ASPECTS OF SUPERHEATED DROPLET DETECTORS AND THEIR APPLICATION IN DARK MATTER SEARCH

By

SUSNATA SETH

(Enrolment No.-PHYS05200704014)

Saha Institute of Nuclear Physics, Kolkata

A thesis submitted to the
Board of Studies in Physical Sciences

In partial fulfillment of requirements
For the Degree of
DOCTOR OF PHILOSOPHY
of
HOMI BHABHA NATIONAL INSTITUTE

August, 2014

Homi Bhabha National Institute
Recommendations of the Viva Voce Board

As members of the Viva Voce Board, we certify that we have read the dissertation prepared by Susnata Seth entitled "Aspects of Superheated Droplet Detectors and their application in Dark Matter Search" and recommend that it may be accepted as fulfilling the dissertation requirement for the Degree of Doctor of Philosophy.

________________________________ Date:
(Chairman/Convener - Prof. Pijushpani Bhattacharjee)

________________________________ Date:
(Member- Prof. Parthasarathi Mitra)

________________________________ Date:
(Member - Prof. Satyajit Saha)

________________________________ Date:
(Member - Prof. Debades Bandyopadhyay)

________________________________ Date:
(Member - Prof. Mala Das)

________________________________ Date:
(External Examiner: Prof. Samit Kumar Mandal)

Final approval and acceptance of this dissertation is contingent upon the candidate's submission of the final copies of the dissertation to HBNI.

I/We hereby certify that I/we have read this dissertation prepared under my direction and recommend that it may be accepted as fulfilling the dissertation requirement.

Place: Guide:

Date: Prof. Pijushpani Bhattacharjee

STATEMENT BY AUTHOR

This dissertation has been submitted in partial fulfillment of requirements for an advanced degree at Homi Bhabha National Institute (HBNI) and is deposited in the Library to be made available to borrowers under rules of the HBNI.

Brief quotations from this dissertation are allowable without special permission, provided that accurate acknowledgement of source is made. Requests for permission for extended quotation from or reproduction of this manuscript in whole or in part may be granted by the Competent Authority of HBNI when in his or her judgment the proposed use of the material is in the interests of scholarship. In all other instances, however, permission must be obtained from the author.

Susnata Seth

DECLARATION

I, hereby declare that the investigation presented in the thesis has been carried out by me. The work is original and has not been submitted earlier as a whole or in part for a degree/deploma at this or any other Institution/University.

Susnata Seth

List of Publications

Journal

1. **Neutron-gamma discrimination by pulse analysis with superheated drop detector.**
   Mala Das, **S. Seth**, S. Saha, S. Bhattacharya and P. Bhattacharjee,
   Nuclear Instruments and Methods in Physics Research A, **2010**, 622, 196-199.

2. **Dark matter search with PICASSO.**
   S. Seth in V. Zacek et al., PICASSO collaboration,
   Journal of Physics : Conference Series, **2012**, 375, 012023.

3. **Constraints on low-mass WIMP interactions on ^{19}F from PICASSO.**
   S. Seth in S. Archambault et al., PICASSO collaboration,
   Physics Letters B, **2012**, 711, 153-161.

4. **The nucleation parameter for heavy-ion induced bubble nucleation in superheated emulsion detector.**
   S. Seth, M. Das, S. Bhattacharya, P. Bhattacharjee and S. Saha,
   Journal of Instrumentation, **2013**, 8, P05001.

5. **Searching for universal behaviour in superheated droplet detector with effective recoil nuclei.**
   Mala Das and **Susnata Seth**,
   Pramana-journal of physics, **2013**, 80, 983-994.

PICASSO Scientific/Technical Report

(Refereed by PICASSO collaboration internal committee.)

1. **Simulation of the α-response of superheated droplet detector for PICASSO experiment.**
   Susnata Seth,
   PICASSO Scientific/Technical Report, (**PSTR_12_001**), **2012**.

2. **Study of alpha particles and neutrons induced nucleations for superheated droplets of smaller size at low frequency.**
   Susnata Seth and Mala Das,
   PICASSO Scientific/Technical Report, (**PSTR_13_003**), **2013**.

3. **Effect of time and gain correction on resolution of PVAR distribution for PICASSO detector.**
   Susnata Seth and Mala Das,
   PICASSO Scientific/Technical Report, (**PSTR_13_004**), **2013**.

Conference Publications

1. **SDD in neutron-gamma field.**
   Mala Das, **Susnata Seth**, and Satyajit Saha,
   18^{th} National Symposium on Radiation Physics, held at Udaipur, November 19-21, 2009.

2. **R-114 and C_4F_{10} as sensitive liquid in superheated drop detector for neutron detection.**
   Mala Das, **Susnata Seth**, and Satyajit Saha,
   DAE symposium on Nuclear Physics, held at Pilani, December 20-24, 2010.

3. **Gamma background rejection in C_4F_{10} superheated droplet detector by pulse analysis.**
   Mala Das, **Susnata Seth**, Satyajit Saha, and Pijushpani Bhattacharjee,
   International Symposium on Accelerator and Radiation Physics (ISARP), held at Kolkata, February 16 - 18, 2011.

4. **Simulation of the response of superheated droplet detector to high energy heavy ion.**
   Susnata Seth, Sudeb Bhattacharya, Mala Das, Pijushpani Bhattacharjee, and Satyajit Saha,
   DAE symposium on Nuclear Physics, held at Visakhapatnam, December 26-30, 2011.

5. **The effective recoil nuclei in superheated droplet detector for WIMPs dark matter search.**
   Mala Das and **Susnata Seth**,
   DAE symposium on Nuclear Physics, held at Visakhapatnam, December 26-30, 2011.

6. **Study of neutron and alpha particle induced events in superheated droplet detector.**
   S. Seth, P. K. Mondal, and M. Das,
   DAE symposium on Nuclear Physics, held at Delhi, December 3-7, 2012.

7. **Simulation of the intrinsic background of PICASSO detector for dark matter search experiment.**
   S. Seth, M. Das, on behalf of PICASSO collaboration,
   DAE symposium on Nuclear Physics, held at Delhi, December 3-7, 2012.

8. **Role of acoustic energy in reduction of background of PICASSO detector.**
   Susnata Seth and Mala Das, on behalf of PICASSO collaboration,
   DAE International symposium on Nuclear Physics, held at Mumbai, December 2-6, 2013.

Others

1. **Study of low frequency acoustic signals from superheated droplet detector.**
   Prasanna Kumar Mondal, **Susnata Seth**, Mala Das and Pijushpani Bhattacharjee,
   Nuclear Instruments and Methods in Physics Research A, **2013**, 729, 182-187.

Signature of Student:

ACKNOWLEDGEMENTS

It is a great pleasure to thank the people who helps me during my research works in Saha Institute of Nuclear Physics. First and foremost, I would like to acknowledge and thank my advisor, Prof. Pijushpani Bhattacharjee for his valued guidance, discussions, suggestions and encouraging me to proceed my doctoral research work on this topic. I really thankful to him for his valuable feedback that improved this thesis.

I would sincerely like to thank Prof. Mala Das for her careful guidance and constant encouragement in pursuing my research work. She helped all through my research work whenever I needed. Without her dedicated supervision, support and encouragement, it is not possible to complete this thesis.

I would like to express my sincere thank to Prof. Sudeb Bhattacharya for his valuable discussions, suggestions and guidance in writing the simulation code. I would sincerely like to thank Prof. Satyajit Saha for his valuable discussions and suggestions.

I would like to thank Mr. Nilanjan Biswas and Dr. Prasanna Kumar Mondal for their various assistance in performing experiments, and Dr. Richard Britto for valuable discussions on analysis.

I am grateful to Prof. B. K. Chatterjee, Department of Physics, Bose Institute, Kolkata for providing the R-114 liquid and ^{137}Cs gamma source, ^{241}AmBe neutron source and Dr. Chandana Bhattacharya, VECC, Kolkata for providing ^{241}Am alpha source.

I would like to thank all the members of PICASSO collaboration, past and present, for their valuable discussions, suggestions and support. My special thanks to Dr. Sujeewa Kumaratunga, Dr. Marie-Cécile Piro and Dr. Christopher Jackson for their guidance and discussions on performing the analysis of PICASSO experiment data. I am especially thankful to Dr. Viktor Zacek for his valuable suggestions.

I would like to thank all of my friends. It would be impossible to mention each person's contributions, and I certainly would make omissions. I express my sincere gratitude for their friendship, encouragement.

Lastly, but also most importantly, I am thankful to my parents, elder sister, brother in law, nephew, other family members and well wishers for their love and support.

I sincerely apologize for unwillingly omission of any name from the above list of acknowledgment.

Contents

SYNOPSIS

A superheated droplet detector (SDD) (sometimes also called bubble detector) consists of a large number of droplets of a superheated liquid suspended in another immiscible liquid-like, soft gel medium or a firm polymer matrix. The droplets are kept in the 'superheated' liquid state at temperatures above the normal boiling temperature of the liquid (corresponding to the ambient pressure) by isobaric heating or isothermal decompression. The basic principle of operation of SDD is similar to that of a bubble chamber : The superheated state being metastable, the passage of an energetic particle through a droplet can trigger a 'nucleation' event, whereby the energy deposited by the particle within the droplet can cause a phase transition of the metastable liquid phase to the vapour phase. If the energy deposited by the particle within a certain critical length is larger than a certain critical energy, the vapour bubble grows, eventually converting the whole liquid droplet into the vapour phase. The acoustic pulse generated in this process constitutes the signal of passage of the particle, which is recorded by acoustic sensors. Random nucleation events can also be caused by the presence of various kinds of heterogeneous nucleation sites such as solid impurities, air bubbles or gas pockets trapped at the solid-liquid interface at the container surface. SDDs are currently being used in various areas such as in neutron dosimetry, gamma ray detection, proton detection, heavy ion detection, neutron spectrometry and also in cold dark matter search experiments.

This thesis presents a detailed study of the response of SDDs to various kinds of particles such as neutrons, alpha particles, gamma rays and heavy ions, with a view to a better understanding of the working principles of SDDs in general and towards developing effective procedures for discrimination of nucleation events due to various particles (neutrons, alphas, gamma rays, etc.) that are known to be responsible for the background events in experiments for direct detection of Weakly Interacting Massive Particle (WIMP) candidates of dark matter (DM) using SDDs.

The thesis is divided into two parts: The main objectives of Part I are (i) to study the response of the SDD to heavy ions and, in particular, to study the dependence of the nucleation parameter (k) on the mass of the heavy ions, and (ii) to study discrimination of neutron and gamma-ray induced nucleation events in SDDs with different active liquids. In Part II, certain issues pertaining to the application of SDDs in the direct detection of the WIMP candidates of DM by the PICASSO experiment[1], are discussed. Specifically, results of investigations into the following aspects of the experiment are presented: (i) To understand the reason behind the two different threshold temperatures observed for α-induced events in the detector, (ii) to study the role of the droplet size (of the active liquid) in the discrimination between α- and neutron induced nucleation events in the detector, and (iii) development of an analysis procedure to improve the resolution of discrimination between the α- and neutron (or nuclear recoil) induced events.

Below we give a brief description of the contents of various chapters of the thesis.

In **Chapter 1** we provide a general overview of the SDD and its application in the search for the WIMP candidates of DM. We then provide a description of the contents of the subsequent chapters of the thesis.

In **Chapter 2**, which constitutes the first chapter of Part I of the thesis, we discuss the basic working principle of SDDs. Though a universally accepted complete theory is not available, Seitz's thermal spike model provides a reasonably good explanation of the basic principle of the particle/radiation-induced nucleation in a superheated liquid. A critical minimum energy (E_{c}) has to be deposited by the

[1]The PICASSO experiment is an international collaboration of nine institutions from four countries (including Saha Institute of Nuclear Physics, Kolkata, India), and is located at the SNOLAB underground facility in Sudbury, Ontario, Canada.

interacting particle within a small localized region in order for a nucleation event to take place. If the initial size of the resulting vapour bubble is above a certain critical radius (r_c), the bubble becomes thermodynamically unstable and grows rapidly to visible size. Both r_c and E_c decrease rapidly with temperature. Thus bubble nucleation probability increases with temperature. This allows the detector to be made sensitive or insensitive to different particles by appropriately choosing the temperature and or pressure. In other words, the SDD is a threshold-type detector. These aspects are discussed in details in Chapter 2 including the definition of the "nucleation parameter", an important quantity that characterizes the nucleation process that is discussed further in later chapters.

In **Chapter 3**, we focus on simulation studies to understand bubble nucleation due to heavy ions. We present our results of the simulation of the response of superheated droplet detector with active liquid R-114 ($C_2Cl_2F_4$; b.p. 3.77 °C) to heavy ions ^{12}C(180 MeV/u), ^{20}Ne(400 MeV/u) and ^{28}Si(350 MeV/u). The values of the nucleation parameter, k, for bubble nucleation induced by high energy heavy ions ^{12}C(180 MeV/u), ^{20}Ne(400 MeV/u) and ^{28}Si(350 MeV/u) are determined by comparing the experimentally obtained normalized count rates with those obtained from our simulation code based on GEANT3.21. We have performed two separate sets of simulation: In Simulation I, the geometry of the detector used in the actual experiment is simulated, and in Simulation II, instead of simulating the whole experimental set up, we independently determined the nucleation probability of a single droplet as a function of nucleation parameter, k. This nucleation probability is then used to calculate the expected nucleation rate for different temperatures. It is observed from our results that the value of k for ^{12}C(180 MeV/u) is higher than that for higher mass ions like ^{20}Ne(400 MeV/u) and ^{28}Si(350 MeV/u), i.e., the value of k decreases with the increase in mass of heavy ions. Thus the present simulation provides an important observation that the nucleation parameter depends on the mass number of the ion.

In **Chapter 4** we discuss the results of our experiment performed to understand the discrimination between the neutron- and gamma-ray induced nucleation events. This is crucial for measurement of neutron dose in a strong background of gamma-ray as well as for dark matter search experiments. The experiments are performed using two different liquids, namely, R-114 and C_4F_{10} (b.p. -1.7 °C at a pressure of 1.013 bar). For this purpose, we use a ^{252}Cf (3.2 μCi) fission neutron source and a ^{137}Cs gamma-ray source (32.5 mCi). We have performed the experiments at the neutron sensitive temperatures of 55 °C for R-114 and 35 °C for C_4F_{10} and also at neutron and gamma-ray sensitive temperatures of 70 °C for R-114 and 55 °C for C_4F_{10} in presence of ^{252}Cf source. Trace of each pulse is recorded and the power (P) is calculated from the amplitudes of the pulses. The power, P, which is a measure of the energy released during the bubble nucleation process, is defined as $\log_{10}(\sum_i |A_i|^2)$, where A_i is the pulse amplitude in volt of the digitized acoustic pulse at the i^{th} time bin, and the summation extends over the duration of the signal. The experimental results show that the neutron induced events have higher values of P than those due to the gamma-ray induced events. This is because of the fact that the linear energy transfer (LET) due to heavy recoiling nuclei produced by the incident neutrons is in general larger than that due to gamma rays for which the energy deposition occurs essentially due to secondary electrons which deposit energy in the medium almost at the end of their tracks. The results of our experiment performed with liquid R-114 at temperatures 70 °C and 75 °C with the gamma-ray source ^{137}Cs also show that the pulses are of relatively lower amplitudes compared to those due to neutrons from ^{252}Cf. This important observation clearly demonstrates for the first time the possibility of identification of and hence discrimination between neutron and gamma ray induced nucleation events by measuring the pulse height distribution in a mixed neutron-gamma radiation field. In addition, it is also observed from our experiment that the position of the peak of the P-distribution is independent of temperature for ^{137}Cs gamma-ray induced events in C_4F_{10}. This is useful for applying temperature independent rejection of the gamma-ray induced events. Finally, it is found that R-114 as the active liquid provides a better discrimination between neutron- and gamma ray induced events than C_4F_{10}.

In **Chapter 5**, we focus on direct detection of the WIMP candidates of DM. From theoretical point of view, currently the most favored candidate of DM are the so-called Weakly Interacting Massive Particles (WIMPs) predicted in many models of particle physics beyond the Standard Model. After providing a concise review of the phenomenology of direct detection, we discuss in detail the PICASSO (Project In CAnada to Search for Supersymmetric Objects) experiment, which searches for the WIMPs using SDDs with perfluorobutane, C_4F_{10}, as the target material. The PICASSO experiment is primarily sensitive to the spin-dependent (SD) interaction of the WIMPs because of the relatively large SD cross section of the WIMPs with ^{19}F contained in C_4F_{10}, although PICASSO is also sensitive to the spin-independent (SI) WIMP interactions due to the presence of the carbon atoms in C_4F_{10}. In addition, due to the relatively light mass of the target nucleus ^{19}F and the low recoil detection threshold energy of about 1.7 keV, the PICASSO experiment is currently one of the most sensitive experiments for relatively low mass WIMPs (below 15 GeV/c^2). Details of the data analysis procedure for the PICASSO experiment and a brief review of the latest results from the experiment are given.

Chapter 6 of the thesis is devoted to a simulation study to understand the alpha background. We have simulated the response of the two α-spiked detectors, which are particularly prepared and used in the PICASSO experiment to understand the response of the superheated liquids for known source of α contamination. It is observed from experiments that the response of detector for these two cases has two different threshold temperatures. The simulation is performed using our simulation code based on GEANT 3.21 for two cases with alpha particles (a) from ^{241}Am embedded in the polymer matrix and (b) from ^{226}Ra embedded both in the polymer matrix and in the liquid droplets. A small prototype detector having randomly distributed droplets of active liquid C_4F_{10} in a holding matrix of CsCl, which is the main constituent component of the polymer matrix used in the PICASSO experiment, is simulated. From the results of the simulation, it is observed that the threshold temperature of alpha particles in the case of ^{241}Am spiked detector (for which the source of the α contamination is in the polymer matrix only) and the case of ^{226}Ra spiked detector (for which the α contamination is present both in the droplet as well as in the polymer matrix) is same, while the calculation of LET using SRIM2008 code explains that the higher LET of recoiling nuclei, Pb, of energy 146 keV coming from ^{226}Ra decay chain is responsible for the experimentally observed lower threshold temperature in case of ^{226}Ra spiked detector. These results of our simulation yield a proper understanding of the actual experimental results.

In **Chapter 7** we discuss the effect of the droplet size on the discrimination between α- and neutron induced events, considering the low frequency components of the signal. A condenser microphone is used as acoustic sensor to acquire the low frequency components of the signal. For this purpose, we have performed experiments with superheated R-12 (CCl_2F_2, b. p. -29.8 °C) droplets dispersed in soft aquasonic gel matrix in presence of two neutron sources, namely, ^{241}Am-Be (3 Ci) and ^{252}Cf (3.2 μCi), and an α-source, ^{241}Am (30 particles s^{-1}) at the temperature of 33.5±0.5 °C. The droplets of two different radius distributions (0-100 μm) are used. The analysis is carried out using the filtered signals and their frequency spectrum using a code based on the ROOT data analysis software. We considered the effectiveness of several different variables for discrimination between the neutron and α- induced events. It is observed that the Power (P) and '$\ln(A^2)$' (where A is the maximum amplitude of the signal), are two reasonably good variables for discrimination between α- and neutron induced events. The logarithm of the area under the power spectrum of the signal ($\log_{10} P_A$) is another good variable for the discrimination. Instead of obtaining larger amplitude of pulses for alpha-particle induced events, as previously observed by COUPP, PICASSO and SIMPLE experiments, both smaller and larger amplitude pulses are observed in our present experiments due to the different smaller droplet size distribution used in our experiment. The present study shows that the α-neutron discrimination works better for smaller droplets and the variable, 'P', gives a better discrimination capability than '$\ln(A^2)$' which was used by the SIMPLE experiment.

In **Chapter 8**, we describe a new analysis method for obtaining a better α-neutron discrimination capability through the variable PVAR (which is a measure of the acoustic energy released during the bubble nucleation process). It is observed that the value of this variable decreases with time which makes the PVAR distribution broader, thereby affecting the α-neutron discrimination ability. We have developed two correction methods to improve the resolution of PVAR distribution by controlling the effect of decrement of PVAR with time. This has resulted in significant improvement in the data analysis of the PICASSO experiment.

Finally, in **Chapter 9**, we conclude by summarizing the main results of this thesis.

List of Figures

List of Tables

Chapter 1

General Introduction

1.1 Superheated Droplet Detector

A liquid is called superheated liquid, when it maintains its liquid state at a temperature above its boiling point (corresponding to the ambient pressure). It is possible to reach that state by "isobaric heating" (i.e., at a constant pressure, increasing temperature very slowly to/above boiling point starting from a comparatively lower temperature) or, by "isothermal decompression" (i.e., at a constant temperature, reducing pressure very slowly to the ambient pressure starting from a comparatively higher value). The superheated liquid state is a metastable state of liquid. To maintain this metastable state normal boiling should be prevented by removing heterogeneous nucleation sites which act as sites for nucleation of bubbles of the vapour phase of the liquid. Heterogenous nucleation can occur at various interfaces like liquid-solid, liquid-liquid or liquid-gas interfaces. For example, heterogeneous nucleation can be triggered by the presence of trapped air bubbles, gas pockets at the solid-liquid interface of the container and particulate impurities. In addition, random fluctuation of temperature can also cause heterogeneous nucleation. During normal boiling, heterogeneous nucleation occurs at a temperature, namely, the boiling point, (T_b), which is usually much below the homogeneous nucleation temperature, called critical temperature (T_c). The latter represents theoretical upper limit to the temperature of the superheated liquid state in absence of heterogeneous nucleation sites. Unlike heterogeneous nucleation, homogeneous nucleation occurs in the bulk of the liquid. Though theoretically the superheated liquid state can exist up to the critical temperature (T_c), in actual experiments the maximum temperature up to which the superheated state persists is found to be about 90 % of the critical temperature (T_c) [1, 2, 3]. This limit of temperature is known as 'limit of superheat of the liquid' (T_sl) and depends on the properties of the liquid.

The particle/radiation-induced heterogeneous nucleation makes the superheated liquid a good medium for detection of various types of radiation. The use of superheated liquid as a radiation detector can be said to have been started with the invention of Bubble Chamber (BC) by Glaser [4]. There are two other forms of such radiation detectors in which a large number of droplets of a superheated liquid are suspended in another immiscible liquid-like, soft gel medium or a firm polymer matrix, and are known as 'Superheated Droplet Detector' (SDD) developed by R. E. Apfel [5] and 'Bubble Detector' (BD) developed by H. Ing and H.C. Birnboim [6]. Sometimes together those detectors are known as 'Superheated Emulsion Detector' (SED). In the Superheated Emulsion Detector (SED), after each interaction with an energetic particle, only a small number of droplets evaporate leaving other droplets unaffected. Thus, unlike in BC, there is no need to re-pressurize the liquid after each interaction to make the detector ready for the next particle. In other words, a SED remains continuously sensitive due to presence of a large number of droplets, each of which acts as a small Bubble Chamber. For Bubble Detectors, in which the liquid droplets are held in position by a firm polymer matrix, the evaporated liquid can be reused by re-pressurizing the system.

The phase transition of metastable superheated liquid state to vapour state happens if the total amount of deposited energy by the traversing particle in the superheated liquid within a certain critical path length exceeds a certain critical energy, which depends on the temperature and pressure of the superheated liquid. An important parameter in this context is the 'degree of superheat' defined as the difference between ambient temperature of the superheated liquid and the boiling point of the same liquid at a given pressure. Alternatively at a given temperature it is the difference between the vapour pressure of the liquid in the superheated state and the ambient pressure at that temperature. The 'degree of superheat' increases with increase in the temperature and decrease in the pressure of the superheated liquid. Higher the 'degree of superheat', less is the energy required for bubble nucleation. So, the minimum energy required for bubble nucleation is controlled by varying the temperature and/or the pressure of the superheated liquid, and the detector can be made sensitive or insensitive to different types of particles by appropriately choosing the operating temperature and/or pressure. In other words, the detector acts as a threshold type detector. This property of the superheated emulsion makes this type of detector very usable in measuring dose and obtaining the energy of neutron in mixed neutron-gamma field. In addition to its use in neutron dosimetry [7, 8, 9, 10] and neutron spectrometry [11, 12, 13, 14, 15], another important application of the superheated emulsion detector is in cold dark matter search experiments [16, 17, 18]. Besides, this type of detector is also being used in gamma ray detection [10, 19, 20], proton detection [21], and heavy ion detection [22, 23, 24, 25]. In this thesis, detailed studies of the response of SDDs to various kinds of particles such as neutrons, alpha particles, gamma rays and heavy ions are discussed towards the goal of obtaining a better understanding of the working principles of SDDs.

1.2 Application of Superheated Droplet Detector in dark matter search

A variety of astronomical observations indicate that more than 80 % of the gravitating mass in the Universe resides in a form that emits no detectable electromagnetic radiation of any kind and is, therefore, termed "Dark Matter" (DM). The nature and composition of this DM are currently unknown and constitute one of the major unsolved problems in fundamental physics. In terms of the mass-energy budget of the Universe, the DM constitutes about a quarter while the Visible Matter (VM) in the form of stars, galaxies, gas etc. form less than 5 % of the total energy budget. The rest about 70 % is in a mysterious form of energy called "Dark Energy" (DE) that is thought to be responsible for the observed accelerated expansion of the Universe. For a review, see, for example, [26].

Currently, one of the most favoured candidates of the DM are the so-called Weakly Interacting Massive Particles (WIMPs), with masses anywhere in the range of few GeV to few hundred TeV, predicted in many theories of physics beyond the Standard Model such as those involving supersymmetry [27] and/or extra (spatial) dimensions [28]. Because of their weak interaction with other particles, the WIMPs can decouple relatively early in the Universe and survive in the Universe today with sufficient abundance required to explain the DM. For a review, see [29, 30].

If DM is indeed made up of WIMPs then their elastic scattering with nuclei may be detectable [31]. Currently, a large number of experiments worldwide are searching for WIMPs by looking for possible signature of WIMP induced nuclear recoils in various detector materials. WIMPs can give rise to nuclear recoils with kinetic energy of the order of few tens to hundreds keV. Typical interaction rate of WIMPs is less than 1 event per kilogram of detector mass per day. In the detector medium signals are generated through three processes: ionization, scintillation and phonon/heat generation. There are various kinds of detectors, some of which need cryogenic system to maintain the temperature at very low value to observe the signature of WIMP induced recoils.

In this thesis, we discuss the use of SDDs in direct detection experiment of WIMP. SDDs are non-cryogenic detectors. Similar to two DM search experiments, SIMPLE (Superheated Instrument for Massive ParticLe Experiments) [17] and COUPP (The Chicagoland Observatory for Underground Particle Physics) [18], the PICASSO (Project In CAnada to Search for Supersymmetric Objects) experiment uses superheated liquid as the target. In this thesis I have focused on the PICASSO experiment. Each detector module of PICASSO experiment consists of droplets (of typically radius $\sim 100\mu$m) of superheated freon liquid C_4F_{10} (b.p. -1.7 °C at a pressure of 1.013 bar), and records the acoustic signals, in audible and ultrasonic region, associated with the passage of particles through the liquid droplets. The target material of the detector contains nuclei of fluorine and carbon. Fluorine has a relatively large spin-dependent (SD) interaction cross-section with WIMPs. Thus PICASSO experiment is primarily sensitive to spin-dependent (SD) interaction of WIMPs with detector nucleus. PICASSO experiment is also sensitive to spin-independent (SI) WIMP interaction due to presence of carbon nuclei. In addition, due to the relatively light mass of the target nucleus ^{19}F and the low recoil detection threshold energy of about 1.7 keV, the PICASSO experiment is currently one of the most sensitive experiments for relatively low mass WIMPs (below 15 GeV/c^2). The advantage of the use of SDD is that this type of detector can operate at room temperature, and no cryogenic system is required. The PICASSO experiment is located at the underground laboratory facilities of the Sudbury Neutrino Observatory (SNOLAB) in Sudbury, Canada.

It is very important in a rare particle search experiment, such as a WIMP search experiment, to estimate the backgrounds and to employ the methods for minimisation of the background. It is also required to discriminate between various types of the background events and also between the WIMP induced events and background events. Of special concerns are the background arising due to neutrons because both neutrons and WIMPs can give rise to nuclear-recoil induced nucleation events. To reduce the cosmic ray induced backgrounds, generally the WIMP search experiments are performed at underground sites. Also to reduce the background due to neutrons, the PICASSO detectors at SNOLAB are surrounded by a 30.5 cm thick water shield, which acts as a neutron moderator and absorber [32].

The γ-ray and β-induced backgrounds typically yield low values of linear energy transfer (LET). As a result PICASSO detectors become sensitive to these backgrounds only at relatively higher temperatures. As SDD is threshold type detector, the background events due to γ and β radiations can be rejected by selecting appropriate low operating temperature range. Though PICASSO experiment is capable of rejecting the γ-ray and β-induced backgrounds, the events due to intrinsic background, such as those due to α-particles, are comparatively more difficult to discriminate and eliminate. Different simulations, experiments and analysis of PICASSO experiment data are going on to understand and discriminate the alpha background from recoil induced events. One of the main aims of this thesis is to study the alpha background of PICASSO experiment.

1.3 Layout of the thesis

This thesis is written in two parts: **Part I** contains the details of superheated droplet detector and the results of different types of studies, including simulation and experiments, which are carried out to understand the physics behind bubble nucleation in SDD. In **Part II**, the application of SDDs in dark matter search experiments is discussed with special emphasis on simulation and experimental studies and analysis of data from PICASSO experiment in order to understand and reduce the effect of α-background, in the experiment.

Chapter 2 is the first chapter of **Part I**. In this chapter, I have described the basic principle of operation of Superheated Droplet Detector (SDD). I briefly describe the different definitions of the "nucleation parameter" that characterize the process of bubble nucleation in SDDs.

In **Chapter 3**, the response of SDD to high energy heavy ions is simulated to better understand the bubble nucleation process. In particular we study the mass dependence of the nucleation parameter for high energy heavy ion induced nucleation process.

In **Chapter 4**, I describe experimental studies that have been performed to discriminate between neutron and gamma induced events. It contains a comparative study of discrimination between neutron and gamma ray induced bubble nucleations for SDDs made of two different active liquids, namely, R-114 ($C_2Cl_2F_4$; b.p. 3.7 °C) and C_4F_{10}.

In **Chapter 5**, the first chapter of **Part II**, I first briefly review the phenomenology of direct detection of WIMP DM particles. I then provide a brief discussion of different methods of direct detection of WIMPs. The methodology of attempts towards direct detection of WIMPs by PICASSO experiment is explained in details. Details of the data analysis procedure for the PICASSO experiment and a brief review of the latest results from the experiment are also given.

In **Chapter 6**, I present our studies on the α-background in PICASSO experiment. This Chapter contains simulation studies towards the goal of understanding the characteristics of the α-induced events. I have described the results of the simulation of α-background of the PICASSO experiment. The simulation has been performed to understand the reason behind the two different threshold temperatures obtained for two different alpha sources, namely, ^{226}Ra and ^{241}Am.

In **Chapter 7**, I present experimental studies on discriminating the α-induced events from neutron/WIMP recoil induced events. Experimental studies to understand the role of smaller droplets and low frequency components of the acoustic signal for discrimination between alpha and neutron induced nucleation events are presented.

In **Chapter 8**, a new analysis method has been described for obtaining a better alpha-neutron discrimination capability using PICASSO experiment data.

Finally, in **Chapter 9**, we conclude by summarizing the main results of this thesis.

Part I

Some aspects of Superheated Droplet Detectors

Chapter 2

Basic principle of Superheated Droplet Detector

2.1 Introduction

The superheated liquid state is a metastable state. It transits to the more stable vapour state through formation of a nucleus of vapour bubbles which subsequently expand to convert the liquid state to vapour state. A universally accepted complete theory of the mechanism of bubble nucleation is still unavailable. However, Seitz's phenomenological "thermal spike"model [33] provides a good description of the basic principles of the particle/radiation-induced bubble nucleation in a superheated liquid. According to this model, during the passage of an energetic particle through a liquid droplet, a "thermal spike" [33] caused by the energy deposited in a highly localized region within the liquid droplet is responsible for bubble nucleation. As a result, vapour embryos of different sizes are produced along the track of that particle. If the radius of the vapour embryo is larger than or equal to a certain critical radius (r_c), the vapour bubble becomes thermodynamically unstable and grows rapidly to visible size through evaporation of rest of the superheated liquid of the droplet. Otherwise it collapses back to the liquid state due to surface tension. Acoustic pulse generated during this process provides the signal of the passage of the particle, which can be recorded by acoustic sensors.

To form a bubble of critical radius ($r_{\rm c}$), the energy deposition ($E_{\rm dep}$) by charged particle along an effective path length ($L_{\rm eff}$) within the superheated liquid must be greater than or equal to the critical minimum energy, $E_{\rm c}(T, p)$ (see Equation (2.8) below), which is required to from that bubble, i.e., the condition of bubble nucleation can be expressed by the following equations,

$$E_{\rm dep} \geq E_{\rm c}, \tag{2.1}$$

or,

$$\int_0^{L_{\rm eff}} \frac{dE}{dx} dx \geq E_{\rm c}, \tag{2.2}$$

where $\frac{dE}{dx}$ is the linear energy transfer (LET) of the charged particle. The effective path length ($L_{\rm eff}$) is related to the critical radius ($r_{\rm c}$) as discussed in the next Section. This condition is also true for the critical minimum energy expressed by the Equation (2.5) below.

2.2 Condition of bubble nucleation and definition of nucleation parameter

The free energy (G) required to form a spherical vapour bubble of radius r in a liquid was first derived by Gibbs using classical thermodynamics [34]. Gibbs defined the free energy as the difference between the surface energy and volume energy required to create a vapour bubble of radius r.

$$G = 4\pi r^2\sigma(T) - \frac{4\pi}{3}r^3(p_\mathrm{v} - p_0), \tag{2.3}$$

where, σ(T) is the surface tension (liquid-vapour interfacial tension) of liquid at the

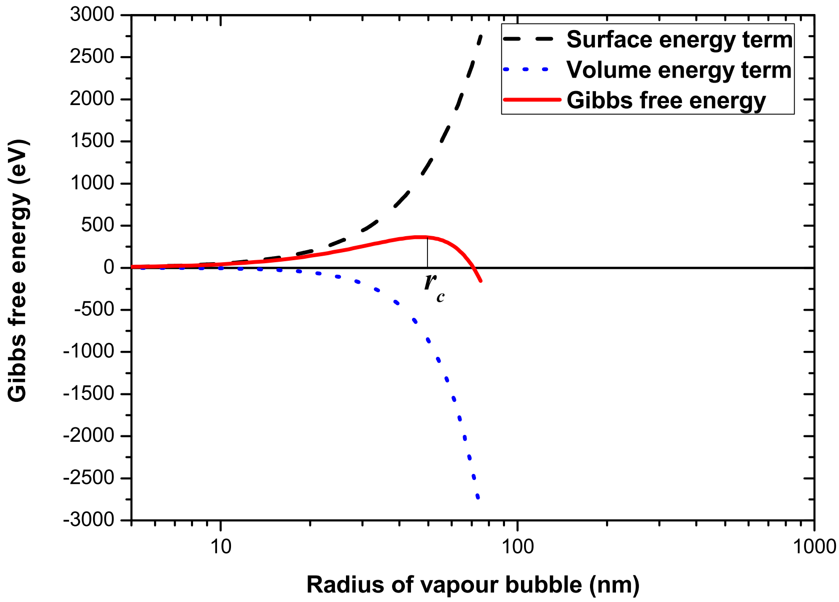

Figure 2.1: Plot of Gibbs free energy to form vapour bubble of radius r as obtained from Equation (2.3). The variation of surface energy and volume energy terms are also shown in the plot as a function of the radius of vapour bubble.

temperature T, p_v is the equilibrium vapour pressure of superheated liquid and p_0 is the ambient pressure (pressure of the surroundings of the bubble). The quantity (p_v-p_0) is often called the "degree of superheat" of the liquid. In Figure 2.1, Gibbs free energy is plotted as a function of radius of C_4F_{10} liquid at temperature 35 °C. It shows that the value of G first increases with increasing radius of bubble, reaches a maximum, and then decreases with increasing r. The radius for which G is maximum (i.e. the bubble becomes unstable to growth) is known as critical radius (r_c), which is expressed by following equation obtained by using the condition

$\frac{dG}{dr}$=0, so

$$r_{\mathrm{c}} = \frac{2\sigma(T)}{p_{\mathrm{v}} - p_0} = \frac{2\sigma(T)}{\Delta p}. \tag{2.4}$$

The minimum amount of reversible thermodynamic work (W) to from a vapour bubble of critical size was originally derived by Gibbs and can be obtained by substituting the expression r_{c} in Equation (2.3). So, the expression of W is,

$$W(T,p) = \frac{16\pi\sigma^3(T)}{3(p_{\mathrm{v}} - p_0)^2}. \tag{2.5}$$

Since the degree of superheat ($p_{\mathrm{v}} - p_0$) increases and surface tension (σ) decreases with increasing temperature, the critical minimum energy or threshold energy (W) required for nucleation decreases with increasing temperature. An important quantity in this context is the energy deposited by the particle within an effective path length $L_{\mathrm{eff}} = 2r_{\mathrm{c}}$ [35], i.e.

$$E_{\mathrm{dep}} = L_{\mathrm{eff}}\left(\frac{dE}{dx}\right) = 2r_{\mathrm{c}}\left(\frac{dE}{dx}\right). \tag{2.6}$$

Usually, only a small fraction of the total deposited energy (E_{dep}) is utilized in the nucleation process. The quantity $\frac{W}{E_{\mathrm{dep}}}$ is called the "thermodynamic efficiency" (η_{T}) for the bubble nucleation process [35]. The value is typically in the range of 3% to 5% for neutron induced nucleation [35]. The condition for bubble formation is also written as,

$$\frac{W}{kr_{\mathrm{c}}}(T,p) \geqslant \frac{dE}{dx}\ , \tag{2.7}$$

where k is the "nucleation parameter" [36] and is equal to twice the thermodynamic efficiency (η_{T}) [13]. Note that the right hand side of the Equation (2.7) depends on the energy of the incident particle while the left hand side is a function of the temperature and pressure of the liquid. The characteristics of the nucleation parameter (k) have been studied in detail in the Refs. [13, 25, 36, 37]. From experiment, the estimated value of k for bubble nucleation induced by neutrons from Am-Be source in superheated liquid R-114 was found to be 0.1158 [37]. However the value of k somewhat different for bubble nucleation induced by other particles, in particular, heavy ions or neutrons of different energies. In Chapter 3, we shall discuss in detail the dependence of the nucleation parameter k on the mass of the heavy ions inducing bubble nucleation in superheated liquid R-114. In Chapter 6, the nucleation parameter for alpha particle induced bubble nucleation in superheated liquid C_4F_{10} will be discussed.

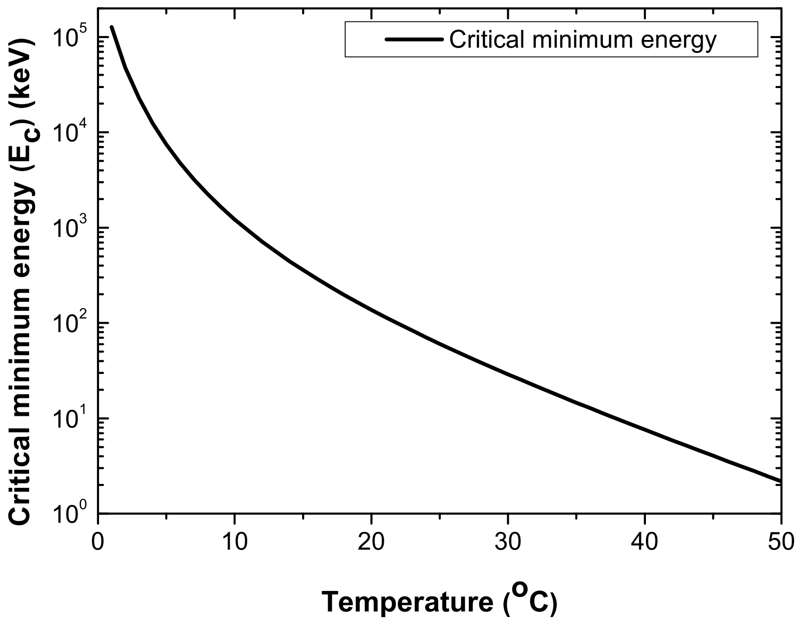

Figure 2.2: Plot of critical minimum energy required to from C_4F_{10} vapour bubble of radius r_c (obtained from Equation (2.8)) as a function of temperature.

Instead of considering only the contribution of reversible thermodynamic work, the critical minimum energy can be calculated as the sum of the reversible works of bubble surface formation, evaporation of the liquid and expansion against pressure of the liquid and the irreversible works, such as energy lost by generation of the acoustic wave emission, by the action of viscous forces during bubble's growth, the thermal energy lost during the bubble expansion to its critical radius. The expression of E_{c} is [38, 39],

$$E_{\mathrm{c}} = -\frac{4\pi}{3} r_{\mathrm{c}}^3 (p_{\mathrm{v}} - p_0) + \frac{4\pi}{3} r_{\mathrm{c}}^3 \rho_{\mathrm{v}} h_{\mathrm{lv}} + 4\pi r_{\mathrm{c}}^2 \left[\sigma - T \frac{d\sigma}{dT} \right] + W_{\mathrm{irr}}, \tag{2.8}$$

where ρ_{v} is the density of the vapour and h_{lv} is the latent heat of evaporation. The first term in Equation (2.8) explains the reversible mechanical energy during expansion to a bubble of radius r_{c} against the pressure of the liquid. The second term represents the energy needed to evaporate the liquid during formation of the bubble of critical radius. The third term describes the work needed initially to create the liquid-vapour interface of vapour embryo while the last term, W_{irr}, is the irreversible works which has smaller contribution than other terms. The calculation of the each terms of the Equation (2.8) for various freons at different temperatures, indicated that the first three terms provide more than 99 % of the critical minimum energy [40]. In Figures 2.2 and 2.3, E_{c} and r_{c} are plotted as a function of temperature and it is observed that both decrease rapidly with increasing temperature.

It is to be noted that in addition to the nucleation parameter, k, there is another nucleation parameter, namely, a, which relates the effective path length with critical radius by the expression $L_{\mathrm{eff}} = a r_{\mathrm{c}}$. In this case, instead of using the expression of W, the expression of E_{c} shown in Equation (2.8) is used as the required critical minimum energy to form the vapour bubble of radius r_{c}. The value of the nucleation parameter a is suggested as 2π or 6.28 times the critical radius by Norman and Spiegler [41] which is based on the Lord Rayleigh's criteria of instability of vapour jets in a liquid [42]. The threshold temperature

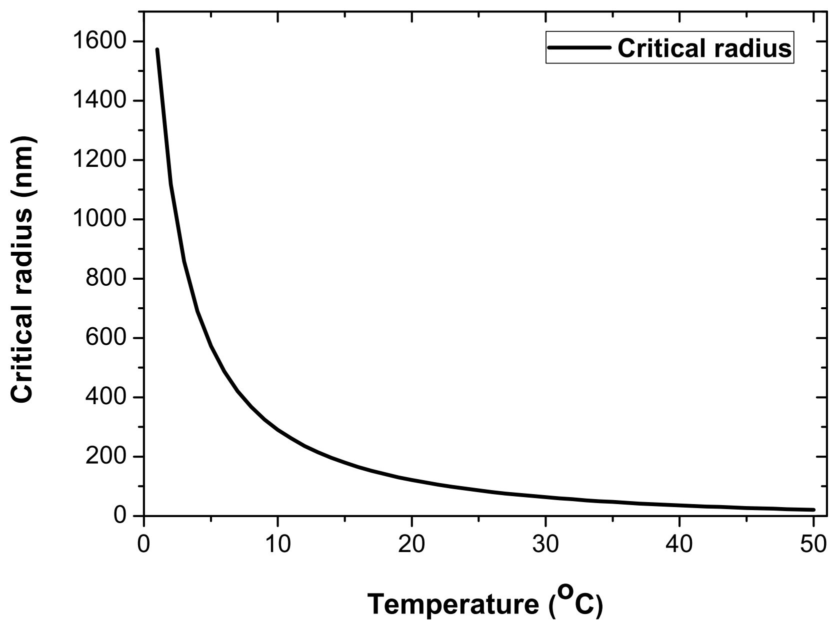

Figure 2.3: Plot of critical radius of vapour bubble of C_4F_{10} (obtained using Equation (2.4)) as a function of temperature.

of nucleation for neutrons of energy few MeV to 14.1 MeV has been observed for different superheated liquids like water, acetone, benzene and comparison of the experimental results with theoretical prediction gave the value of a in the range 6.28 - 12.96 [43, 44]. Using the Seitz's "temperature spike" theory [33] and Rayleigh's criteria, Bell et al. [45] developed an analytic method, according to which the value of a is always 6.07 independent of the type of radiation and fluid and the system condition. This value of the nucleation parameter a was not consistent with the results from various experiments performed with various liquids like water, propylene glycol, acetone, benzene [43, 44, 46, 47].

In another description of the nucleation process [48], the effective length is expressed as $L_{\mathrm{eff}} = br_{\mathrm{cl}}$, where b is the nucleation parameter and r_{cl} is the radius of the seed liquid droplet. A seed liquid droplet contains the same mass of superheated liquid as that of the critical sized vapour bubble of radius r_{c}. The critical minimum energy required for nucleation has also been expressed by Equation (2.8) in this model. The radii r_c and r_cl are related by the following equation,

$$r_\mathrm{cl} = (\frac{\rho_\mathrm{v}}{\rho_\mathrm{l}})^{1/3} r_\mathrm{c} \ , \tag{2.9}$$

where ρ_v and ρ_l are the densities of the vapour and the liquid used as the sensitive liquid. The relation between these three nucleation parameters, k, a and b is derived as [36, 49],

$$b = k \frac{E_\mathrm{c}}{W} \frac{r_\mathrm{c}}{r_\mathrm{cl}}, \tag{2.10}$$

and,

$$b = a \frac{r_\mathrm{c}}{r_\mathrm{cl}}. \tag{2.11}$$

In the next Chapter we study the behaviour of nucleation parameter, k, for bubble nucleation induced by heavy ions.

Chapter 3

The nucleation parameter for heavy ion induced bubble nucleation in Superheated Droplet Detector

3.1 Introduction

In this Chapter we study an important parameter, namely, nucleation parameter, that characterizes the bubble nucleation process in superheated droplet detectors. As discussed in the previous Chapter, there is no universally accepted theory of 'bubble nucleation'. There are various phenomenological models to describe the nucleation process in superheated droplet detector. In the present Chapter, we use the nucleation parameter k as defined in Ref. [36] and discussed in more details in Section 2.2. There have been a large number of studies which attempt to estimate the value of nucleation parameters for neutrons [10, 36, 43, 44, 45, 48, 49]. But not much work has been done on estimation of nucleation parameter for heavy ions. In an earlier work [25], the response of SDD to various high energy heavy ions has been studied and the nucleation parameter has been estimated from the experimental results using estimation of $\frac{dE}{dx}$ from SRIM 2008 code [50]. In the present work, we consider the detailed geometry of the detector, allowing us to make a more accurate estimate of $\frac{dE}{dx}$, resulting in a more reliable estimate of the nucleation parameter for heavy ions.

Experimental studies on detection of heavy ions by superheated droplet detectors have been done in Refs. [22, 23, 24, 25]. From measurement of the maximum track length for various ions in a superheated droplet detector, the relationship between maximum track length and the atomic number of the ions can be established, allowing identification of heavy ions [22, 23, 24]. The high energy heavy ions used in these studies were ^{12}C (290 MeV/u), ^{28}Si (600 MeV/u), ^{40}Ar (650 MeV/u), ^{56}Fe (500 MeV/u), ^{84}K (400 MeV/u) and ^{132}Xe (290 MeV/u). The response, threshold temperatures and the threshold degree of metastability of nucleation in superheated droplet detector made of active liquid R-114 were investigated for different heavy ions with different energies, namely, ^{12}C (180 MeV/u, 230 MeV/u), ^{20}Ne (230 MeV/u, 400 MeV/u), ^{28}Si (180 MeV/u, 350 MeV/u), ^{40}Ar (500 MeV/u), and ^{56}Fe (500 MeV/u) [25, 51]. The track length for protons has also been studied and in this case bubble tracks are formed by protons in the region corresponding to the Bragg peak of protons in the detector [21].

To understand the response of superheated droplet detectors to various particles, one has to take recourse to simulation. Computational studies of the response of superheated droplet detector to neutrons have been done using the frame work of Seitz's radiation-induced nucleation theory [33, 52]. Monte Carlo studies of the response of superheated droplets of liquid C_4F_{10} for alpha particles, neutrons, gamma rays and δ-rays have been done within the context of dark matter search experiments [16]. These studies have allowed determination of various parameters like the alpha detection efficiency as a function of temperature and the loading factor of the detector. It was also established from simulation studies that the maximal alpha detection efficiency is inversely proportional to the droplet radius.

In the present work, we present our results of the simulation of the response of superheated droplet detector with active liquid R-114 ($C_2Cl_2F_4$) to heavy ions ^{12}C (180 MeV/u), ^{20}Ne (400 MeV/u) and ^{28}Si (350 MeV/u) using GEANT3.21 simulation toolkit [53]. We also study the possible dependence of the nucleation parameter k [36] on the mass of the heavy ions. We have performed two separate sets of simulations, referred to as Simulation I and Simulation II. In Simulation I, we simulated the geometry of the experimental set up of the actual experiment to calculate the expected nucleation rate. In Simulation II, instead of simulating the whole experimental set up, we independently determined the bubble nucleation probability of a single droplet as a function of the nucleation parameter, k, using GEANT3.21. This nucleation probability is used to calculate the expected number of nucleation events for the same experiment. The normalized count rates at the threshold temperature of bubble nucleation, for the high energy heavy ions ^{12}C (180 MeV/u), ^{20}Ne (400 MeV/u) and ^{28}Si (350 MeV/u) from the above two simulations are compared with the experimental data [25] to estimate the nucleation parameter k, for the heavy ions.

3.2 Present work

The details of the experiment for which the simulation is carried out is described in Ref. [25]. A brief description of the experiment is given below for the sake of completeness. The experimental set up is shown schematically in Figure 3.1. The dimensions of the detector used in the experiment were about 80 mm in length and 15 mm in diameter, containing 5000 droplets of the liquid R-114 suspended in a firm polymer matrix and were inside a glass vial of 1 mm thickness. The vial was placed inside an aluminium holder of thickness 1 mm. The beam entry port was 6 m away from the detector system. The droplets had a distribution in diameter with a sharp peak at about 21 μm. The main component of the polymer was glycerine. Before entering into the detector, the ions passed through 6 m of air, 1 mm of Al holder and 1 mm of glass vial. In the experiment, the particle flux (I_B) was 1000 particles/sec/cm^2. The simulation is carried out for ^{12}C (180 MeV/u), ^{20}Ne (400 MeV/u) and ^{28}Si (350 MeV/u). Below we describe two separate simulations carried out in this work in order to estimate the nucleation parameter (k) by using the results of the experiment described above.

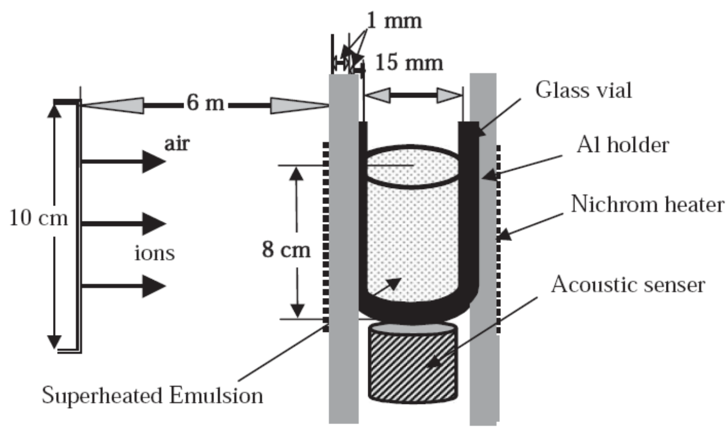

Figure 3.1: Schematic diagram of the set up of the experiment for which the simulation is carried out [25].

3.2.1 Simulation I

In this simulation, we simulate the experimental set up of the actual experiment. The positions of the droplets and incident points of the ions are chosen randomly. There are two parts in the simulation: the geometry and the tracking of particles. In the geometry part, first the glycerine cylinder of density 1.24 gm/cc, glass cylinder of density 2.58 gm/cc and the liquid droplets of R-114 are considered.

The densities of R-114 liquid at different temperatures, are obtained from the

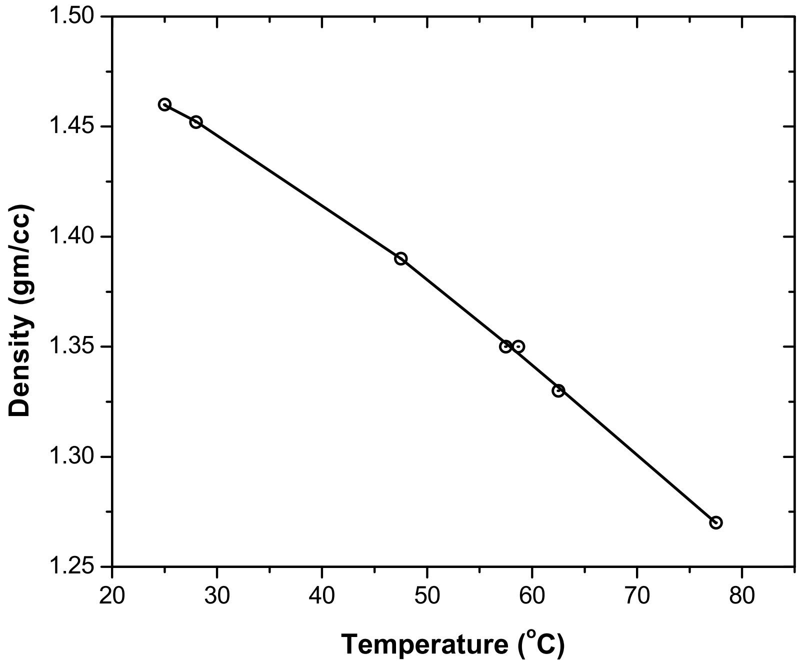

Figure 3.2: Variation of density vs temperature for R-114 liquid.

following fitted functional form, represented by the black line in Figure 3.2, of the density as a function of temperature:

$$y = 1.49059 + 8 \times 10^{-5}x - 6 \times 10^{-5}x^2 + 2.8291 \times 10^{-7}x^3 \ . \tag{3.1}$$

Here y is density in gm/cc and x is temperature in °C. The densities at some specific temperatures as represented by black circles in Figure 3.2 are obtained from Ref. [25]. A cylinder of Al with height 80 mm and diameter 19 mm is created. Within this Al cylinder, a 1 mm thick hollow glass cylinder of same height and outer diameter of 17 mm is placed. Then the cylinder of glycerine with height 80 mm and diameter 15 mm is created and placed inside the hollow glass cylinder. A total of 5000 (N_0) uniformly and randomly distributed non-overlapping droplets of R-114 are then placed in the cylinder containing the glycerine. The distribution of the droplets is shown in Figure 3.3. The diameter of each droplet is taken as 20 μm.

The second part of the simulation is tracking of particles through the geometry described above. The energy deposition by the ions during the passage through 6 m of air is obtained using SRIM 2008 code [50]. As the simulation is done for an experiment of 100 sec time duration, a total of $\sim$ 2.6 million particles coming from negative x-direction is allowed to fall randomly on the outer surface of the Al cylinder perpendicular to the long axis of the detector. All particles have momenta only in the positive x-direction and the values of momenta at the entry point of the Al cylinder for ^{12}C (180 MeV/u), ^{20}Ne (400 MeV/u) and ^{28}Si (350 MeV/u) are found to be 7.071 GeV/c, 18.759 GeV/c and 24.022 GeV/c respectively. The distribution of the incident positions of the ions is shown in Figure 3.4. The distribution of the droplet centers and incident positions are generated outside the GEANT code, using the SRAND random number generator [54].

The linear energy transfer, $\frac{dE}{dx}$, within a droplet is obtained from the GEANT code. A true bubble nucleation event is assumed to occur if $\frac{dE}{dx}$ is greater than the critical energy deposition $(\frac{W}{kr_c})$ required for nucleation. Extra events due to more than one nucleation for same droplet are rejected. The normalized count, $\frac{1}{N_0.I_B}(\frac{dN}{dt})$ in unit of cm^2, is calculated and plotted as a function of the operating temperature.

3.2.2 Simulation II

This simulation is carried out to first find the probability of nucleation of a droplet for the three ions, ^{12}C (180 MeV/u), ^{20}Ne (400 MeV/u) and ^{28}Si (350 MeV/u) and then, using this probability, the normalized count rate and the nucleation

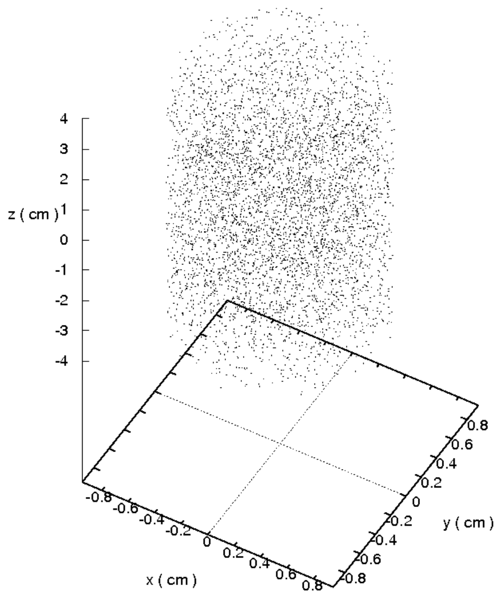

Figure 3.3: Distribution of center of droplets of R-114 in Simulation I.

parameter for the above mentioned experiment are obtained. In this simulation only one single droplet of liquid R-114 of diameter 20 μm is created. To include the actual experimental situation of the randomness in the incident positions of the ions within a droplet, a total of 100 incident positions within the droplet are generated using the SRAND random number generator [54]. On each incident position an ion with the same energy is made to fall 3000 times. The energy losses of the ions during their passage through air are taken into account and calculated using SRIM 2008. As a result, the momenta of ^{12}C (180 MeV/u), ^{20}Ne (400 MeV/u) and ^{28}Si (350 MeV/u) at the incident points within the droplet are 7.071 GeV/c, 18.759 GeV/c and 24.022 GeV/c respectively. The momentum is only in the positive x-direction. The energy deposition as well as LET of the ion along its track through the droplet are obtained from the GEANT code. The distribution of LET for the ion has been obtained for each temperature. In Figure 3.5 the distribution of LET within a 20 μm diameter droplet for ^{12}C, ^{20}Ne and ^{28}Si with above mentioned momenta are shown for a temperature of 50 °C. The density of

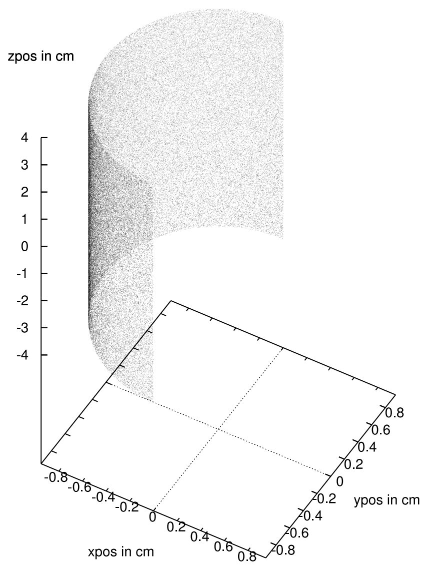

Figure 3.4: Distribution of 2.6 million of incident positions of the ions on the outer surface of the Al cylinder in Simulation I. For clarity, only 0.1 million incident positions are shown. Note that the random distribution of the incident points spans almost a continuous surface.

R-114 liquid at different temperatures are obtained from the fitted functional form using Equation (3.1). Using the distribution of LET, the probability of bubble nucleation of a droplet has been calculated for each temperature for different values of nucleation parameter (k). We defined the probability of bubble nucleation of a droplet (P_B) for a particular nucleation parameter (k) as,

$$P_B = \frac{\text{No. of hits with LET greater than } \frac{W}{kr_c}}{\text{Total number of hit}} \,. \tag{3.2}$$

It is seen that, for any given temperature, the probability reaches a saturation value as the value of k is increased. For illustration, this probability P_B as a function of the nucleation parameter k, for various temperatures, is shown in Figure 3.6 for the heavy ion ^{12}C (180 MeV/u) with incident momentum 7.071 GeV/c. To obtain the number of bubble nucleation events due to a particular ion with a particular

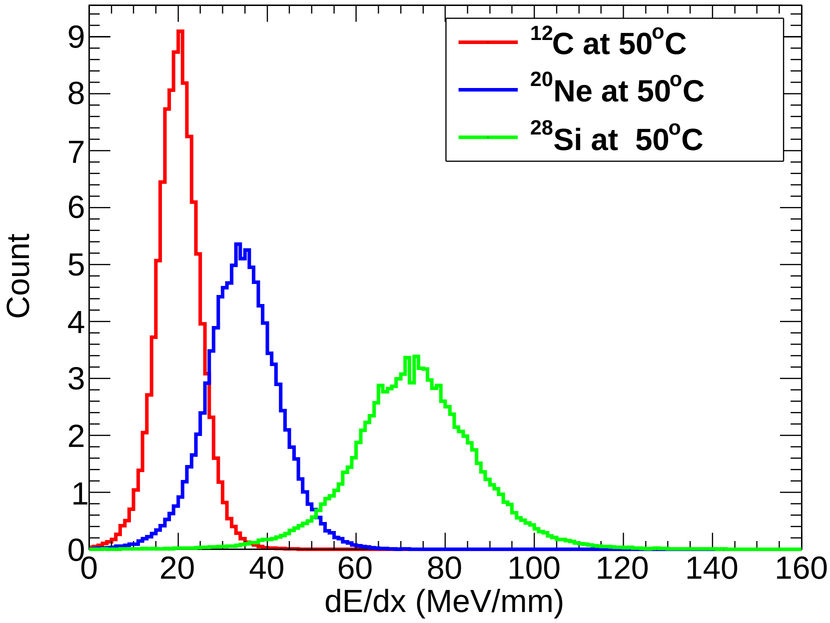

Figure 3.5: Distribution of LET within a 20 μm diameter R-114 droplet obtained at 50 °C from GEANT3.21 for the simulation of ^{12}C (180 MeV/u), ^{20}Ne (400 MeV/u) and ^{28}Si (350 MeV/u). The red, blue and green curves are for ^{12}C (180 MeV/u), ^{20}Ne (400 MeV/u) and ^{28}Si (350 MeV/u) with momenta 7.071 GeV/c, 18.759 GeV/c and 24.022 GeV/c, respectively.

nucleation parameter, the probability of bubble nucleation at that value of the nucleation parameter for that ion is multiplied by the total hit points obtained from Simulation I for the same ion. Finally the normalized count, $\frac{1}{N_0.I_B}(\frac{dN}{dt})$ in unit of cm^2, is calculated and plotted as a function of temperature.

3.3 Results and Discussions

3.3.1 Simulation I

From Simulation I, we have obtained the normalized count rates for different temperatures. Varying the value of k, the response has been fitted with the experimental result. To find the value of k, the normalized count rate (N_{expt}) at the

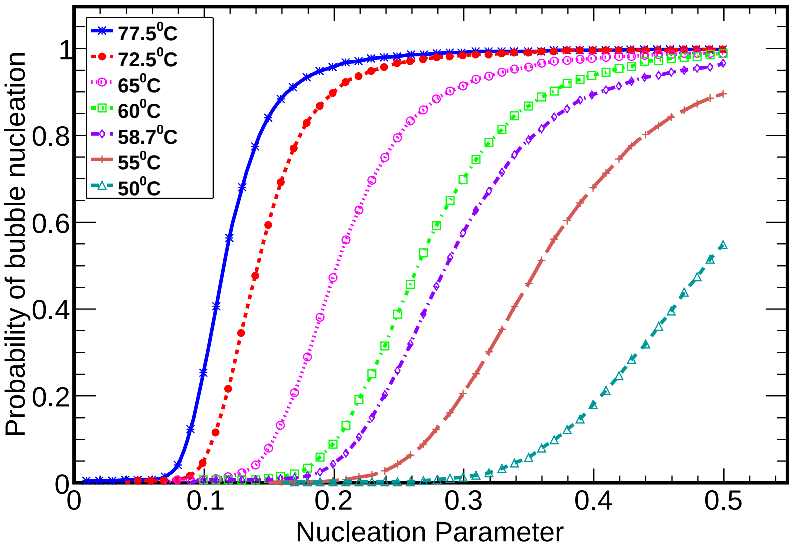

Figure 3.6: Probability of bubble nucleation as a function of nucleation parameter k for ^{12}C (180 MeV/u) with incident momentum 7.071 GeV/c.

experimentally estimated threshold temperature and that obtained from the Simulation I (N_1) are compared. Experimentally at low temperatures the response was almost flat at a value of 5×10^{-7} cm^2 corresponding to background. Above a certain threshold temperature, the number of counts rises sharply [25]. The experimental threshold temperature ($T_{\rm th}$) is considered at the midpoint between the temperature at the end of the above mentioned flat region of the curve and the temperature corresponding to the next higher count above the background count of 5×10^{-7} cm^2. The normalized count rate at the threshold temperature so defined is taken to be the mean of the two counts at the two corresponding temperatures. The same procedure is adopted here to find the normalized count rate (N_1) at the threshold temperature.

In Table 3.1, the normalized count rates at the threshold temperature from the experiment and Simulation I with different values of k are tabulated. The value of k for which the deviation between experiment and Simulation I is least is taken as the best value of k for a particular ion. The deviation for Simulation I is

Table 3.1: Normalized count rate obtained from simulations by varying the nucleation parameter (k) and compared with experimentally obtained values.

Ion (energy in Mev/u) and T_{th}(°C)	Experiment Normalized count at T_{th} (10^{-7} cm^2) (N_{expt})	Value of k	Simulation I Normalized count at T_{th} cm^2 (N_1)	Simulation I Δ_1^2	Simulation II Normalized count at T_{th} cm^2 (N_2)	Simulation II Δ_2^2
^{12}C (180)	5.45	0.24	6.8×10^{-7}	0.061	0 7.68×10^{-7}	0.167
58.7±1.2		0.23	3.93×10^{-7}	0.078	5.61×10^{-7}	0.001
		0.22	3.41×10^{-7}	0.140	3.9×10^{-7}	0.081
		0.21	6.3×10^{-8}	0.782	2.54×10^{-7}	0.285
		0.19	7.0×10^{-9}	0.974	8.72×10^{-8}	0.706
		0.11	0	1.000	7.64×10^{-11}	1.000
^{20}Ne (400)	8.1	0.23	3.126×10^{-6}	8.175	3.60×10^{-6}	11.864
62.5±2.5		0.12	1.551×10^{-6}	0.837	1.09×10^{-6}	0.119
		0.11	2.8×10^{-7}	0.428	6.29×10^{-7}	0.050
		0.10	1.2×10^{-7}	0.726	2.83×10^{-7}	0.423
^{28}Si (350)	5.6	0.23	3.192×10^{-6}	22.090	3.81×10^{-6}	33.681
57.5±2.5		0.08	1.598×10^{-6}	3.436	1.39×10^{-6}	2.197
		0.07	8.32×10^{-7}	0.236	4.90×10^{-7}	0.016
		0.06	1.2×10^{-8}	0.958	8.67×10^{-8}	0.714
		0.05	1.00×10^{-9}	0.996	7.91×10^{-9}	0.972

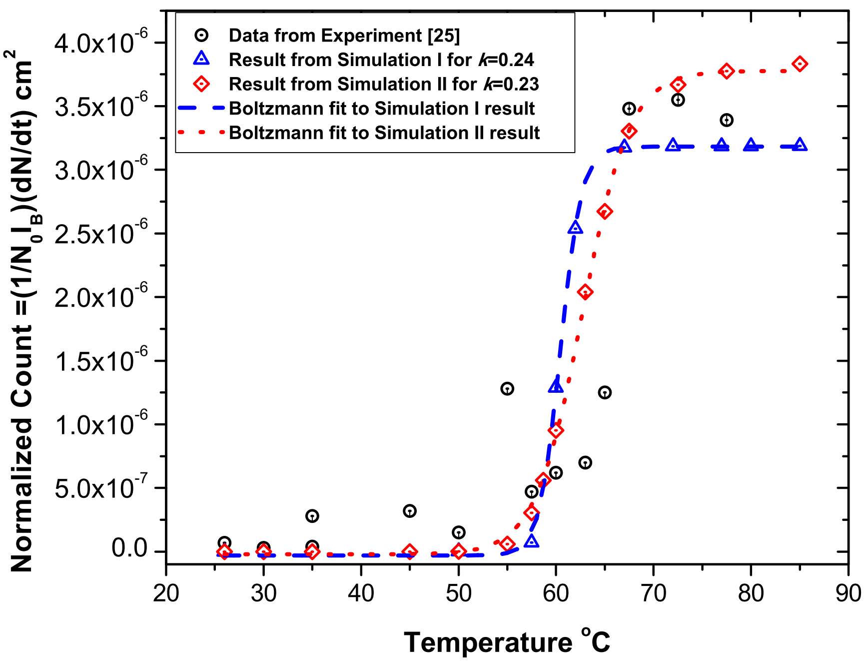

Figure 3.7: Simulation results for ^{12}C (180 MeV/u) ion.

defined as $\Delta_1^2 = (1 - \frac{N_1}{N_{\text{expt}}})^2$. In case of ^{12}C (180 MeV/u), the deviation (Δ_1^2) is smallest for nucleation parameter $k = 0.24$. For the other two heavier ions, ^{20}Ne (400 MeV/u) and ^{28}Si (350 MeV/u), the deviation is smallest for the values of nucleation parameter 0.11 and 0.07 respectively. The normalized count rate as a function of temperatures for the best value of k obtained above for Simulation I (blue triangles in Figures 3.7, 3.8, 3.9) are fitted to the Boltzmann function (blue dashed line in Figures 3.7, 3.8, 3.9) given by

$$y(T) = \frac{(A_1 - A_2)}{(1 + e^{\frac{(T-T_o)}{dT}})} + A_2 \,,$$

where $y(T)$ is the normalized count at temperature ($T\,^\circ$C) and A_1 is the base line value and A_2 is the plateau value of the count rate. The values of the thermodynamic efficiency, η_T for ^{12}C (180 MeV/u), ^{20}Ne (400 MeV/u) and ^{28}Si (350 MeV/u)

Table 3.2: Nucleation parameter (k) and thermodynamic efficiency (η_{T}) for different heavy ions in R-114 liquid obtained from Simulation I and Simulation II.

Ion	Incident energy MeV/u	Mass no.	k obtained from		η_{T} obtained from k	
			Simulation I	Simulation II	Simulation I	Simulation II
^{12}C	180	12	0.24	0.23	0.12	0.115
^{20}Ne	400	20	0.11	0.11	0.055	0.055
^{28}Si	350	28	0.07	0.07	0.035	0.035

from Simulation I is 0.12, 0.055 and 0.035, respectively (see Table 3.2).

3.3.2 Simulation II

A similar procedure as described above for Simulation I is followed to obtain the nucleation parameter (k) and thermodynamic efficiency (η_{T}) from Simulation II. The normalized count rates (N_2) for different values of nucleation parameter (k) at the threshold temperature obtained from the simulation are shown in Table 3.1. The deviation is calculated using the equation $\Delta_2^2 = (1 - \frac{N_2}{N_{\mathrm{expt}}})^2$. It is seen that the smallest deviation Δ_2^2 is obtained for k values of 0.23, 0.11, 0.07 for ^{12}C (180 MeV/u), ^{20}Ne (400 MeV/u) and ^{28}Si (350 MeV/u) respectively (Table 3.1). The response obtained from Simulation II for ^{12}C (180 MeV/u), ^{20}Ne (400 MeV/u) and ^{28}Si (350 MeV/u) ions are shown as red dotted line in Figures 3.7, 3.8, 3.9, respectively. The thermodynamic efficiency (η_T) for the same set of ions are 0.115, 0.055 and 0.035, respectively (Table 3.2).

3.3.3 General observations

From Simulation I and II, η_{T} is found to be in the range of 3.5% to 12%. The values of k and η_T in R-114 liquid for different heavy ions as obtained from Simulation I and II are shown in Table 3.2. From Table 3.2, comparing the value of k from the two simulations, it is seen that for ^{28}Si (350 MeV/u) and ^{20}Ne (400 MeV/u),

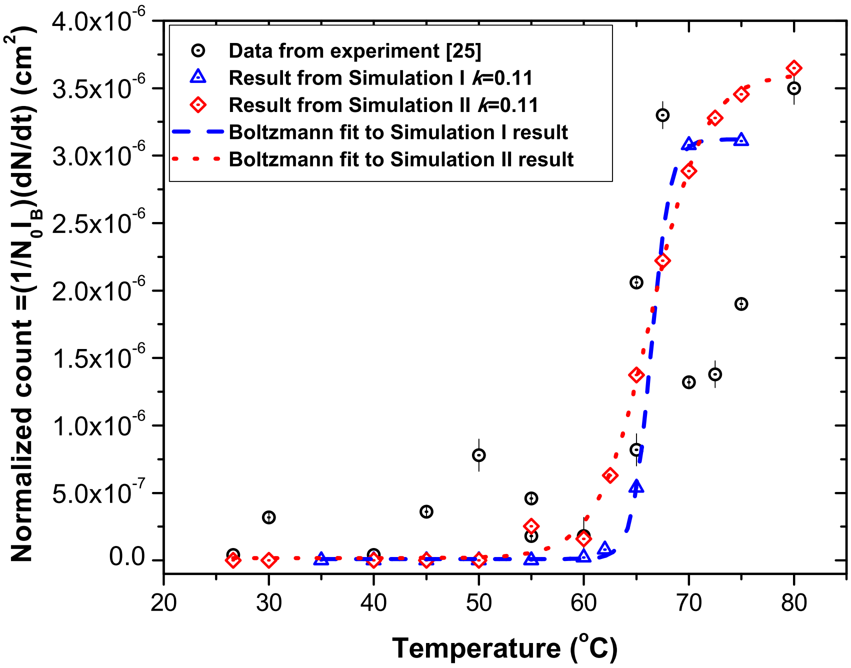

Figure 3.8: Simulation result for ^{20}Ne (400 MeV/u) ion.

the values of k are same and these are 0.07 and 0.11, respectively, while for ^{12}C (180 MeV/u) values of k are 0.24 and 0.23 from Simulation I and Simulation II, respectively. Our results show that the value of k varies with the mass number of the ions. It can be explained by comparing the mean value of LET distribution within a 20 μm droplet obtained from the GEANT code. The mean value of LET for ^{28}Si (350 MeV/u) and ^{20}Ne (400 MeV/u) are 73.14 MeV/mm and 34.50 MeV/mm respectively. These values are greater than that for ^{12}C (180 MeV/u) (20.11 MeV/mm) (see Figure 3.5). By definition η_T is the fraction of energy deposition required for bubble nucleation and as η_T decreases with increase of LET, this implies that thermodynamic efficiency (η_T) (and, hence, correspondingly nucleation parameter (k)) is lowest for ^{28}Si and highest for ^{12}C.

We have also done a separate calculation to obtain the value of nucleation parameter using the result from Simulation I. In this calculation all the experi-

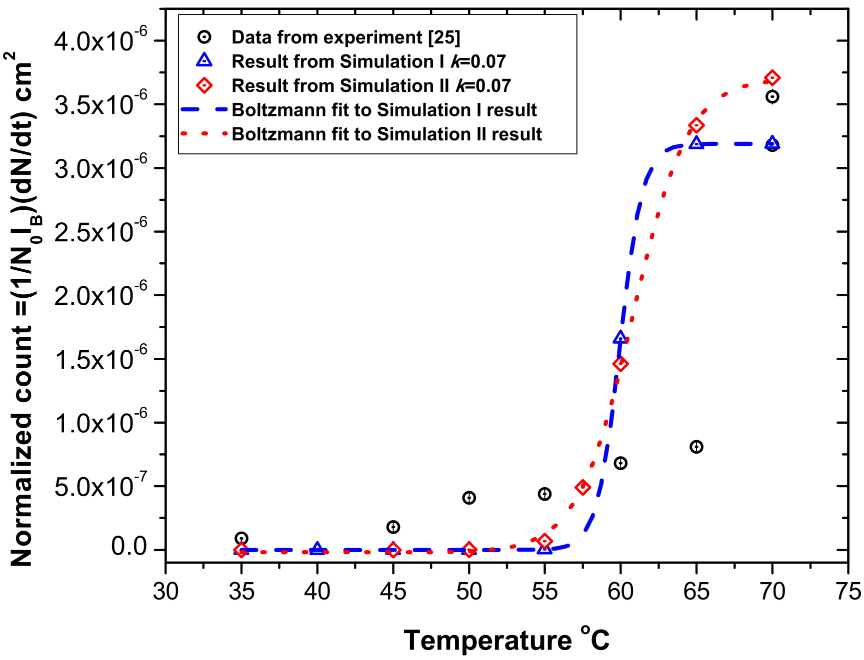

Figure 3.9: Simulation result for ^{28}Si (350 MeV/u) ion.

Table 3.3: Nucleation parameter (k) for different heavy ions in R-114 liquid obtained using simulation I and all experimental data for C, Ne, Si.

Ion	Incident energy MeV/u	Mass no.	k	Deviation obtained using Equation (3.3)
^{12}C	180	12	0.19	0.725
^{20}Ne	400	20	0.11	0.784
^{28}Si	350	28	0.05	0.783

mental results for the whole temperature range used in the experiment and for all the three ions C, Ne and Si are considered. Varying the value of k and using the experimental data for all the three ions, a best fitted single simulation curve has been independently found for each of the three ions, ^{12}C (180 MeV/u), ^{20}Ne (400 MeV/u) and ^{28}Si (350 MeV/u). The deviation between the experimental and the simulated normalized count rate has been calculated for all experimental data using the following formula,

$$\text{deviation} = \frac{1}{N}\left[\sum_{i=1}^{N}\left(1 - \frac{N_i^{\text{sim}}}{N_i^{\text{expt}}}\right)^2\right], \tag{3.3}$$

where, i represents the number of experimental data, N is the total number of experimental data available for the three ions, obtained from [25], N_i^{expt} and N_i^{sim} are the normalized count rate corresponding to a particular temperature from experiment and Simulation I respectively. The best fitted single simulation curve for each ion corresponds to a nucleation parameter k for which the deviation is smallest. For ^{12}C (180 MeV/u), ^{20}Ne (400 MeV/u) and ^{28}Si (350 MeV/u) the nucleation parameter (k) is found to be equal to 0.19, 0.11 and 0.05, respectively (Table 3.3), which also shows the dependence of k on the mass number of the ions.

We should mention that, as evident from the Figures above, there are some deviations of the simulation results from the actual experimental data points. This is only to be expected. There can be several reasons for this. For example, in the simulations described above, we have not included the effects of possible fluctuation of the flux of the incident particles during the experiment. Also, we have considered all the droplets to be of a fixed size, rather than a possible distribution of the radii of the droplets in the actual experimental situation. Furthermore, possible spontaneous nucleations due to impurities in the real detector are not considered. All these effects may, to varying degrees, contribute to the deviations between the simulated results and experimental data points seen in the Figures above. However, the important point to note is that the simulations do reproduce the broad nature of the experimental response curve. This, we believe, indicates that our simulations do indeed capture the essential physics of the nucleation process under consideration.

3.4 Conclusions

We have studied the response of superheated droplet detector to incident heavy ions, ^{12}C (180 MeV/u), ^{20}Ne (400 MeV/u) and ^{28}Si (350 MeV/u) to understand the dependence of the bubble nucleation process on the masses of the incident nuclei. We have done this by simulating the energy losses (LET) by the nuclei during their passage through the active liquid droplets that constitute the detector. Our simulation also includes the geometry of the detector used in the actual experiment. We have determined the nucleation parameter, k, by comparing the simulation results with those from experiment. It is observed from the result that the value of the nucleation parameter, k for ^{12}C (180 MeV/u) is higher than that of the higher mass ions like ^{20}Ne (400 MeV/u) and ^{28}Si (350 MeV/u). For the three ions investigated here, k is observed to decrease with the increase in mass of the heavy ions. The present simulation provides an important observation that the nucleation parameter, (k) depends on the mass number of the ions.

Chapter 4

Discrimination between neutron and gamma ray induced bubble nucleation in Superheated Droplet Detector

4.1 Introduction

Superheated droplet detector is used for both neutron detection and cold dark matter WIMPs (Weakly Interacting Massive Particles) search experiments under different operating temperatures and pressures. For neutron detection, the type of the detector liquid normally used are R-12 (CCl_2F_2; b.p. -29.8 °C), R-114 ($C_2Cl_2F_4$; b.p. 3.7 °C), R-134a ($C_2H_2F_4$; b.p. -26 °C) etc. High energy X-ray radiotherapy machines are known to generate neutrons by photodisintegration or electron-disintegration of atomic nuclei in various components of the accelerator, from various parts of the patient treatment room and the patient's body [55]. Superheated droplet neutron dosimeter is a promising dosimeter for measuring neutron dose equivalent in and around the radiotherapy beam and in patients in the presence of large background of photon flux (three to four orders of magnitude larger than neutrons) [56]. As discussed in Chapter 2 the threshold energy (W) for the SDD depends on temperature and pressure and the types of the sensitive liquid used in the detector. Thus the detector can be made insensitive to gamma rays while being sensitive to neutrons by varying the ambient temperature and pressure of the liquid. This property of the detector makes it a very useful tool in neutron dose measurement in a strong background of gamma rays. Photon sensitive temperature of different halocarbon and hydrocarbon and electron energy deposition were investigated by d'Errico and an empirical formulation was established which states that the gamma sensitive temperature would be the midpoint between the boiling point and the critical temperature of the liquid [10]. It also showed that the photon may trigger bubble vaporization via secondary electrons at their peak ionization density [10].

Superheated liquids C_4F_{10}, C_2ClF_5 (b.p. -38.9 °C), CF_3I (b.p. -21.8 °C) etc. are used for dark matter search experiments [16, 17, 18]. WIMP induced nuclear recoils are similar to neutron induced nuclear recoils. By varying the operating condition, using different liquids of different boiling points and compositions, and employing different pulse analysis techniques, neutron, α-particle, γ - ray etc., that are known to be responsible for the background events in cold dark matter search experiment, can be identified. The dark matter search experiments that use superheated liquids as detector, namely, COUPP, PICASSO and SIMPLE, employ different techniques that can also discriminate between neutron and alpha particle induced events [18, 57, 58]. It is found that alpha induced signals are in general of larger amplitudes than that of neutrons. In order to detect the WIMP induced nuclear recoils with lower energy, the detector must have a relatively low threshold energy. At the low value of threshold energy, detectors also become sensitive to gamma ray induced nucleation events. Thus the ability to effectively distinguish between neutron- and γ- ray induced nucleation events in SDD detectors is an important requirement for the use of SDDs in WIMP DM search experiments.

In the present Chapter, we present a comparative study of two different liquids, namely, R-114 and C_4F_{10}, with regard to their ability to discriminate between neutron - and γ - ray induced nucleation events in a mixed neutron - γ radiation field.

4.2 The experiment

In the experiment, we have fabricated separate SDDs with droplets of superheated liquids R-114 and C_4F_{10} embedded in a viscous aquasonic gel medium the main composition of which is glycerol. The droplets are produced by adding the liquid on the top of degassed soft supporting gel medium in a stainless steel high pressure chamber and by stirring the liquid by a stirrer rotated with variable speed motor. The fabrication procedure is similar to as described in the literature by B. Roy et al. [59].

The detectors are placed inside a water bath and the temperature of the bath is controlled by a temperature controller (Metravi, DTC-200) with precision $\pm 1\,^{\circ}$C (shown in Figure 4.1). The acoustic pulse associated with the process of bubble nucleation in liquid droplets is measured by a condenser microphone with a frequency response up to about 30 kHz, and the traces of the electrical pulse output are recorded in digital storage oscilloscope (Agilent Technologies, MSO7032A; 350MHz, 2GSa/s). The commercially available condenser microphone contains two parallel plates of which one is made of a very light material and acts as a diaphragm. The diaphragm vibrates when struck by sound waves. This changes the distance between the two plates and as a result, its capacitance. This gives a

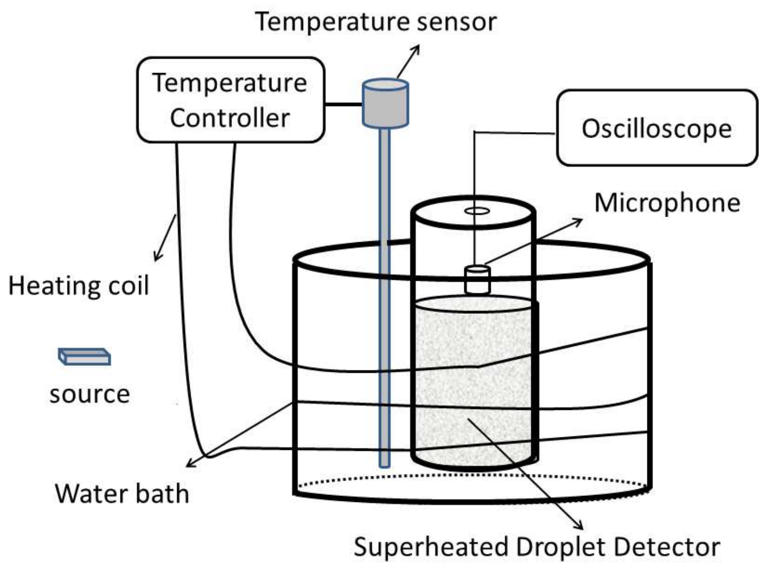

Figure 4.1: Schematic diagram of experimental set up to measure the acoustic response of neutron and γ-ray induced events in presence of different sources.

corresponding electric signal and the intensity of the electric signal depends on the intensity of the acoustic pulse falling on it. The development of the electronic circuit with the condenser microphone is described in the Ref. [60]. The low frequency signal is associated with the final stage of bubble nucleation. After complete phase transition of a droplet, a freely oscillating vapour bubble is formed which oscillates around its equilibrium radius and the ambient equilibrium pressure with a resonant frequency (e.g., 6 kHz for C_4F_{10}) that depends on the density of the surrounding medium [61].

The responses of SDD with sensitive liquid C_4F_{10} in presence of ^{137}Cs (32.5mCi) γ - source is measured by varying the temperature of the detector in the range of 30-60 °C at the ambient pressure of 1 atmosphere to identify the gamma sensitive temperature for this liquid. In a previous experiment [60], the response of SDD to ^{252}Cf was measured using superheated droplets of R-114 as sensitive liquid by varying the temperature of the detector in the range 35-75 °C. The result of this experiment clearly indicated the existence of two distinct steps in the response of SDD of R-114 to ^{252}Cf. The first step at the lower temperature is responsible for the nucleation due to neutrons and the second one near 70 °C is due to gamma rays from ^{252}Cf. Once the γ-ray sensitive temperature is identified for two liquids, the experiments are performed at a temperature which is lower than the γ-ray sensitive temperature to acquire the traces of the neutron induced events. In this way, the measurement for neutron induced nucleation events becomes free from the γ-ray induced nucleation events.

The experiments are performed in presence of a ^{252}Cf (3.2 μCi) fission neutron source at the neutron sensitive temperatures of 55 °C for R-114 and 35 °C for C_4F_{10}. The experiments are also done at both neutron - and γ sensitive temperatures of 70 °C for R-114 and 55 °C for C_4F_{10}. To observe spontaneous nucleations in R-114 droplets, experiments are performed at two different temperatures, 55 °C and 70 °C, in absence of source. In separate experiments, the detector with R-114 liquid is irradiated with a ^{137}Cs (32.5mCi) γ - source at 55 °C, and at 70 °C and above. Similarly, the detector with C_4F_{10} is irradiated with the same γ-source at three temperatures 50 °C, 55 °C and 60 °C. The volume of the detector with R-114 liquid is 10 ml in a 15 ml borosilicate glass vial, while that with C_4F_{10} is 40 ml in a glass vial.

4.3 Results and Discussion

The measurement of the pulse height (H) distribution at temperature 55 °C and 70 °C for ^{252}Cf using SDD with R-114 liquid is shown in Figure 4.2. The results for the same detector irradiated with ^{137}Cs γ-ray source at and above 70 °C are shown in Figure 4.3. The typical waveforms for neutron and gamma induced events in case of R-114 liquid are shown in Figures 4.4 and 4.5 respectively.

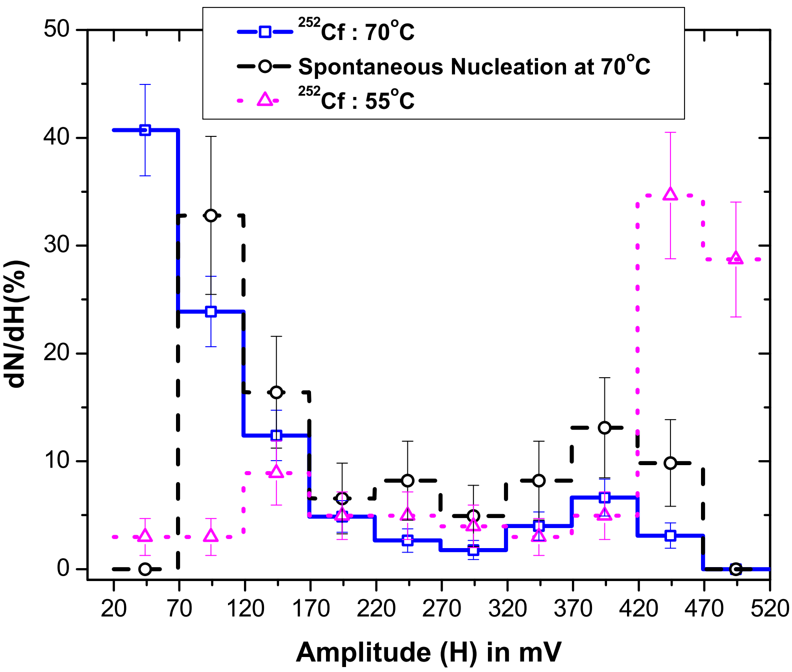

Figure 4.2: Experimentally observed pulse height (maximum) distribution in presence of ^{252}Cf at 55 °C and 70 °C and also for spontaneous nucleation at 70 °C in case of SDD with R-114 liquid.

The measurements at 55 °C with ^{252}Cf are done to observe the pulse height (H) distribution due to neutrons only, while the measurements at 70 °C contains the contribution due to both neutron and gamma induced nucleation events. Figure 4.2 shows that the pulses due to neutrons are of higher amplitudes and lie mainly in the bin of 420-520 mV while the pulses due to γ-rays are of lower amplitudes, mainly lying in the 20-70 mV bin. The observed pulses due to spontaneous nucleation at 70 °C are in between the pulses due to neutrons and γ-rays. Spontaneous nucleation at 55 °C is negligible for R-114 sample used in the present experiment. It is known that spontaneous nucleation occurs in such detector in the absence of any known source, and the rate of spontaneous nucleation increases with increase in temperature until the limit of superheat ($T_{\rm sl}$) is reached [3]. As temperature

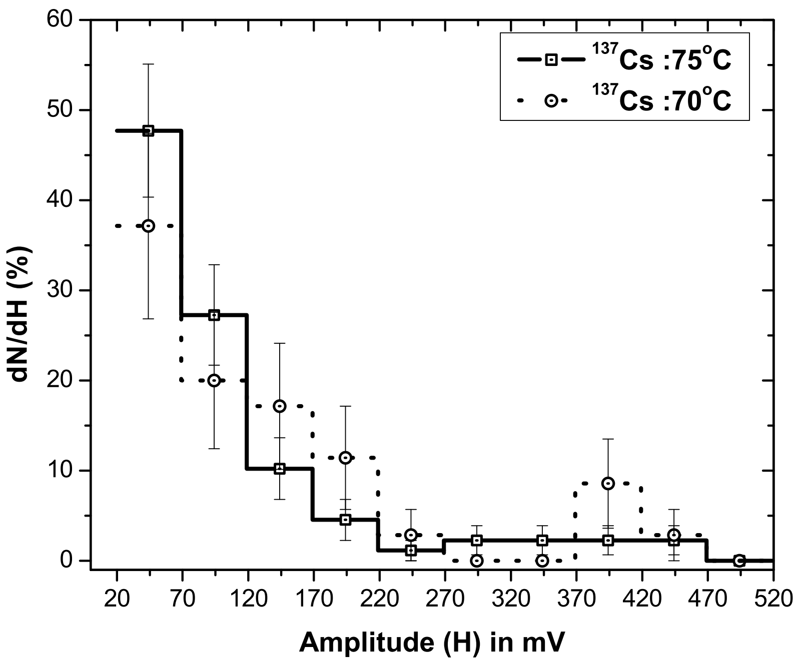

Figure 4.3: Observed pulse height (maximum) distribution of SDD with R-114 liquid in presence of ^{137}Cs at 70 °C and 75 °C.

increases, thermal fluctuation in the droplet can cause bubble nucleation. Therefore, at 55 °C, which is much lower than the critical temperature (T_c = 145.7 °C) of R-114, the spontaneous nucleation is very low. But at 70 °C, the rate becomes significant as it is closer to the critical temperature.

Figure 4.3 shows that the pulses due to ^{137}Cs at 70 °C and 75 °C are generally of lower amplitudes than those observed due to neutron induced events in the case of ^{252}Cf source. For ^{137}Cs no response was observed at 55 °C. This is due to the fact that the detector is insensitive to γ-rays at 55 °C. It is also observed that count rate is higher at 75 °C than that at 70 °C. This is because the probability of nucleation for γ-ray increases with temperature. This observation also confirms that the γ induced nucleation events are of lower amplitudes.

Measurement of maximum amplitude of the pulse provides rough information

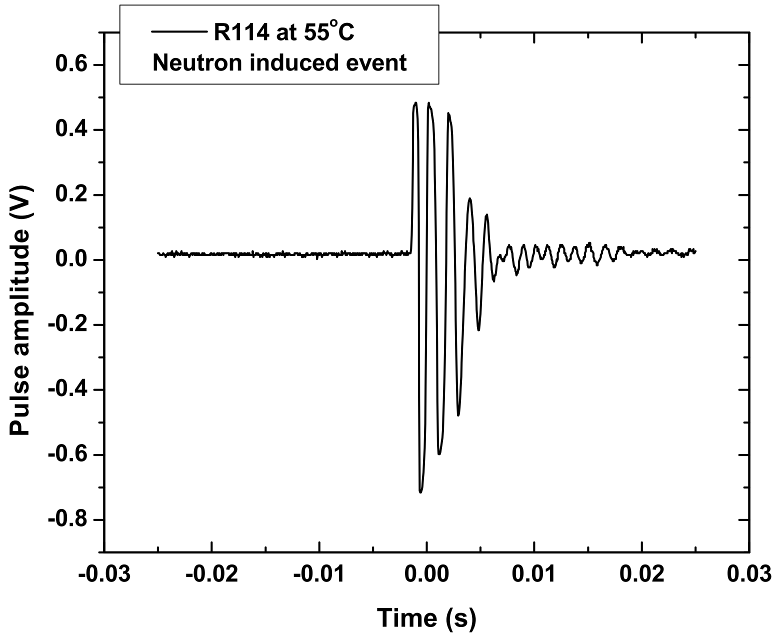

Figure 4.4: Typical waveform of the condenser microphone output for neutron induced nucleation events in SDD with R-114 liquid.

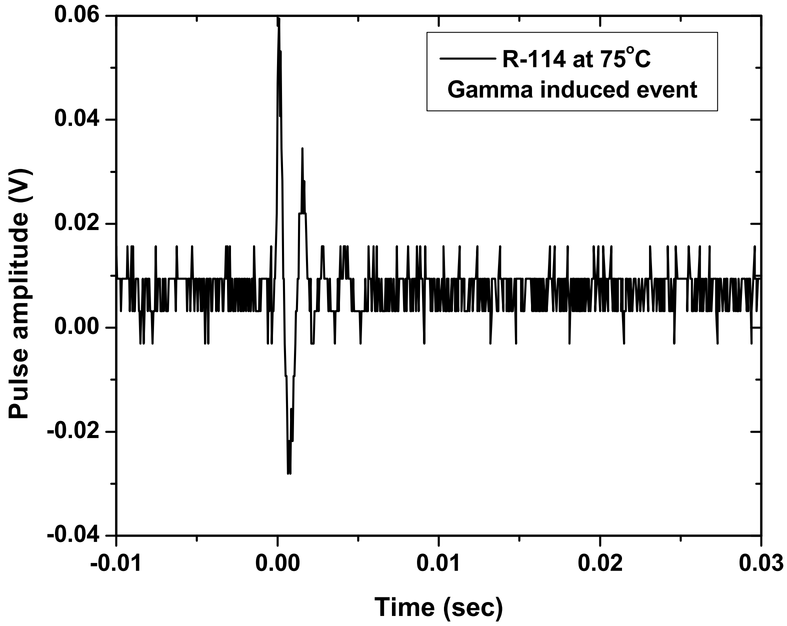

Figure 4.5: Typical waveform of the condenser microphone output for gamma-ray induced nucleation events in SDD with R-114 liquid.

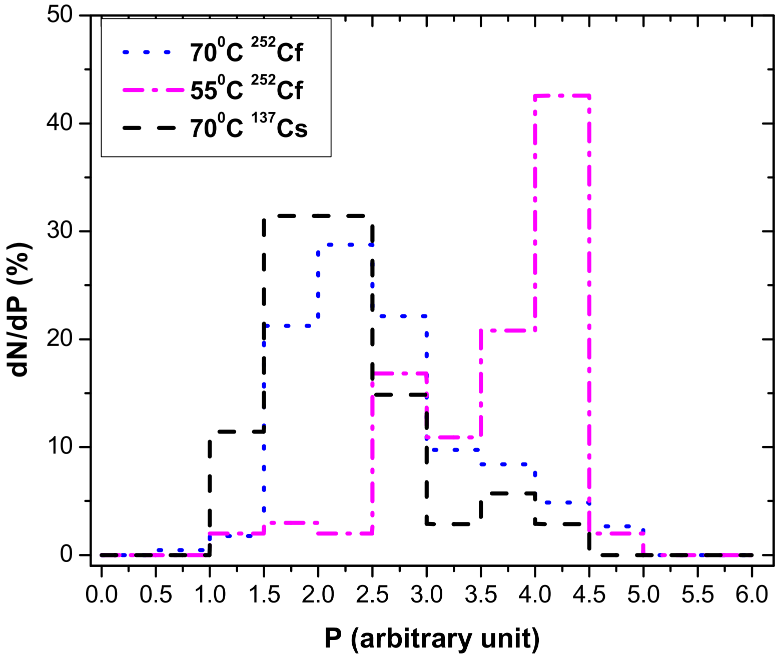

Figure 4.6: Power distribution of the pulses of SDD with R-114 liquid as recorded with ^{252}Cf at 55 °C and 70 °C and with ^{137}Cs at 70 °C.

about the energy deposited and released during the nucleation process. A more precise way of presenting the results is in terms of power. Power is proportional to energy released during the bubble formation process. Therefore, the results are also displayed in Figure 4.6 in terms of power, P [62]. Power is defined as

$$\mathrm{P} = \log_{10}(\sum_i |A_i|^2) \tag{4.1}$$

where A_i is the pulse amplitude in volt of the digitized acoustic pulse (see Figures 4.4 and 4.5) in the i^{th} time bin, and the summation extends over the duration of the signal. In Figure 4.6, P is rescaled to P = 0 corresponding to the lowest value. In Figure 4.6, power distribution of events are displayed for neutron and γ-ray induced events. It is seen that neutron induced events are of higher P than that of γ-ray induced events.

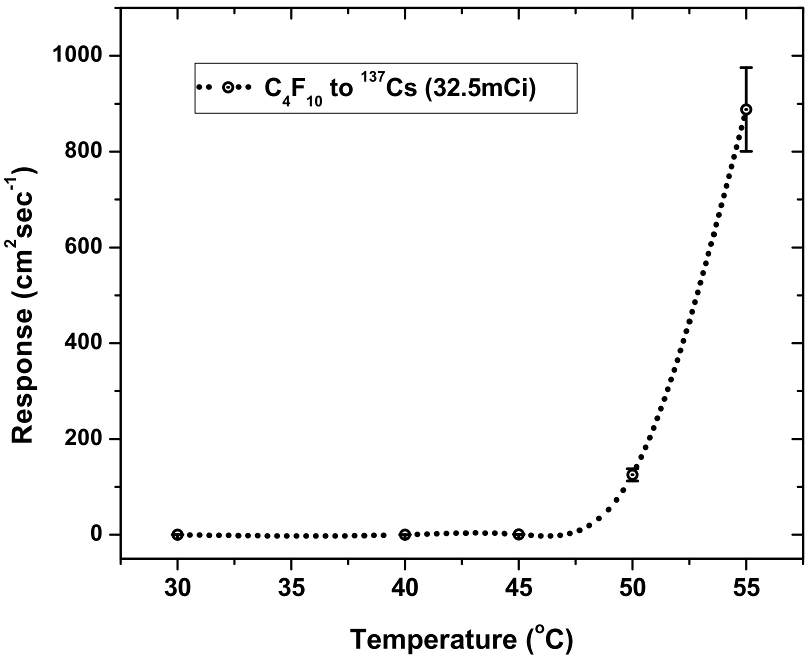

Figure 4.7: Observed response (count rate/particle fluence) of C_4F_{10} detector as a function of temperature in the presence of ^{137}Cs γ-source.

We next study the P-distribution for neutron and γ-ray induced events in SDD with liquid C_4F_{10}. The results of the measurements of count rate of bubble nucleation in SDD with C_4F_{10} in presence of ^{137}Cs γ-source as a function of temperature are shown in Figure 4.7. In the present experiment, the threshold temperature for γ sensitivity of the unpurified detector fabricated in a normal (non-clean room) condition is found to be in the range of $45\,^{\circ}\mathrm{C} < T_{\mathrm{th}} \leq 50\,^{\circ}\mathrm{C}$. Therefore, to study the neutron induced events for this liquid we restrict the operating temperatures of the liquid well below 45 °C, i.e. in the γ insensitive region. We note in this connection that the γ sensitive threshold temperature of purified C_4F_{10} detector, fabricated in clean room environment and irradiated with ^{22}Na (0.7μCi), as reported by PICASSO experiment, is above 55 °C [57, 62]. In Figure 4.8, power distribution of pulses in presence of ^{252}Cf at different temperatures is shown for C_4F_{10} and R-114 liquid. From this Figure it is seen that C_4F_{10} at 35 °C and R-114 at 55 °C are sensitive to neutrons from ^{252}Cf. At the same time C_4F_{10} at 55 °C and R-114 at 70 °C become also sensitive to γ-rays from ^{252}Cf source. It is observed from Figure 4.8 that for R-114, neutron and γ induced events are well separated, while for C_4F_{10} they are not. It is also noticed that the P-distribution for γ induced events for both the liquids, C_4F_{10} and R-114 strongly overlap.

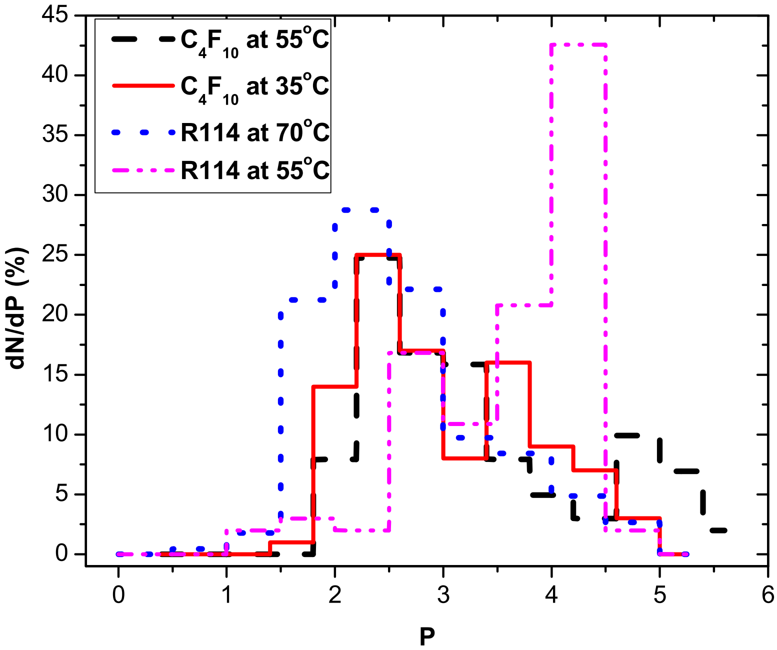

Figure 4.8: Observed power distributions at different temperatures for C_4F_{10} and R-114 detector in the presence of ^{252}Cf fission neutron source.

The recoiling nuclei C, Cl and F produced by incident neutrons have relatively higher LET compared to recoiling electrons produced by incident γ-rays. The electrons deposit their energy in the medium almost at the end of their tracks [10]. Thus the energy deposited by γ-rays is in general much smaller than that due to recoiling nuclei. As discussed in Chapter 2, the threshold energy (W) required for bubble formation decreases with increase in temperature of the detector. Therefore, at lower temperatures only heavy recoils having higher linear energy transfer (LET) in the liquid can trigger bubble formation. At a sufficiently high temperature and correspondingly low threshold energy (W), gamma rays having lower LET can also trigger bubble formation. Besides that, the pulse height and power spectrum are dependent on energy deposited and released during bubble formation. Having higher LET values for nuclear recoils, neutron induced events show higher amplitudes and power than those of the gamma-rays induced events. Details

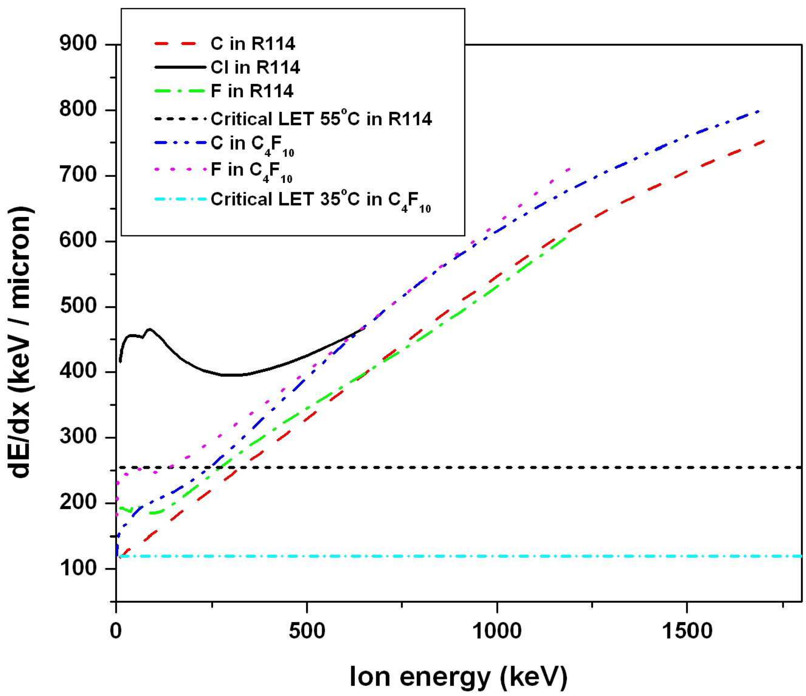

Figure 4.9: Calculated value of LET (dE/dx) of heavy recoils, C, Cl and F in R-114 and for C and F in C_4F_{10} using the SRIM 2008 code along with the critical LET for bubble nucleation in R-114 and C_4F_{10} liquids at 55 °C and 35 °C, respectively.

of the neutron energy spectrum of ^{252}Cf was explained in the Ref. [60, 63]. The $\frac{dE}{dx}$ curves of different constituent nuclei in R-114 and C_4F_{10} are calculated using SRIM code [50] and shown in Figure 4.9. The two horizontal lines (dashed and dashed-dotted) in Figure 4.9 are the critical LETs for bubble nucleation in R-114 at 55 °C and in C_4F_{10} at 35 °C, calculated using Equation (2.7). Figure 4.9 shows that $\frac{dE}{dx}$ of chlorine is much higher in the lower energy region than that of other recoil nuclei, namely carbon (C) and fluorine (F), in both the liquids. The peak energy of neutrons from ^{252}Cf fission neutron source occurs at about 700 keV [63], and the maximum energies of recoil nuclei due to elastic head on collision with neutrons of that energy are 74.6 keV, 198.8 keV, 133.0 keV for chlorine, carbon and fluorine, respectively. Because of the high LET of chlorine at relatively low recoil energy, the energy deposited within the effective path length required for bubble nucleation at a given temperature is larger in R-114 than those due to carbon and fluorine in C_4F_{10}. Therefore, compared to C_4F_{10}, R-114 offers better discrimination between neutron and gamma induced events.

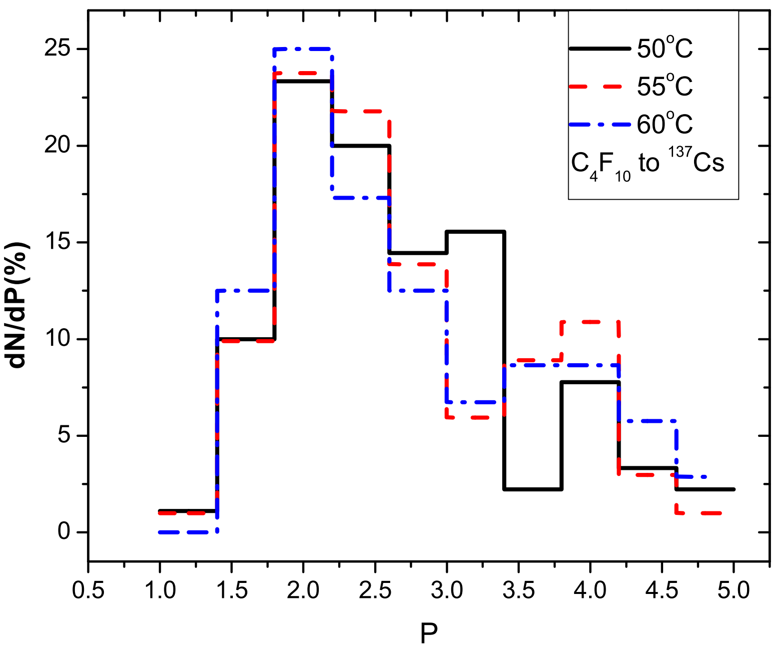

Figure 4.10: Observed power distribution of pulses due to nucleation events in C_4F_{10} detector at different temperatures in presence of ^{137}Cs γ-source.

The power (P) distribution of the pulses obtained at different temperatures for ^{137}Cs γ-ray induced events in C_4F_{10} is shown in Figure 4.10. It has been earlier reported [57] that the peak of the distribution of the integrated signal power, "PVAR", for neutron induced events for C_4F_{10} detector depends on the temperature. The construction of "PVAR" variable is different from that of the power (P) and discussed in details in Chapter 5. The measured temperature dependence of the peaks serves to define the temperature dependent cut on "PVAR" in order to reject the non-particle induced events [57, 62]. On the other hand, our results in Figure 4.10 show that the peak of the power distribution for γ induced events is independent of the operating temperature. This shows that a temperature independent cut on the power distribution can be used to reject the γ induced events in superheated droplet detector employing C_4F_{10} as sensitive liquid in soft aquasonic gel supporting medium for the purpose of neutron detection in mixed neutron - γ radiation field, and also for WIMP search experiment.

4.4 Conclusions

The results of experimental studies with SDD presented in this Chapter clearly demonstrate for the first time, the ability of SDD to identify and discriminate between neutrons and gamma rays by measuring the pulse height distributions of the acoustic pulses in a mixed radiation field. This is very useful in neutron dosimetry and also in WIMP search experiments. A comparative study is performed on the response of R-114 and C_4F_{10} detectors in a mixed neutron - γ radiation field. Using the power distribution of pulses as a diagnostic tool it is observed that R-114 offers a better neutron-gamma discrimination than C_4F_{10}. Although the probability of γ induced nucleation increases with increase in temperature in both liquids, the peak of the power distribution is observed to be independent of the operating temperature in liquid C_4F_{10}. The power distribution of gamma-ray induced pulses falls in the same region, independent of the sensitive liquid R-114 or C_4F_{10}.

Part II

Application of Superheated Droplet Detectors in dark matter search experiment

Chapter 5

Dark Matter and its direct detection

5.1 Introduction

As mentioned in Section 1.2, the Weakly Interacting Massive Particles (WIMPs) are currently one of the most favoured candidates of the Dark Matter (DM) in the Universe. In the following Sections, we review the basic phenomenology of direct detection of WIMP DM particles and then discuss various types of detectors currently in operation. Finally we discuss in details the PICASSO experiment.

5.2 Phenomenology of direct detection of WIMPs

Direct detection experiments look for nuclear recoils produced by the scattering of WIMP with the nuclei of the detector material. Here we shall consider the case of nuclear recoils produced by elastic WIMP-nucleus scattering. In the laboratory frame of reference, the target nucleus is at rest, and the WIMP is incident on it with energy E_χ. After elastic scattering, the WIMP is scattered at an angle ϕ and

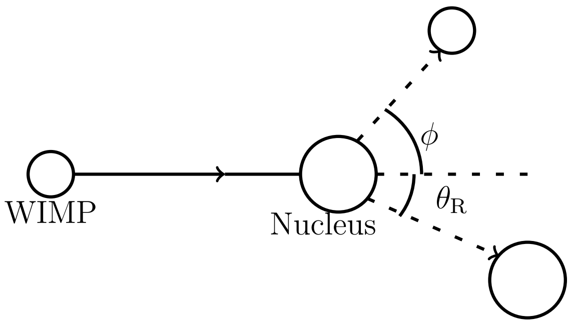

Figure 5.1: Diagram of WIMP-nucleus elastic scattering in Laboratory frame.

the nucleus recoils at an angle θ_{R} which is the angle between the initial direction of WIMP and the direction of motion of the nucleus (see Figure 5.1). Recoil kinetic energy of the target nucleus in terms of the initial energy of WIMP is,

$$E_{\mathrm{R}} = E_\chi \frac{4M_\chi M_{\mathrm{A}}}{(M_\chi + M_{\mathrm{A}})^2} \cos^2 \theta_{\mathrm{R}}, \tag{5.1}$$

where M_χ and M_{A} are the masses of the WIMP and the target nucleus, respectively, $E_\chi = \frac{1}{2} M_\chi v^2$ is the kinetic energy of incident WIMP, and v is the speed of WIMP with respect to the target nucleus.

In the center-of-momentum (CM) system, this same event is seen as two particles coming from opposite direction and scattered at angle θ. The relation between scattering angle in laboratory frame and that in CM frame is $\tan \theta_R = \frac{\sin\theta}{1-\cos\theta}$. So, using this relation in Equation (5.1) we have the nuclear recoil energy in CM frame is,

$$E_R = \frac{4M_\chi M_{\mathrm{A}}}{(M_\chi + M_{\mathrm{A}})^2} E_\chi \frac{(1-\cos\theta)}{2} \tag{5.2}$$

$$\Rightarrow E_R = E_\chi r \frac{(1-\cos\theta)}{2}, \tag{5.3}$$

where

$$r = \frac{4M_\chi M_\mathrm{A}}{(M_\chi + M_\mathrm{A})^2}. \tag{5.4}$$

From the Equation (5.3), we see that the minimum speed (v_{min}) of WIMP that can produce a recoil energy E_R is given by

$$v_{\mathrm{min}} = (\frac{2E_\mathrm{R}}{rM_\chi})^{1/2}. \tag{5.5}$$

In addition, of course, the WIMP in the galaxy should have a maximum speed v_{max} equal to the Galactic escape speed v_{esc}.

The differential event rate per unit mass for a target of atomic mass A_T AMU is

$$\begin{aligned} dR(E_\mathrm{R}) &= \frac{N_A}{A_\mathrm{T}}\,\sigma_{\chi\mathrm{N}}(E_\mathrm{R})\,v\,dn && (5.6)\\ &= \frac{N_A}{A_\mathrm{T}}\sigma_{\chi\mathrm{N}}(E_\mathrm{R})v\,\frac{n_0}{k}\theta(v - v_{\mathrm{min}})\theta(v_{\mathrm{max}} - v)f(\vec{v}, \vec{v_\mathrm{E}})\,d^3\vec{v}, && (5.7) \end{aligned}$$

where N_A = Avogadro number (6.02×10^{26} kg^{-1}),

dn = number density of WIMP with velocities within $d^3\vec{v}$ about $\vec{v}$,

n_0 = mean WIMP number density ($= \rho_\chi/M_\chi$) in the solar neighbourhood,

ρ_χ = mass density of WIMPs in the solar neighbourhood,

$k = \int_0^{v_{\mathrm{max}}} f(\vec{v}, \vec{v_\mathrm{E}})\,d^3\vec{v}$ is a normalization constant,

$\sigma_{\chi\mathrm{N}}(E_\mathrm{R})$ = WIMP-nucleus interaction cross section,

$\vec{v}$ = velocity of WIMP with respect to the target at rest on Earth,

$\vec{v_\mathrm{E}}$ = velocity of Earth (target) relative to the WIMP distribution, and

$f(\vec{v}, \vec{v_\mathrm{E}})$ = the velocity distribution function of the WIMPs.

In Equation (5.7), the θ-functions take care of the fact that only WIMPs of speeds greater than a certain $v_{\rm min}$ can produce a nuclear recoil energy $E_{\rm R}$ (see Equation (5.3)) and the WIMPs in the Galaxy have a maximum speed $v_{\rm max}$.

Total event rate corresponding to recoil energy $E_{\rm R}$ is $\int_{E_{\rm min}}^{E_{\rm max}} dR(E)$, where $E_{\rm max}$ and $E_{\rm min}$ are the maximum and minimum energy of WIMP which can produce recoil energy E_R. We assume that the scattering is isotropic in the CM frame. This means that the recoils are uniformly distributed in the range $0 \leqslant E_{\rm R} \leqslant rE_\chi$. As the distribution of recoil energy is uniform, the differential event rate per unit detector mass (measured in units of counts $\rm keV^{-1}.\ kg^{-1}.\ d^{-1}$) can be expressed as [64],

$$\frac{dR}{dE_{\rm R}} = \int_{E_{\rm min}}^{E_{\rm max}} \frac{dR(E)}{rE_\chi}. \tag{5.8}$$

In our galaxy the velocity distribution of WIMPs is assumed to follow an isotropic Maxwell velocity distribution of form

$$f(\vec{v}, \vec{v_{\rm E}}) = \exp\left(-\frac{(\vec{v}+\vec{v_{\rm E}})^2}{v_0^2}\right), \tag{5.9}$$

where v_0 is the characteristic speed of the WIMPs which is related to the velocity dispersion ($\langle v^2\rangle^{1/2}$) of the WIMPs through the relation $v_0^2 = \frac{2}{3}\langle v^2\rangle$, and $v_{\rm E} = 244\ \rm km\,s^{-1}$ is the speed of Earth relative to the WIMP distribution. Earth moves around sun at an angle $60\,^\circ$ relative to the Galactic plane, and with an average speed of $\sim 30\ \rm km\,s^{-1}$. So, a velocity component of value $\sim 15\ \rm km\,s^{-1}$ is alternatively added to and subtracted from the relative speed between the WIMP and the target nucleus (at rest on Earth), giving rise to an expected annual modulation of the event rate. The local mass density (ρ_χ) of WIMP is assumed to be ~ 0.2 - 0.4 $\rm GeV\,cm^{-3}$ and $v_{\rm esc} \simeq 400$ - $600\ \rm km\,s^{-1}$ is the Galactic escape speed [27]. The differential event rate per unit detector mass (measured in units of counts $\rm keV^{-1}$.

kg^{-1}. d^{-1}) can be obtained from Equation (5.8) and expressed as,

$$\frac{dR}{dE_{\mathrm{R}}} = \frac{1}{rE_0}\int_{v_{\min}}^{v_{\max}} \frac{v_0^2}{v^2} dR(v), \tag{5.10}$$

where $E_0 \equiv \frac{1}{2}M_\chi v_0^2$. Substituting Equations (5.7) and (5.9) in Equation (5.10), we have

$$\frac{dR}{dE_R} = \frac{N_A}{A_{\mathrm{T}}}\sigma_{\chi\mathrm{N}}\frac{n_0}{k}\frac{v_0^2}{rE_0}\int_{v_{\min}}^{v_{\max}} \frac{1}{v}e^{-\frac{(\vec{v}+\vec{v_{\mathrm{E}}})^2}{v_0^2}} d^3\vec{v}. \tag{5.11}$$

Noting that, $(\vec{v}+\vec{v_{\mathrm{E}}})^2 = v^2+v_{\mathrm{E}}^2+2vv_{\mathrm{E}}\cos\theta$, and the maximum value of the WIMP speed is expected to be the escape speed of the WIMP from our galaxy, i.e., $v_{\max}$ = v_{esc}, we have from Equation (5.11),

$$\frac{dR\,(v_E, v_{\mathrm{esc}})}{dE_{\mathrm{R}}} = \frac{N_A}{A_{\mathrm{T}}}\sigma_0 F^2(E_{\mathrm{R}})\frac{n_0}{k}\frac{v_0^2}{rE_0}\int_0^{2\pi} d\phi \int_{v_{\min}}^{v_{\mathrm{esc}}} ve^{-\frac{(v^2+v_{\mathrm{E}}^2)}{v_0^2}} dv \int_{-1}^{+1} e^{-\frac{2vv_{\mathrm{E}}\cos\theta}{v_0^2}} d\cos\theta, \tag{5.12}$$

where we have written $\sigma_{\chi\mathrm{N}} = \sigma_0 F^2(E_{\mathrm{R}})$, with σ_0 being the "zero momentum transfer" cross section (with $F^2(0) = 1$). $F(E_{\mathrm{R}})$ is the energy dependent nuclear form factor. For practical calculations, Equation (5.12) can be approximated as [64]

$$\frac{dR}{dE_R} \approx c_1\frac{R_0}{rE_0}F^2(E_R)\exp(-c_2E_R/rE_0), \tag{5.13}$$

where c_1, c_2 are fitting constants of order unity which include the effect of Earth's velocity with respect to our galactic halo with

$$\frac{c_1}{c_2} = \frac{R(v_{\mathrm{E}}, v_{\mathrm{esc}} = \infty)}{R(v_{\mathrm{E}} = 0, v_{\mathrm{esc}} = \infty)} = \frac{R(v_{\mathrm{E}}, v_{\mathrm{esc}} = \infty)}{R_0}, \tag{5.14}$$

where R stands for total event rate and the coefficients $c_{1,2}$ depend on the chosen values of v_E and v_esc. $c_{1,2} = 1$ for $v_\mathrm{E} = 0$, $c_1 = 0.75$, $c_2 = 0.56$ for $v_\mathrm{E} = 244$ $\mathrm{km\,s^{-1}}$. Note that, R_0 is the total event rate assuming $v_\mathrm{E} = 0$, $v_\mathrm{esc} = \infty$ and 'zero momentum transfer' cross-section ($\sigma_{\chi\mathrm{N}} = \sigma_0 = \mathrm{constant}$) and can be expressed as,

$$
\begin{aligned}
R_0(\mathrm{counts\,kg^{-1}\,d^{-1}}) &= \frac{2}{\sqrt{\pi}}\frac{N_\mathrm{A}}{A_\mathrm{T}}\sigma_0\frac{\rho_\chi}{M_\chi}v_0 && (5.15)\\
&= \frac{403}{A_\mathrm{T}M_\chi}\left(\frac{\sigma_0}{1\,\mathrm{pb}}\right)\left(\frac{\rho_\chi}{0.3\,\mathrm{GeV\,cm^{-3}}}\right)\left(\frac{v_0}{230\,\mathrm{km\,s^{-1}}}\right) && (5.16)
\end{aligned}
$$

The WIMP-nucleus cross-section depends on the target material and on the type of interaction between target material and WIMP. The WIMP-nucleus cross section can be broadly classified into two types, namely, spin-dependent (SD) and spin-independent (SI) interactions. In the SD case, it is primarily the unpaired nucleon inside the nucleus which contributes to the cross section while in the SI case, all the nucleon contribute coherently. Coherent interaction occurs when the wavelength associated with the incoming energy of WIMP is larger than the size of nucleus. In general, the zero momentum transfer interaction cross-section can be expressed as [27],

$$
\sigma_0 = 4G_F^2\mu_\mathrm{A}^2 C_\mathrm{A}, \tag{5.17}
$$

where G_F is the Fermi constant, $\mu_\mathrm{A} = \frac{M_\chi M_\mathrm{A}}{(M_\chi + M_\mathrm{A})}$ is the WIMP-nucleus reduced mass and C_A is the "enhancement factor" which depends on the type of WIMP interaction. For SD and SI interactions, the enhancement factors can be expressed as [27, 64],

$$
\begin{aligned}
C_\mathrm{A}^\mathrm{SD} &= \frac{8}{\pi}\left[a_\mathrm{p}\langle S_\mathrm{p}\rangle + a_\mathrm{n}\langle S_\mathrm{n}\rangle\right]^2\frac{J+1}{J}, && (5.18)\\
C_\mathrm{A}^\mathrm{SI} &= \frac{1}{4\pi}\left[Zf_\mathrm{p} + (A-Z)f_\mathrm{n}\right]^2, && (5.19)
\end{aligned}
$$

where, $a_{\mathrm{p,n}}$ are strengths of effective SD coupling of proton (neutron) with WIMP, $\langle S_{\mathrm{p,n}} \rangle$ are the expectation values of the spin for proton (neutron) in the target nucleus, and J is total nuclear spin. The quantities $f_{\mathrm{p,n}}$ are the strengths of SI WIMP couplings to protons (neutrons) of the target, and Z, A are the atomic and mass number of target nucleus, respectively. The WIMP-nucleus total effective interaction cross-section can be written as a sum of contributions from SD and SI interaction cross-sections.

It is convenient to express this zero momentum WIMP-nucleus cross-sections (σ_0) in terms of zero-momentum WIMP-proton (σ_{p}) and WIMP-neutron (σ_{n}) cross-sections as,

$$\sigma_{\mathrm{p,n}} = \sigma_0 \frac{\mu_{\mathrm{p,n}}^2}{\mu_{\mathrm{A}}^2} \frac{C_{\mathrm{p,n}}}{C_{\mathrm{A}}}, \tag{5.20}$$

where $\mu_{\mathrm{p,n}} = \frac{M_\chi M_{\mathrm{p,n}}}{M_\chi + M_{\mathrm{p,n}}}$ are the WIMP-proton and WIMP-neutron reduced mass, $C_{\mathrm{p,n}}$ are the proton and neutron contributions to the total enhancement factor which can be calculated using Equations (5.18) and (5.19). In the case of spin independent interaction, it is often assumed that coupling to neutron and proton are equal ($f_{\mathrm{n}} \simeq f_{\mathrm{p}}$). In that case, for spin independent (SI) interaction, we get $\frac{C_{\mathrm{A}}}{C_{\mathrm{p}}} \simeq \frac{C_{\mathrm{A}}}{C_{\mathrm{n}}} \simeq A^2$ by using Equation (5.19).

5.3 Detection techniques and current experiments

The kinetic energy of the WIMP-induced recoiling target nucleus is dissipated in detector medium through mainly two processes (i) ionization in liquid/gas material which is similar to the formation of electron-hole pair in solid crystal, and (ii) lattice vibration (phonon generation) in solid crystal. A WIMP detector attempts to pick up signals due to one or both of these processes. Different ways of detection of ionization and phonon signals are used in ongoing experiments: (i) ionization signals as scintillation lights, (ii) direct measurement of ionization signals, (iii) ionization signals as acoustic signals which is caused by heating and (iv) phonon signals as heat.

Below we give a brief review of the basic principles of detectors currently being used in WIMP search experiments.

5.3.1 Detection using scintillation lights

When a charged particle passes through certain kinds of detector materials, a small fraction of the kinetic energy deposited by the charged particle is converted to light. For a given detector material, the fraction of incident energy of particle converted to light depends on the type of particle and its energy. Nuclei in general yield less scintillation light in comparison to that observed for electrons recoil of the same energy. This light can be measured by a 'photomultiplier tube (PMT)' which converts the light flashes to an electrical pulse.

Two types of scintillators are currently used in DM search experiment: (i) solid scintillator (e.g. radio-pure Thallium doped Sodium Iodide (NaI), or Caesium Iodide (CsI)), (ii) liquid scintillator (e.g. noble liquid such as Argon, Neon or Xenon).

There is also a difference between the shapes of PMT pulse due to electron induced scintillation and nuclei induced scintillation in a solid scintillator. For example, the KIMS (Korea Invisible Mass Search) experiment at Yangyang Underground Laboratory (Korea) [65] uses CsI(Tl) crystal and uses pulse shape analysis to discriminate between electronic and nuclear recoil events. DAMA (DArk MAtter) experiment at Gran Sasso (Italy) [66] uses NaI crystals and searches for annual modulation of the event rate expected due to the motion of the Earth around the Sun. The scintillation mechanism in inorganic crystal, such as, NaI, CsI depends on the energy band structure of electrons in the crystal lattice. When a charged particle or photon falls on pure crystal, absorption of energy can elevate electrons from valance band to conduction band by leaving holes in the valance band. The return of electrons from conduction band to valance band is associated with emission of photons typically of ultraviolet wavelengths. However, when a small amount of impurities, called activator, for example Tl, is added to a pure crystal, the energy band structure of the electrons is modified. Energy states are created within the forbidden gap through which the electron can de-excite back to the valence band. Because the energy is less than that of the full forbidden gap, this transition allows the emission of photons with lower energy, in particular, of visible wavelength.

Noble liquids are also used as scintillator medium. The DEAP (Dark matter Experiment using Argon Pulse shape discrimination) at SNOLAB uses liquid argon scintillator. DEAP and CLEAN (Cryogenic Low Energy Astrophysics with Noble liquids) collaborations are presently building the miniCLEAN experiment at SNOLAB, Canada [67, 68] which uses liquid argon or neon scintillator. The XMASS experiment at the Kamioka Observatory (Japan) uses liquid xenon scintillator [69]. Unlike solid scintillator, liquid scintillator is operated at low temperature of about few kelvin and the scintillation mechanism is different from that in solid scintillators. The scattering of the incoming particle gives rise to a recoiling electron (e^-) or nucleus (A^+), where $A \equiv$ Ar, Ne, Xe. A recoiling electron or ion can then excite or ionize another atom of the noble liquid. The excited atoms (A^*) sometimes quickly combines with an atom in the ground-state (A) to form a dimer states (A_2^*). In addition, the ion (A^+) can also combine with a ground-state atom (A) to form an ionized molecule (A_2^+), which can then combine with free electrons (e^-) to form excited dimers. The decay of the dimer state (A_2^*) to ground state produces the observed scintillation light. The pulse shape from PMT due to electron and nuclear induced scintillation can be discriminated using pulse-rise time, the signal intensity at the beginning of the pulse.

Another kind of scintillator detector is the Dual phase (liquid-gas) Time Projection Chamber (TPC) in which the passage of an incoming particle can give rise to two scintillation signals. Again, a noble liquid (e.g. Ar or Xe) is used as target material. There is a cryostat which contains the noble liquid with a layer of gas at its top. The passage of any charged particle through this liquid produces direct scintillation light denoted by (S1) as described in case of liquid scintillator. The electrons which escape recombination are drifted towards the gas phase from their interaction sites by a strong homogeneous electric field. The electrons passing through the gas, produce another scintillation light pulse, called secondary scintillation light pulse (S2). These scintillation lights pulses (S1 and S2) are detected by an array of PMTs, one array immersed in the noble liquid at the bottom of the detector, and another array at the top, in the gas. The S1 and S2 pulses thus correspond respectively to the light and ionization signal produced by a particle interacting with the sensitive volume. S1 and S2 signals can be distinguished from each other by the signal duration. S2 signals are generally of longer in duration than S1 because S2 is produced along the path of electrons in the gas gap between anode and liquid surface.

The ratio of these two scintillation signals is lower for nuclear recoil induced events than electron recoil induced ones, thus allowing discrimination between β and γ induced events (which preferably give rise to electron recoils than nuclear recoils) from those induced by neutrons, WIMPs. It is also possible to obtain information about the energy deposited as well as the location of the interaction point using S1 and S2 signals for each event. The (x, y) position of the interaction site is obtained from the hit patterns of S2 signal on the PMTs in the gas phase and the time difference between S1 and S2 signal multiplied by electron drift velocity provides the z-position of the interaction site.

The XENON experiment at Gran Sasso National Laboratory (LNGS, Italy) [70] and the LUX (The Large Underground Xenon) experiment at the Sanford Underground Research Facility (Lead, South Dakota) [71] both use liquid Xenon as target liquid. The DarkSide experiment at Gran Sasso National Laboratory (LNGS, Italy) utilizes dual phase TPC of liquid Argon [72].

5.3.2 Ionization and phonon signals

Ge and Si detectors are used for simultaneous measurement of direct ionization and lattice vibration (phonon) signals. The experiment is operated at low temperature ($\sim$ few ten mK). The simultaneous measurements of these both ionization and phonon signals allow this type of detector to discriminate between electron and nuclear recoil events.

Ge and Si ZIP (Z-dependent Ionization and Phonon) and iZIP (interleaved Z-sensitive Ionization and Phonon) detectors are used by CDMS collaboration for different phases of the experiment [73, 74]. When a particle interacts with the nucleus of the crystal, some of the deposited energy is used to create electron-hole pairs while the rest goes into vibration (phonon) of the crystalline lattice. The electron-hole pairs are separated and drifted to charge collectors by an electric field applied across the detector. This gives the ionization signal. The phonon signals from the nuclear recoil events are detected by the Transition Edge Sensor (TES). The TES consisting of tungsten coupled to aluminium fins acts as superconducting phase transition thermometer. The temperature of TES is kept at the transition temperature at which the transition from the superconducting state to the normal state happens. The produced phonon propagates through crystal, and when reaches to aluminium fins, phonon transfers its energy to quasi-particle Cooper pair electrons and breaks them. The electrons created in this process diffuse to tungsten and superconducting to normal phase transition occurs due to small increase in temperature. As a result, the resistance of tungsten changes by a large amount which is generally measured by SQUID (superconducting quantum interference device) based electronics.

Recoiling electrons are in general more ionizing than recoiling nuclei of same recoil energy. As a result the electrons generally give rise to a higher ratio of ionization to phonon signal, called "ionization yield". Besides that, phonon signals due to nuclear recoils have longer rise times and occur later than those due to electron recoils. Combined application of ionization yield and phonon-timing cuts allows to reject the background events, namely, gamma, beta radiations.

5.3.3 Scintillation and phonon signals

Scintillator crystals (e.g. $CaWO_4$, $ZnWO_4$) are used to detect phonon along with scintillation light signal. The heavy nucleus, after scattering from a WIMP, receives a very small amount of recoiling energy. To detect this very low amount of recoiling energy the experiment is performed at low temperatures of about $\sim$few ten mK. This energy deposition produces phonon which is measured by TES. In addition to this phonon signal a small fraction of the deposited energy in the crystal produces scintillation light. The ratio of scintillation light signal to phonon signal called "light yield" is used to discriminate between the signals from different types of particles.

CRESST (Cryogenic Rare Event Search with Superconducting Thermometers) experiment at Gran Sasso National Laboratory (LNGS, Italy) [75] measures both phonon signal and scintillation light signal using $CaWO_4$ crystal. In order to mea-

Table 5.1: Detectors used in currently operating experiment.

Detector used	Collaboration name	Underground Laboratory
CsI(Tl) scintillator	KIMS [65]	Yangyang (Korea)
NaI(Tl) scintillator	DAMA [66]	Gran Sasso (Italy)
Liquid scintillator	miniCLEAN [68]	SNO (Canada)
(Argon/Neon/Xenon)	XMASS [69]	Kamioka(Japan)
Dual phase Time Projection	XENON [70]	Gran Sasso(Italy)
Chamber (Xenon/Argon)	LUX [71]	Sanford (US)
	DarkSide [72]	Gran Sasso(Italy)
Ge "ZIP" and iZIP detector	CDMS [73]	Soudan(US)
	SuperCDMS [74]	Soudan(US)
Ge detector	EDELWEISS [76]	LSM(France)
$CaWO_4$	CRESST [75]	Gran Sasso (Italy)
Superheated Droplet Detector	SIMPLE [58]	LSBB (France)
(C_2ClF_5,C_4F_{10})	PICASSO [32]	SNO (Canada)
Bubble Chamber (C_3F_8)	COUPP [18]	FermiLab (US)

sure the scintillation light, each crystal is paired with a separate cryogenic light detector. Each light detector consists of a light absorber and TES. A crystal and the corresponding light detector form a detector module which is enclosed in a common scintillating and highly reflective housing to maximize the collection of the scintillation light. EURECA (European Underground Rare Event Calorimeter Array), a new generation experiment based on the technique of the EDELWEISS [76] and CRESST experiments, uses Zinc tungstate ($ZnWO_4$) crystal for measurement of both phonon signal and scintillation light [77].

5.3.4 Acoustic signals

In Bubble Chamber (BC) and Superheated Droplet Detector (SDD), the interaction with incident particles causes heat which causes phase transition from superheated liquid state to vapour. The basic principle of these detectors has been discussed in the Chapter 2. During the phase transition, an acoustic signal is generated which is acquired by using different types of acoustic sensors. COUPP experiment uses BC with liquid CF_3I, while SIMPLE and PICASSO experiments use SDD of C_2ClF_5 and C_4F_{10} liquids, respectively, for detection of WIMP. At present, PICASSO and COUPP together are using a BC with C_3F_8 (b. p. -36.83 °C) liquid and this new generation experiment is known as PICO experiment. In the next Section, we shall discuss the PICASSO experiment in more details.

Some of the detectors which use the detection principles discussed above are summarized in the Table 5.1.

5.4 Dark matter search with PICASSO detector

As mentioned in Chapter 1 (Section 1.2), the PICASSO detector is currently one of the most sensitive detector for spin-dependent interaction of WIMPs. PICASSO experiment is located at SNOLAB which is an underground laboratory situated 2070 m deep in a nickel mine in Sudbury, Ontario, Canada. Experimental set of PICASSO experiment at SNOLAB is shown in Figure 5.2. A total of 32 detector modules are installed in eight Temperature and Pressures Control Systems (TPCS), each TPCS containing four detector modules (Figure 5.3). Temperature can be controlled with precision $\pm 0.1\,^{\circ}$C. Each detector module of volume about 4.5 litres consists of an acrylic cylinder of height 40 cm and diameter 14 cm, and filled with droplets (radius $\sim 100\ \mu$m) of Perfluorobutane, C_4F_{10} liquid suspended in a polymerized gel matrix. Average active mass of the detector is 90 gm of C_4F_{10} which corresponds to 72 gm of ^{19}F. For each detector module nine piezoelectric transducers (Ferroperm PZ27) are used to acquire the acoustic signals due to incident particles. These transducers are mounted at three different heights of the detector and have pressure sensitivity of 27 μV/μbar.

<u>Detector Calibration :</u>

As discussed in Chapter 2, the minimum critical energy or threshold energy

Figure 5.2: Left: A 4.5 L detector module. Each module is selected with 9 piezo-electric transducers. Right: Experiment set up of 2.6 kg with ultrapure water shielding at new location in SNOLAB (2010). 32 detectors modules are installed in 8 TPCS [78].

of bubble nucleation (E_{c}) depends on the temperature and pressure of a liquid. So a particle having an energy above a certain threshold energy can only trigger nucleation and this energy depends on the temperature and pressure of the liquid. This dependence can be studied with neutron induced recoils. For this purpose measurements have been performed with mono-energetic neutron beams with the detector module kept at a pressure of 1 bar. The neutrons scattering with the liquid C_4F_{10} produce recoiling nuclei of fluorine and carbon. In the center of momentum system, the recoil energy of a nucleus after elastic scattering with neutron can be expressed as,

$$E_{\mathrm{R}}^{i} = \frac{4M_{\mathrm{n}}M_{\mathrm{N}_i}}{(M_{\mathrm{n}} + M_{\mathrm{N}_i})^2} E_{\mathrm{n}} \frac{(1 - \cos\theta)}{2}, \tag{5.21}$$

where E_{n} and θ are the incident neutron energy and the scattering angle in the center of momentum system respectively, and M_{n} and M_{N_i} represent the masses of neutron and target nucleus, N_i, respectively. The quantity, $f_i = \frac{4M_{\mathrm{n}}M_{\mathrm{N}_i}}{(M_{\mathrm{n}}+M_{\mathrm{N}_i})^2}$ corresponding to $\theta = 180^\circ$ gives the maximum fraction of energy of incident neutron transferred to a recoil nucleus. For fluorine and carbon this fraction is of value 0.19 and 0.28, respectively.

Figure 5.3: A Temperature and Pressures Control Systems (TPCS) containing four detector modules.

The mono-energetic neutrons used in calibration are produced via nuclear reaction between mono-energetic proton and targets of Lithium (^{7}Li) and Vanadium (^{51}V). The nuclear reaction, ^{7}Li(p,n)^{7}Be produces neutrons of energies from 100 keV up to 5 MeV and ^{51}V(p,n)^{51}Cr produces mono-energetic neutrons with energy down to 4.8 keV. During measurement, the maximum recoil energy of ^{19}F corresponding to the neutron energy is found to be ranging from 0.9 keV up to 800 keV (see in Figure 5.4). For each selected neutron energy the temperature has been ramped up and down at a fixed pressure to obtain the detector response (count rates). From such curves the threshold temperature (T_{th}) is extracted by extrapolating the curves down to few degrees below the temperature at which the lowest count rate has been measured [16]. By this process one can obtain the neutron energy as a function of threshold temperature at a certain pressure and it is well explained by fitting with an exponential function (shown in Figure 5.4). The threshold energy of neutron ($E_{\mathrm{n,th}}$) and the recoil energy of ^{19}F ($E_{\mathrm{F,th}}$) are given by following relation [62],

$$E_{\mathrm{F,th}} = 0.19E_{\mathrm{n,th}} = (4.93 \pm 0.15) \times 10^3 \exp(-0.173 \times T)(\mathrm{keV}), \tag{5.22}$$

where T is in °C. The pressure is kept at 1 bar. For comparison, the measurements with α-particle induced recoils are shown as open circles at temperatures 21 °C and 25 °C (see Figure 5.4). The point at 21 °C corresponds to the energy deposition by ^{210}Pb of energy 146 keV from the decay chain of α-source ^{226}Ra and at 25 °C for alpha particles at Bragg peak from ^{241}Am α-source.

Detector Response :

With the detector calibration as described above, we now consider the response of the detector for various types of incident particles. It is observed that count rate around the threshold temperature is generally increases with temperature [10]. The response of this type of detector is found to be well described by the probability function, $P(E_{\mathrm{dep}}, E_{\mathrm{th}}(T))$, giving the probability of producing a nucleation event, for an energy deposition of E_{dep} in a liquid with threshold energy $E_{\mathrm{th}}(T)$. The empirical functional form of this probability is [16],

$$P(E_{\mathrm{dep}}, E_{\mathrm{th}}(T)) = 1 - \exp\left(\frac{-\alpha(E_{\mathrm{dep}} - E_{\mathrm{th}}(T))}{E_{\mathrm{th}}(T)}\right), \tag{5.23}$$

where α is a parameter which describes the observed steepness of the threshold energy as a function of temperature and determined experimentally. Larger the value of α, steeper is the detector response with temperature, allowing a more accurate determination of the value of the threshold energy. This parameter describes the

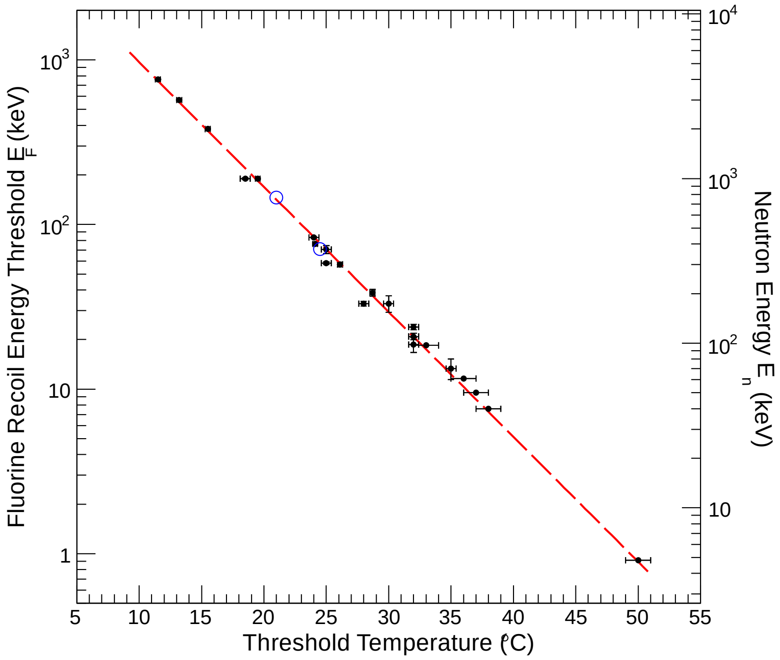

Figure 5.4: The energies of mono-energetic neutrons (shown in right vertical scale) as a function of measured threshold temperature. The left vertical scale represents the maximum recoil energy of fluorine related to the neutron energy. The data shown here is well explained by an exponential dependence on temperature (broken red line). For comparison, the measurements with α-particle induced recoils are shown as open circles at temperatures 21 °C and 25 °C. The point at 21 °C corresponds to the energy deposition by ^{210}Pb of energy 146 keV from the decay chain of α-source ^{226}Ra and at 25 °C for alpha particles at Bragg peak from ^{241}Am α-source. [32].

statistical nature of the energy deposition by a particle and its conversion into heat. The value of α is in general different for different particles. In terms of energy (E_{R}) of the recoiling nucleus, the probability for bubble nucleation given in Equation (5.23) can be expressed as

$$P(E_{\mathrm{R}}, E_{\mathrm{R,th}}(T)) = 1 - \exp\left(\frac{-\alpha(E_R - E_{\mathrm{R,th}}(T))}{E_{\mathrm{R,th}}(T)}\right), \tag{5.24}$$

where $E_{\mathrm{R,th}}(T)$ is the threshold recoil energy at temperature T. The probability of nucleation is zero if $E_{\mathrm{R}} < E_{\mathrm{R,th}}(T)$ and increases gradually up to 1 for $E_{\mathrm{R}} \geq$

$E_{\mathrm{R,th}}(T)$. This function is used to obtain the efficiency of triggering a bubble nucleation at a particular temperature by a recoiling nucleus.

The response of a PICASSO detector to different types of particles as a function of operating temperature of the detector as well as threshold energy of fluorine recoil is shown in Figure 5.5. The temperature is converted to threshold energy of ^{19}F recoil (shown in upper x-axis of Figure 5.5) by using Equation (5.22). In Figure 5.5, the alpha response curve (open triangle with error bars) is obtained after spiking the polymer matrix with ^{241}Am. The threshold temperature corresponds to an energy deposition (E_{dep}) of value 71 keV. The alpha particle of initial energy 5.64 MeV from ^{241}Am source with energy deposition at Bragg peak causes bubble nucleation at that temperature. The lower threshold temperature in case of ^{226}Ra spiked detector (full dots with error bars in Figure 5.5) is due to ^{210}Pb with energy 146 keV from the decay chain of ^{226}Ra. In Chapter 6, we shall discuss in detail about the two different threshold temperatures from two different alpha sources.

The response curve (dot-dashed) for γ-rays in Figure 5.5 has been obtained by irradiating the detector using a gamma source, namely, ^{22}Na (0.7 μCi). Two gamma rays of different energies are produced during decay of ^{22}Na : 1.275 MeV and 511 keV. Former gamma ray is emitted when the daughter nucleus, Neon (^{22}Ne*), decays to ground state from its first excited state and two 511 keV gamma rays are produced from $e^{+}e^{-}$ annihilation process. It has been observed that measurements with gamma rays of energy 127 keV to 1.3 MeV from other sources, namely, ^{57}Co, ^{60}Co, ^{137}Cs give identical response curve [61]. Since the average Z of the detector material is about 5.5, it is expected that the Compton scattering cross section dominates in the energy range from 400 keV to 5 MeV. In the tracks of Compton electrons, δ-rays and Auger electrons are randomly produced which curl up into highly localized region at the end of their trajectories and trigger bubble nucleation. It is observed from simulation results that energy spectra of the δ-ray

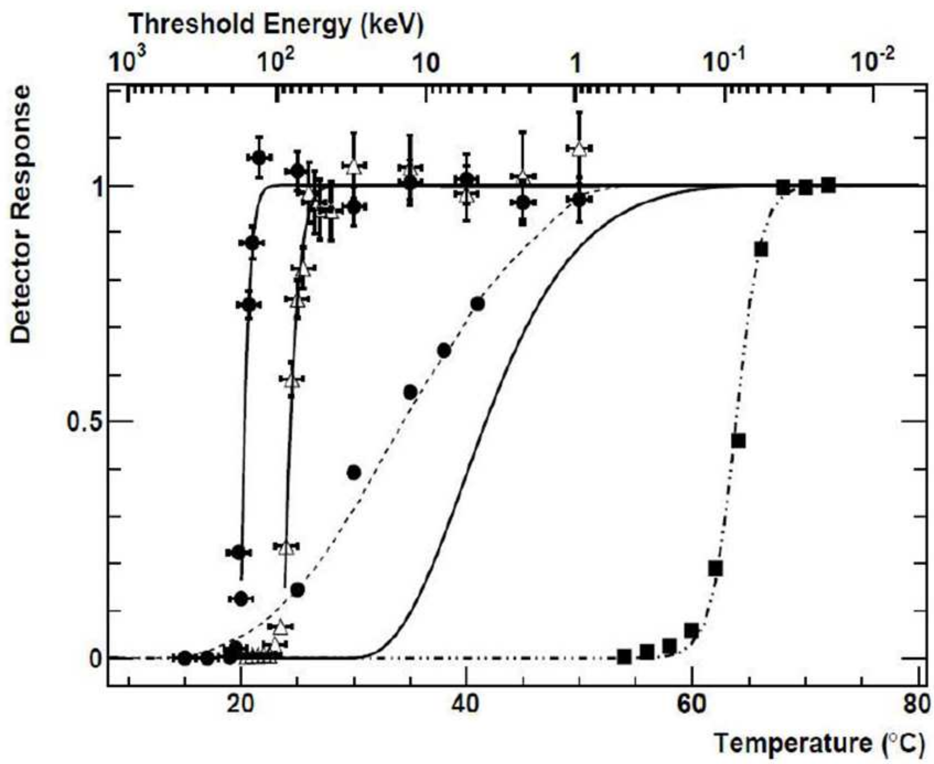

Figure 5.5: Response to different kinds of particles in PICASSO detector. From left to right the responses are due to ^{210}Pb of recoil energy 146 keV from ^{226}Ra decay chain, alpha particles at Bragg peak from ^{241}Am decays, poly-energetic neutrons from AcBe source (dotted), recoiling fluorine modeled assuming the scattering of WIMP of mass 50 GeV/c^2 (continuous line), γ-rays from gamma source, namely, ^{22}Na and for minimum ionizing particles (dot-dashed) respectively. [78]. All responses are normalized to one at full detection efficiency. Temperatures are converted to threshold energies of ^{19}F recoil (upper x-axis)using Equation (5.22).

on the tracks of electrons of energy 5 keV to 500 keV and on the tracks of muons of energy 1 GeV are similar in shape and 50 % of the emitted δ-rays are found to deposit energies smaller than 0.05 keV [16]. So, from Figure 5.5, it is observed that minimum ionizing particles like gamma rays, electrons, muons produce bubble nucleation above 50 °C (less than energy $\approx$ 1 keV) for PICASSO detector.

The dotted curve in Figure 5.5 is for poly-energetic fast neutrons from AcBe source. At the experiment site, neutrons can be produced by muons traversing the detector itself and by (α,n) reactions in the surrounding rock. The fast neutron flux is measured to be $\sim$ 3000 neutrons m^{-2}d^{-1} at the experiment site. The neutron background is reduced by using water shielding of thickness 30.5 cm which acts as a neutron moderator and absorber. From the measurements using ^{3}He counters and the simulation results, it is observed that the fast neutron flux from the surrounding rock is decreased by a factor about 35 [32]. The estimated neutron induced count rate at the experiment site is at the level of 1.1 neutrons per kg of ^{19}F per day for operation at 5 keV threshold energy or at temperature of about 40 °C.

In Figure 5.5 the continuous curve (without any associated data points) represents the expected response curve of ^{19}F recoils assuming scattering of WIMPs of mass 50 GeV/c^2 with ^{19}F nuclei. This curve has been obtained by following procedure.

The observed event rate as a function of WIMP mass (M_χ), spin-dependent cross section ($\sigma_0^{\rm SD}$) and operating temperature (T) can be expressed by [16],

$$R_{\rm obs}(M_\chi, \sigma_0^{\rm SD}, T) = \int_0^\infty P(E_{\rm R}, E_{\rm R,th}(T)) \times \frac{dR(v_{\rm E}, v_{\rm esc} = \infty)}{dE_{\rm R}} dE_{\rm R}, \tag{5.25}$$

where $\frac{dR}{dE_{\rm R}}$ is the WIMP induced recoil energy spectrum of ^{19}F nuclei which can be obtained using Equation (5.13) and the nucleation probability $P(E_{\rm R}, E_{\rm R,th}(T))$ is given by Equation (5.24). The value of $F^2(E_{\rm R})$ in Equation (5.13) is close to 1 for light nucleus like fluorine and for small momentum transfer. At a particular temperature, the detection efficiency of WIMP of mass M_χ can be expressed as [16],

$$\begin{aligned} \epsilon(M_\chi, T) &= \frac{\int_0^\infty P(E_{\rm R}, E_{\rm R,th}(T)) \frac{dR}{dE_{\rm R}}\, dE_{\rm R}}{\int_0^\infty \frac{dR}{dE_{\rm R}}\, dE_{\rm R}} && (5.26) \\ &= \frac{c_2}{c_1} \frac{1}{R_0} \int_0^\infty P(E_{\rm R}, E_{\rm R,th}(T)) \frac{dR}{dE_{\rm R}} dE_{\rm R} && (5.27) \end{aligned}$$

Using Equations (5.25) and (5.27), the observed count rate due to WIMP can be expressed as a function of WIMP mass, WIMP-nucleus cross-section and temperature of detector:

$$R_{\text{obs}}(M_\chi, \sigma_0^{\text{SD}}, T) \quad = \quad \frac{c_1}{c_2} R_0(M_\chi, \sigma_0^{\text{SD}}) \epsilon(M_\chi, T) \tag{5.28}$$

where all the detector properties are included in the rate via the factor $\epsilon(M_\chi, T)$, and the effect of the velocity of the Earth on the WIMP-nucleus interaction rate is included in the factor $(\frac{c_1}{c_2})$. Expected count rate for detectors can be determined by Equation 5.28 as a function of temperature for a fixed interaction cross-section.

Figure 5.5 shows that PICASSO detector is strongly sensitive to alpha particles over the entire range of its WIMP sensitivity, while background from γ-rays can be rejected by choosing proper temperature region. As a result alpha particles remain as the most important background for the PICASSO experiment. The best detector is found to have an average background rate of 20.0 $\pm$ 1.9 (stat.) $\pm$ 1.3 (syst.) cts kg(F)$^{-1}$ d^{-1} [32].

Data Analysis Procedure :

The experiment is run in two run modes : One is WIMP run (without presence of any source) and other is calibration run (in presence of poly-energetic AmBe neutron source of activity 68.71 $\pm$ 0.74 s^{-1}). The WIMP runs are of about 40 hours duration and run at temperature of 30-50 °C, while the time duration of calibration runs are comparatively less and depends on the operating temperature. After each run the detectors are pressurized for 15 hours at a pressure of 6 bar to convert the vapour bubbles back to the superheated liquid droplets to prevent excessive bubble growth which could damage the polymer matrix of the detector.

A typical pulse from piezoelectric sensors is shown in Figure 5.6. Different features of the acoustic signal, like acoustic energy, signal rise time, duration of signal, frequency contents of signals etc. are used to construct various variables to discriminate between the different particle induced nucleation events and also the

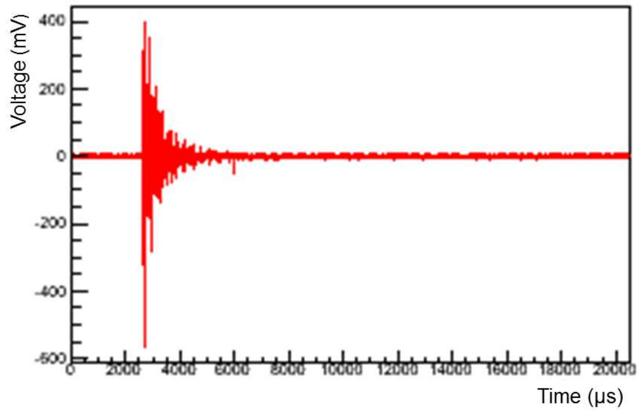

Figure 5.6: Typical signal from piezoelectric transducer.

non-particle induced noise events. PICASSO uses the following three variables, namely, PVAR, FVAR, RVAR, in the data analysis procedure [79, 80, 81]. These variables are discussed below.

- PVAR : The variable PVAR is a measure of the integrated sound intensity or acoustic energy. A low frequency cut is applied at 18 kHz by using Butterworth high pass filter. The algorithm of calculating PVAR variable is described below and graphical representations of the various steps [82] are shown in Figure 5.7:

  (a) Amplitude of the filtered signal is squared (top panel of Figure 5.7) and integrated over the signal duration starting from a fixed pre-trigger time (middle panel of Figure 5.7).

  (b) A straight line is drawn by joining the cumulative sum at pre-trigger time and that at the end point of signal (see middle panel of Figure 5.7). The absolute difference between cumulative sum of integral of amplitude and the straight line are calculated (bottom panel of Figure 5.7).

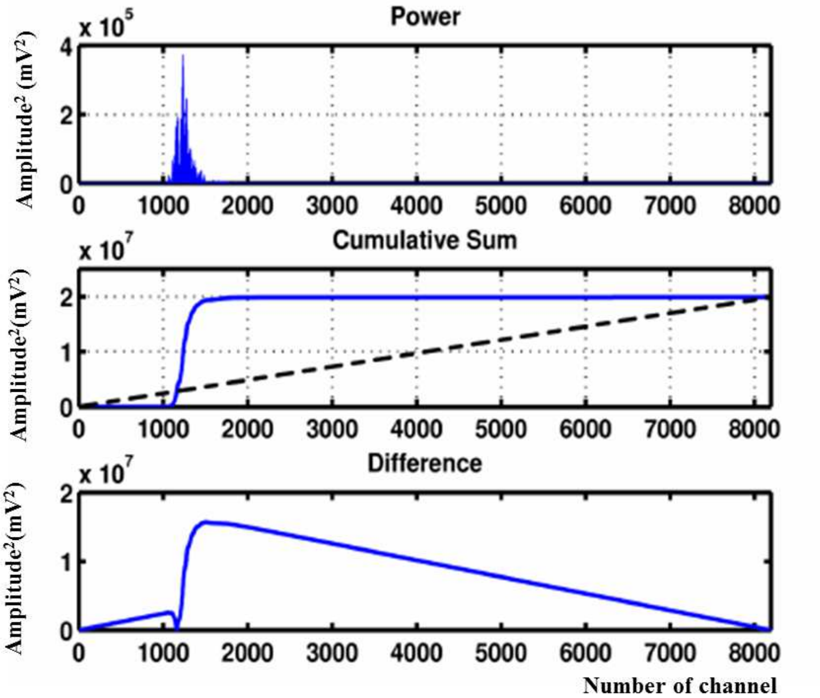

Figure 5.7: Graphical representation of the various steps in the construction of the variable PVAR [82]. (see text for details)

(c) Integral is taken over the obtained absolute difference and logarithm is taken over the resulting values.

(d) To reduce the solid angle effects an average is taken over the relevant number of active transducers.

Mathematically,

$$\mathrm{PVAR} = \frac{\sum_{i=0}^{N_{\mathrm{piezo}}-1} \log_{10}\left[\sum_{j=j_0}^{j_{\mathrm{N}}}\left|\sum_{j=j_0}^{j} A_{ij}^2 - \frac{A_{ij_0}^2 - \sum_{j=j_0}^{j_{\mathrm{N}}} A_{ij}^2}{j_0 - j_N} j\right|\right]}{N_{\mathrm{piezo}}}, \quad (5.29)$$

where A_{ij} is amplitude of the pulse corresponding to j^{th} time bin and i^{th} piezo. N_{piezo} and j_{N} are total number of active piezo and time bin, respectively.

- FVAR : This variable is constructed using the power in the frequency region associated with an acoustic signal. Here, the majority of the signal power is found in the range between 20-70 kHz. Steps for calculating FVAR is described below:

  (a) To obtain the frequency components associated with the signal the Fast Fourier Transforms (FFT) of signals is constructed. In Figure 5.8 [81] waveform and the FFT of particle and non-particle induced events are shown for illustration.

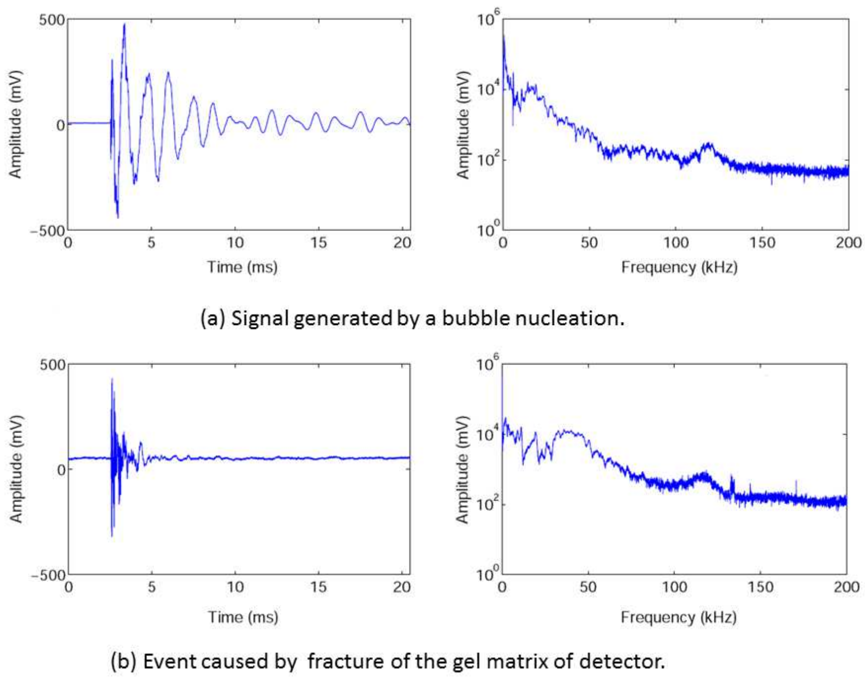

Figure 5.8: Waveform and FFT of particle and non-particle induced events [81].

  (b) Two frequency regions are chosen, say, region-I spans the range 20-30 kHz, while region-II covers the range 45-55 kHz. These frequency windows are chosen such that good separation between noise to particle induced events is obtained.

  (c) Mean of the amplitudes is calculated separately for two frequency regions and the ratio of the mean amplitude of region-I to that of region-II is constructed.

(d) Logarithm of the ratio from step (c) is then taken.

(e) Finally an average is taken over all active transducers.

Mathematically,

$$\mathrm{FVAR} = \frac{\sum_{i=0}^{N_{\text{piezo}}-1} \log_{10}\left[\frac{\frac{1}{N_{\mathrm{I}}}\sum_{j=f_1}^{f_2} A_{ij}^{\text{RegionI}}}{\frac{1}{N_{\mathrm{II}}}\sum_{j=f_3}^{f_4} A_{ij}^{\text{RegionII}}}\right]}{N_{\text{piezo}}}, \tag{5.30}$$

where A_{ij} is the amplitude of the signal corresponding to j^{th} frequency bin and i^{th} piezo. The quantities $N_{\mathrm{I,II}}$ are the number of total frequency bins in region I and region II, respectively, and f_1, f_2 are the lowest and highest bin numbers corresponding to the frequency of region-I, while f_3, f_4 are the lowest and highest bin numbers corresponding to the frequency region-II.

- RVAR : This parameter represents the steepness of the growth of the signals and gives the information of the acoustic energy content within the first 25 μs at the beginning of a signal. Algorithm used to calculate RVAR can be divided into two parts:

  (a) Finding the starting point of an event, say, t_0.

  (b) Construction of RVAR.

  In ideal case, it is expected that there is no electronic noise over time and generation of a pulse due to nucleation gives an accurate starting time of the event. But in actual practice, the presence of electronic noise makes it difficult to find the accurate value of t_0. Following steps are performed to obtain t_0:

(i) The third power of the amplitude of a signal is calculated in every time bin in order to accentuate the differences between the amplitudes in successive time bin. The reason behind taking third power is also to keep the positive and negative values of the amplitudes of the signal.

(ii) The resulting (amplitude)^3 values are normalized using the maximum value of (amplitude)^3.

(iii) Two secondary signals are built : first by taking average over a time interval of 5 μs and the second with a time interval of 40 μs (see Figure 5.9 [81]).

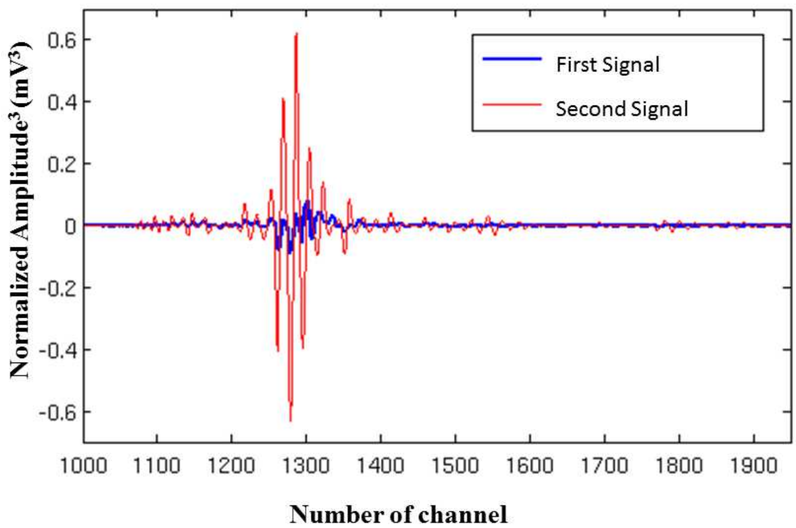

Figure 5.9: Waveform of the two signals generated for determining the starting point of a signal, t_0 [81].

(iv) The absolute difference between these two signals is calculated, which allows the demarcation of two different time zones : one, in which the absolute difference being roughly constant over time and corresponds to the electronic noise before the arrival of a true signal, and the other showing a sudden increase due to arrival of the true signal.

(v) Next, the maximum value of the absolute difference within first 375 μs of the signal is calculated.

(vi) Finally, t_0 is defined such that the value of the absolute difference is 10 times smaller than the maximum value calculated in the previous step.

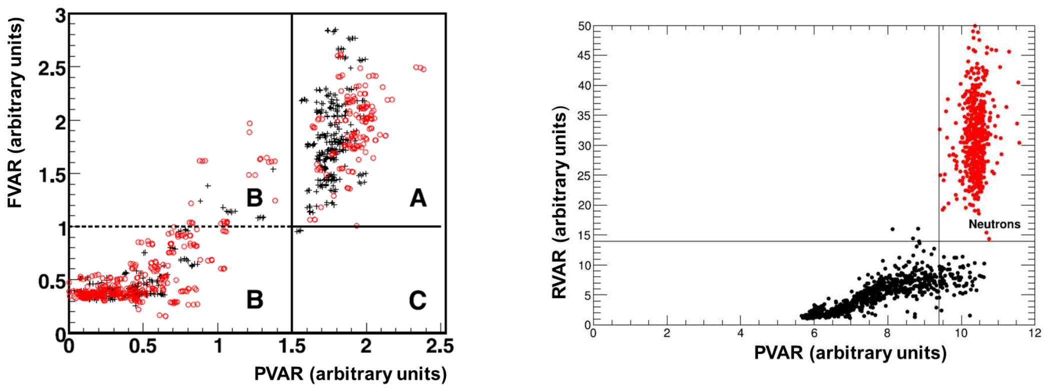

(a) (b)

Figure 5.10: (a) FVAR vs PVAR scatter plot with data from n-calibration (black crosses) and WIMP runs (red circles) for detector 71. Neutron induced events using AmBe source are located in region A. Alpha induced events in WIMP runs are also located in region A. Electronic noise and background acoustic noise like mine blasts are in region B. Noise due to fracture of the polymer would be located in region C, but has not occurred in this case [62]. (b) The scatter plot of RVAR vs. PVAR allows the discrimination between particle induced events from the background events. Neutron induced events are in the upper right rectangle while the background events have low values of RVAR [32].

Once t_0 of a signal is obtained, the variable RVAR is calculated by taking the standard deviation of the amplitudes in the first 25 μs from the time t_0 of the original signal and then taking logarithm and an average are taken over all active transducers.

Mathematically,

$$\mathrm{RVAR} = \frac{\sum_{i=0}^{N_{\mathrm{piezo}}-1} \log_{10}\left[\frac{1}{N}\sum_{j=t_0}^{t_0+N}(A_{ij}-\bar{A}_j)^2\right]^{1/2}}{N_{\mathrm{piezo}}}, \tag{5.31}$$

where $\bar{A}_j = \frac{1}{N}\sum_{j=t_0}^{t_0+N} A_{ij}$ is mean of the amplitude within first 25 μs of a signal and N is the total number of time bins within the first 25 μs of the signal.

Some typical distributions of the three variables, PVAR, FVAR, RVAR, can be seen in Chapter 8. Among these three variables, PVAR is the prime variable to discriminate the non-particle induced events from the particle induced nucleation events. The variable FVAR is effective in rejection of the noise events caused by fracture in polymer matrix, mine blast. At higher temperature, mainly above 40 °C a special type of events called "mystery events" are observed which have slow rise time but with an acoustic energy and frequency content that are comparable to the actual bubble nucleation events. Most probably these events are caused by successive secondary nucleation events near the primary one. RVAR variable is efficient in eliminating mystery events. Scatter plots of FVAR vs. PVAR and RVAR vs. PVAR is shown in Figure 5.10 [32, 62], which show that the different types of events can be well discriminated using these three variables.

Finally to derive exclusion plots (for null results) in the WIMP mass vs. WIMP-nucleus cross section further analysis is performed as follows : First, a run having at least six active transducers and with duration greater than 15 hours for WIMP run and 1 hour for calibration run is chosen as a "good" run. A list of good runs is then made for each of the detectors used in the analysis. If two successive events with a time difference of less than 3 sec ($<$ 0.1 sec for calibration run) occur, then the second event is rejected. In case of low background detectors, the probability of successive events within 3 seconds are very negligible unless the events are re-triggers of the same events or the events physically induced in detector by primary

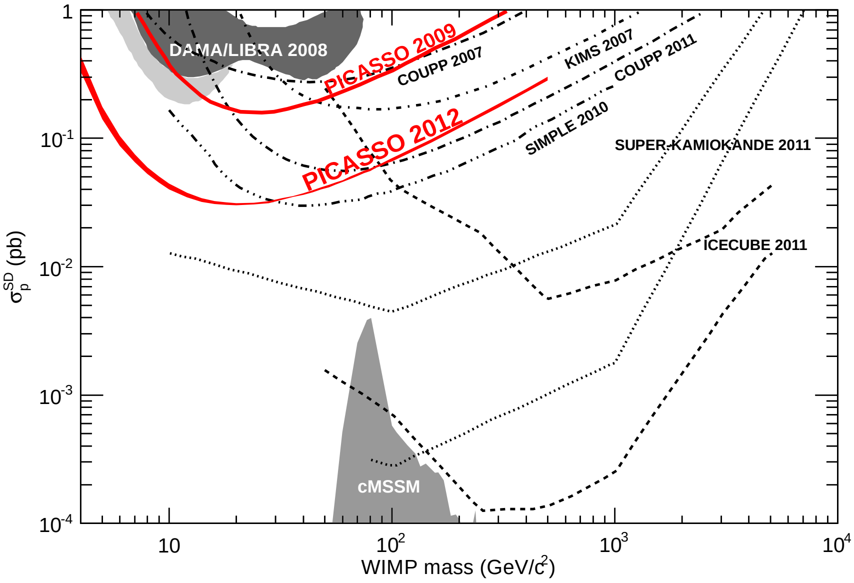

Figure 5.11: Upper limits on cross-section at 90 % C.L. from PICASSO experiment on spin dependent sector are shown in red line [32].

expansion [32]. After that, the particle induced events are selected using a cutoff value of PVAR variable so that 95 % of the particle induced nucleation events are accepted. It is to be noted that for calibration run only first 200 neutron induced events are selected to reduce the effect of decrement of amplitude due to the presence of a large number of bubbles. We shall discuss about this effect later in Chapter 8. In the next step, cutoff values of the variables RVAR and FVAR are applied respectively in such a way that for each case 95 % of the particle induced nucleation events are accepted. The response of alpha particles increases more sharply with increasing temperature than that expected for WIMPs and neutrons. In the energy range of interest, this effect allows us to have two different response curves for alpha and WIMPs. A combined fit of alpha and WIMP response to the data allows one to obtain the upper limit on cross-section for a particular mass of WIMP. For a fixed WIMP mass (M_χ), the WIMP-nucleus cross-section and a scale factor related to alpha response curve are varied to obtain the upper bound

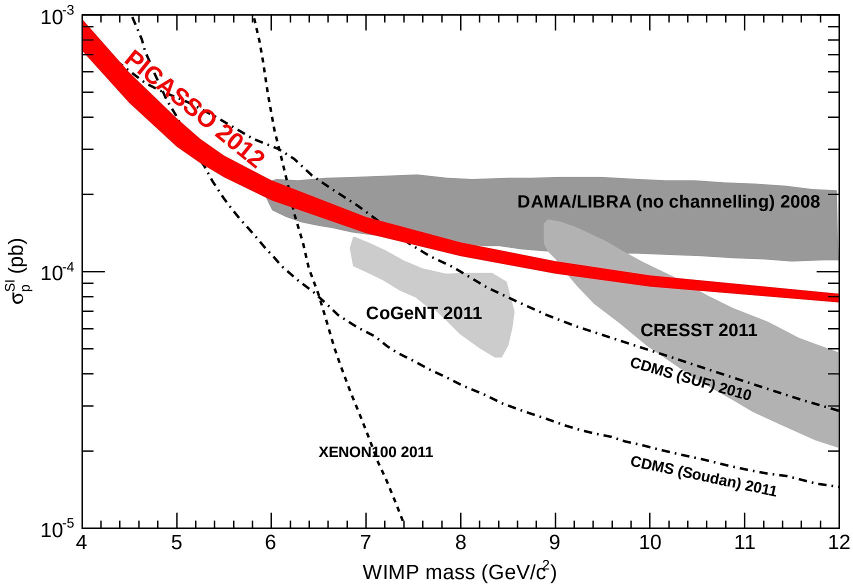

Figure 5.12: Upper limits on cross-section at 90 % C.L. from PICASSO experiment on spin independent sector are shown in red line [32].

of the WIMP-nucleus cross-section. In this analysis value of the parameter α is adopted as 5 and is varied within the interval $2.5 < \alpha < 7.5$.

The results obtained from the analysis of the PICASSO data from a total of 264 WIMP runs for 10 detectors are shown in Figures 5.11 and 5.12 [32]. In the spin-dependent sector (Figure 5.11), the upper limit on the WIMP-proton cross section for WIMP mass of $\sim$ 20 GeV/c^2 is 0.032 pb (90 % C.L.), while in the spin independent sector (Figure 5.12) this limit is 1.41×10^{-4} pb (90 % C.L.) for WIMP mass of $\sim$ 7 GeV/c^2 [32].

The PICASSO experiment ran until the end of 2013. As it is very important to reduce the background due to recoil induced events produced by neutrons, the thickness of the water shielding has been increased to 50 cm from 30.5 cm. As a result the external neutron flux is reduced by a factor of 400. At present ongoing works are being performed to improve the resolution of the discrimination between alpha particle and neutron induced bubble nucleation events. These works are focused on corrections for time of occurrence of the events during run, localization of the events, correction on distance and angle of events from piezoelectric transducers, choice of proper fiducial volume, wavelet analysis variables, double speed electronics, gain optimization of electronics, etc.

In next three Chapters, we discuss some studies related to understand the observed two threshold temperatures for two different alpha sources, role of droplet radius, low frequency components of acoustic signals in discrimination of alpha and neutron induced events and implementation of a correction method to obtain a better resolution of PVAR variable which could produce a better discrimination between alpha-neutron induced events.

Chapter 6

Simulation study of alpha response of the PICASSO detector

6.1 Introduction

As discussed in Section 5.4, alpha particles, gamma rays and neutrons are known to be responsible in the background nucleation events in the PICASSO DM search experiment. The cosmic ray induced backgrounds can be reduced by performing the experiment at the underground location which helps to reduce the flux of muons. The neutrons produced by the (α,n) reaction the surrounding rocks at the SNOLAB site are reduced by using shielding of ultra pure water which acts as neutron absorber and moderator. The gamma ray induced background nucleation events can be rejected by a proper choice of operating temperature of the experiment. But alpha particles remain as contamination in the polymer matrix or sensitive liquid of the detector and it is clear from the response curve of PICASSO detector shown in Section 5.4 that alpha particles could produce bubble nucleation over the whole temperature range in which WIMPs are also sensitive. Thus, it is not possible to reject the nucleation events due to the alpha particles by choosing a temperature range or by using any shielding outside the PICASSO detector. Instead, to reduce such background events, it is essential to purify the polymer matrix and active liquid used in the fabrication of the detector.

The normalized count rate per unit active mass of ^{19}F from WIMP runs from more than one PICASSO detectors was observed to remain flat at the temperature 25 °C to 48 °C, which was identical to the response of detector spiked with alpha source, namely, ^{226}Ra. Unlike the expected response curve for recoiling fluorine due to WIMP interaction, the normalized count rate in the case of the α-particles is observed to increase sharply with temperature near the threshold temperature. From these observations it can be concluded that the most dominant intrinsic sources of background for the PICASSO detector are the alpha particles.

To reduce the alpha particle induced background nucleation events, it is important to understand the effect of alpha contamination in polymer matrix and active liquid on the response of PICASSO detector. For this purpose, the detectors were spiked with alpha emitters outside and inside the droplet using two alpha sources, ^{241}Am and ^{226}Ra, respectively [61]. It was observed that the response of alpha particles for these two cases showed two different threshold temperatures. In this Chapter, we study the response of PICASSO detectors to alpha particles for the above mentioned experiments using GEANT3.21 simulation toolkit [53] to understand the reason behind the two different threshold temperatures. The aim of this study is to investigate whether the different energies of alpha particles during these experiments are responsible for the observed two different threshold temperatures.

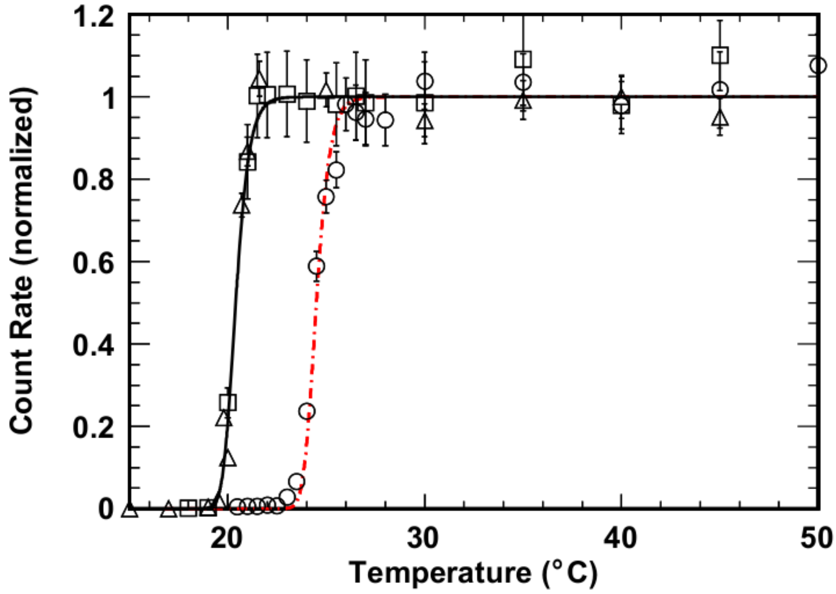

Figure 6.1: Experimental result from Ref. [61]. The response of detector Urs obtained after spiking the polymer matrix by alpha source, namely, ^{241}Am is shown by open circles and that of detector 74 spiked with α-sources ^{226}Ra is indicated by squares and triangles. The latter response curve has lower threshold temperature compared to the former. In detector 74, alpha particles were present in polymer matrix as well as in the liquid droplets.

6.2 Present Work

The details of the experiment for which the simulation is carried out is described in Ref. [61]. A brief description of the experiment is given below. The experiments were performed to study the α response of two PICASSO detectors, namely detector Urs and detector 74, which were particularly prepared for this purpose. The detector Urs was spiked with a ^{241}AmCl solution. The ^{241}Am with an activity of 6.4 Bq was present only in the polymer matrix. The active mass of liquid C_4F_{10} in that detector was (17.8 $\pm$ 2) gm which corresponds to volume loading fraction of (0.84 $\pm$ 0.08) %. The other detector, namely, detector 74, was spiked with 10 Bq of ^{226}Ra. The active mass was (26 $\pm$ 3) gm which corresponds to volume loading fraction of (1.2 $\pm$ 0.1) %. In this case α-particles were present both in the polymer matrix and the C_4F_{10} liquid droplets as ^{226}Ra slowly diffuses to the whole detector volume from the point of injection within a few days. Both detectors having a volume of 1.5 litre were smaller versions of the standard PICASSO detector modules. Details of PICASSO detector modules are discussed in Section 5.4. The droplet size distribution peaks at a diameter of around 200 μm.

Figure 6.1 shows that the normalized count rate of ^{241}Am-spiked detectors (circles) has a threshold at 22 °C while for ^{226}Ra (squares and triangles) the threshold temperature is shifted downward by about 4 °C. This shift in the threshold temperature was suspected to be due to ^{210}Pb nuclei generated in the ^{226}Ra-decay chain, giving nuclear recoils inside the droplets (E_R = 146 keV). The simulation studies presented here verify that this is indeed the case. We also derive the nucleation parameter (k) [36] for α-particles in the case of C_4F_{10} liquid used in the PICASSO experiment.

6.2.1 Calculation of range and stopping power of α-particles in C_4F_{10} by GEANT3.21

We first study the range and stopping power of 5.6 MeV α-particles in C_4F_{10} (density 1.437 gm/cc [83]) using GEANT3.21 Ref. [53]. The simulation has two parts : the geometry of the detector and tracking of particles. In the geometry part, first a cylinder of C_4F_{10} of diameter 15 mm and height 20 cm is constructed. In the simulation, the energy deposition can be obtained at each 5 μm path interval. To obtain energy deposition at 5 μm path interval, the default values of some parameters in GEANT3.21 have been changed. In this simulation, STMIN = 5 μm, DEEMAX = 0.001 are taken and the parameters representing kinetic energy cuts, such as CUTELE, CUTGUM, CUTNEU, CUTMUO and CUTHAD, are all kept at 10 keV for the C_4F_{10} medium. The parameter STMIN controls the minimum step length of the particles in the simulation, while DEEMAX is the maximum fractional energy loss in one step [53]. The α-particle is incident at the position (x, y, z) = (0.0, 0.0, -10.0) cm with momentum (p_x, p_y, p_z) = (0.0, 0.0, 0.2044) GeV/c where the center of the coordinate system is at the center of the cylinder.

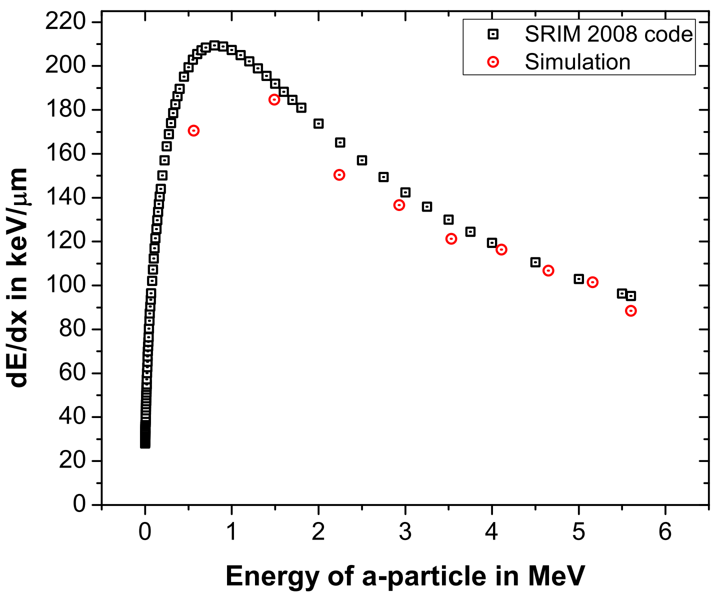

Figure 6.2: dE/dx as a function of energy of alpha particle within C_4F_{10} liquid obtained from simulation using GEANT3.21 (red, circle) and SRIM code (black, square).

The $\frac{dE}{dx}$ as a function of energy of α-particle obtained from one particular run of GEANT3.21 is shown in Figure 6.2 for illustration. For comparison we also show the mean value of $\frac{dE}{dx}$ obtained from SRIM [50] in Figure 6.2. The discrepancy of $\frac{dE}{dx}$ obtained from SRIM and GEANT near the peak of the $\frac{dE}{dx}$ curve (where $\frac{dE}{dx}$ varies sharply) is due to our calculational limitation in choosing sufficiently small values of the step length in GEANT.

6.2.2 Simulation for ^{241}AmCl-spiked detector

^{241}Am decays to ^{237}Np by emitting an α-particle of energy 5.48 MeV (85.2%) and 5.44 MeV (12.8%): $^{241}\mathrm{Am} \rightarrow\ ^{237}\mathrm{Np} + \alpha + 5.64$ MeV. Instead of taking the accurate alpha energy, in our simulation we used the Q-value of the disintegration as the energy of the emitted α-particle. This choice does not affect the result of our simulation because the Bragg peak of α-particle, which plays important role in bubble nucleation, occurs below 2 MeV energy. Contribution to bubble nucleation in C_4F_{10} due to nuclear recoil caused by ^{237}Np is very small due to its short range —it essentially stays in the polymer. So, in the simulation, nucleation due to ^{237}Np has not been considered. In this situation, nucleation is primarily due to α-particles for which the nucleation parameter (k) is estimated from simulation.

Geometry of detector and tracking of particle

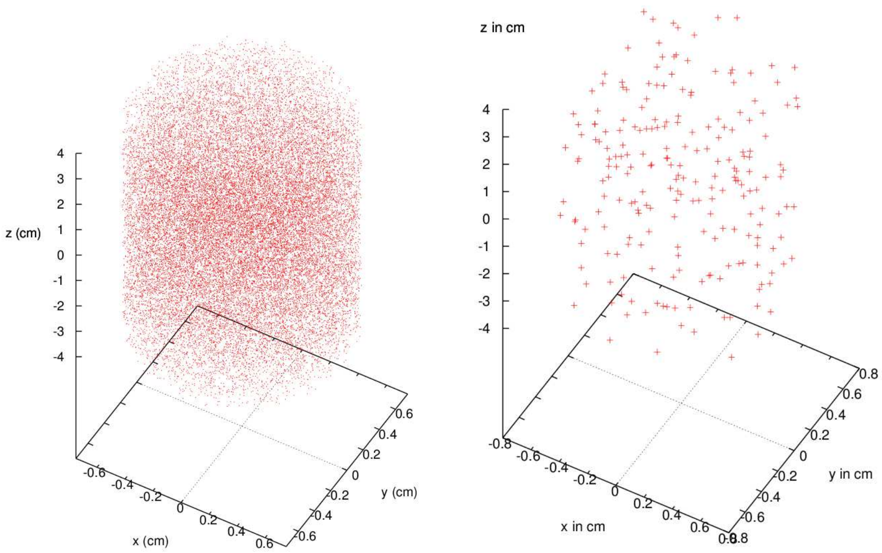

Figure 6.3: Distribution of the centers of C_4F_{10} droplets within ^{241}Am-spiked detector (left), and distribution of the initial positions of the α-particles within ^{241}AmCl-spiked detector (right).

The first part of the simulation is creating the geometry of the detector. In the geometry part of the simulation, first a holding matrix of CsCl of density 1.6 gm/cc is created. Next a small prototype detector consisting of droplets of C_4F_{10} dispersed in a cylinder of CsCl having diameter 15 mm and height (h_{cyln}) 80 mm is created. The variation of the density of C_4F_{10} with temperature is considered according to Ref. [83]. Volume loading fraction of C_4F_{10} has been taken to be 0.84 %. The loading fraction is used to calculate the number of droplet distributed within the detector using the following equation :

$$N_{\text{droplet}} \times \frac{4}{3}\pi r^3_{\text{droplet}} = \text{Volume loading fraction} \times \pi r^2_{\text{cyln}} h_{\text{cyln}}, \tag{6.1}$$

where, N_{droplet} = number of droplets, r_{droplet} = radius of each droplet, r_{cyln} = radius of the detector and h_{cyln} = height of detector. A total of 28350 non-overlapping droplets of C_4F_{10} are distributed randomly and uniformly within the CsCl matrix, and the distribution of the centers of the droplets, shown in Figure 6.3 (left), has been produced by using random number generator SRAND code [54]. The diameter of each droplet is taken as 200 μm. In the simulation, C_4F_{10} is set as the sensitive liquid to collect the information of hit points by α-particles from only this part of the detector.

The next part of the simulation is the tracking of the particle. Simulation has been done for an experiment time duration of 1 h. In the simulation, the detector volume is 14.137 cc. Hence the activity of ^{241}Am is about 0.06 Bq. As a result, total number of decays in 1 h is about 216 within the detector. Thus, a total of 216 α-particles each with energy 5.64 MeV are distributed randomly and uniformly within the polymer as shown in Figure 6.3 (right). To keep the α-particles only within the polymer, the distance between an α-particle's initial position and any droplet center is kept greater than the radius of the droplet (here, 100 μm). The three components of each α-particle's momentum have been distributed randomly. Again, SRAND random number generator is used for creation of random distribution of vertices and momenta. The simulation has been done for different temperatures from 14 °C to 46 °C. Temperature variation of the density of C_4F_{10} is taken into consideration in the simulation.

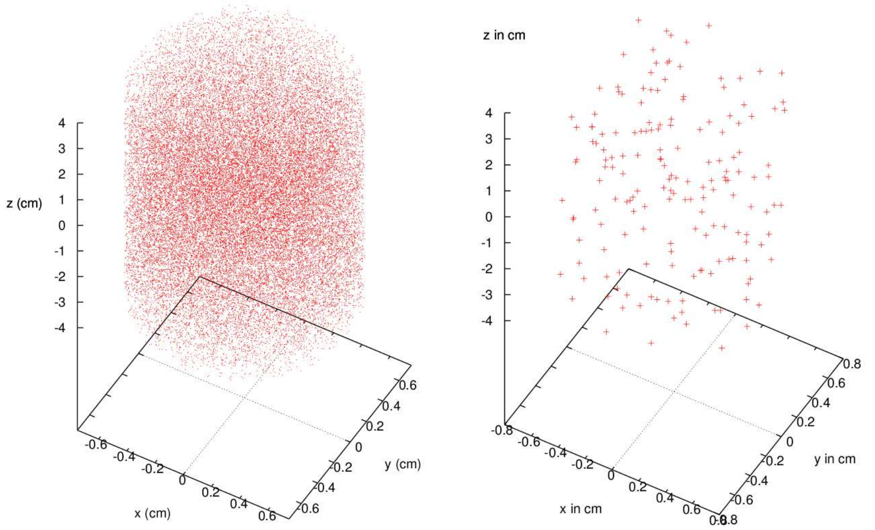

Figure 6.4: Distribution of the centers of C_4F_{10} droplets within ^{226}Ra-spiked detector (left), and the distribution of initial position of the α-particles emitted from ^{226}RaCl-spiked detector (right).

6.2.3 Simulation for ^{226}RaCl-spiked detector

The decay chain of ^{226}Ra can be written as $^{226}\text{Ra} \rightarrow {}^{222}\text{Rn} \rightarrow {}^{218}\text{Po} \rightarrow {}^{214}\text{Pb} \rightarrow {}^{214}\text{Bi} \rightarrow {}^{214}\text{Po} \rightarrow {}^{210}\text{Pb}$. The ^{226}Ra ($T_{1/2}$ = 1602 y) decays into ^{222}Rn ($T_{1/2}$ = 3.8 d) by emitting two α-particles of energies 4.602 MeV and 4.785 MeV. The rest of the chain involves the emission of three α-particles of energies 5.49 MeV, 6.0 MeV and 7.69 MeV, respectively and two β-particles. The $\frac{dE}{dx}$ values of α-particles from above decay chain are calculated by GEANT3.21 and the normalized count rate is obtained below using the nucleation parameter obtained from the previous simulation for ^{241}Am.

Geometry of detector and tracking of particle

In this simulation, the volume loading fraction of C_4F_{10} has been taken to be 1.0 %. Correspondingly, the number of droplets (N_{droplet}) is 33750 using Equation (6.1). All droplets are again randomly and uniformly distributed as shown in Figure 6.4 (left). Distribution of the initial positions of the α-particles is shown in Figure 6.4 (right). The initial positions are created again using SRAND random number generator, outside GEANT. Other characteristics of the simulation are as follows :

(a) The activity of ^{226}Ra is about 0.09 Bq. As simulation has been performed for an experiment time duration of 1/2 h, total number of decay in 1/2 h is about 170. As a result, there are 170 initial positions for α-particles. As mentioned above, there are three relevant α-particles of energy 5.49 MeV, 6.0 MeV and 7.69 MeV at each vertex. Thus the total number of α-particles in the simulation is $(3 \times 170) = 510$.

(b) As ^{226}Ra diffuses in the whole detector, 510 α-particles are distributed uniformly and randomly within the droplets and the polymer matrix.

6.3 Results and discussion

The GEANT simulation provides the $\frac{dE}{dx}$ of α-particles within the droplets. Sometimes there are more than one hit points within a droplet. The energy deposition by α-particle is recorded at every 5 μm distance. From those values, only the highest value of $\frac{dE}{dx}$ is considered. If the value of $\frac{dE}{dx}$ is greater than $\frac{W}{kr_c}$, it is taken as a nucleation event. Here $W = \frac{16\pi\sigma^3(T)}{3(p_v - p_0)^2}$ is the threshold energy and r_c is the critical radius at a given temperature and pressure. The quantity k is the nucleation parameter as described in Section 2.2. Events due to more than one nucleation from same droplet are rejected since in reality a droplet disappears after nucleation event. The count is normalized by the total experimental duration and active mass. For calculating the normalized rate, the density of C_4F_{10} at 30 °C (1.478 gm/cc) is taken.

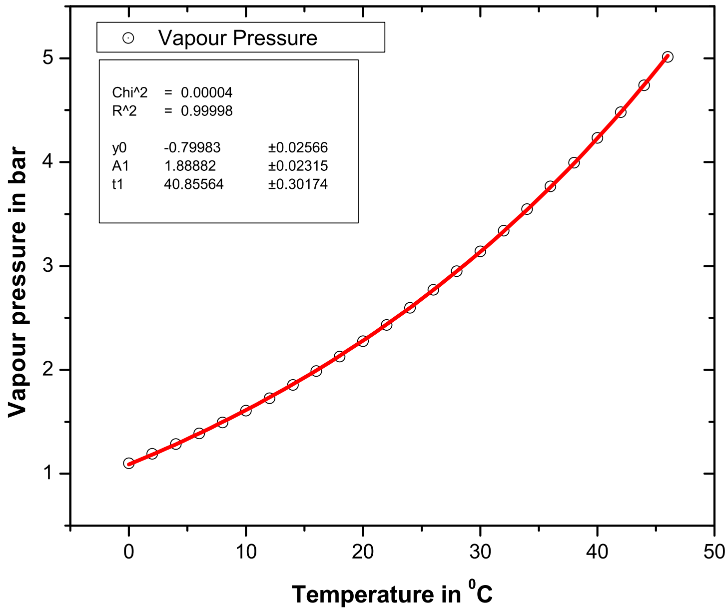

Figure 6.5: Variation of vapour pressure with temperature for C_4F_{10} liquid obtained from Ref. [83] is fitted by the exponential growth function (Equation 6.2).

The surface tension at liquid-vapour interface is obtained from the following relation: $\sigma(T) = A(1 - T/T_c)^n$, where for C_4F_{10} $A = 66.981$, $n = 1.2175$, $T_c = 386.35$ K is the critical temperature and $\sigma(T)$ is in dyne/cm [84]. The values of p_v at various temperatures are read off from the following fitted functional form shown in Figure 6.5, namely,

$$y = y_0 + A_1 \exp(x/t_1), \tag{6.2}$$

where y is p_v and x is T and the fitted parameters are $y_0 = -0.7998 \pm 0.02566$, $A_1 = 1.88882 \pm 0.02315$, $t_1 = 40.85564 \pm 0.30174$.

6.3.1 For ^{241}AmCl-spiked detector

From simulation we have obtained that among the present 216 alpha particles within the polymer matrix of the detector, only 3 of them are able to hit a droplet. No multiple hits to a same droplet are seen. In this case, the active mass of detector of volume 14.137 cc is $(14.137 \times 0.0084 \times 1.478) \approx 0.1755$ gm or 175.5 mg, where density of C_4F_{10} at 30 °C is taken to be 1.478 gm/cc. Consequently, the count rate obtained in the plateau region is found to be about 17.09 $h^{-1}gm^{-1}$. Varying the value of k, the response has been fitted with the experimental result.

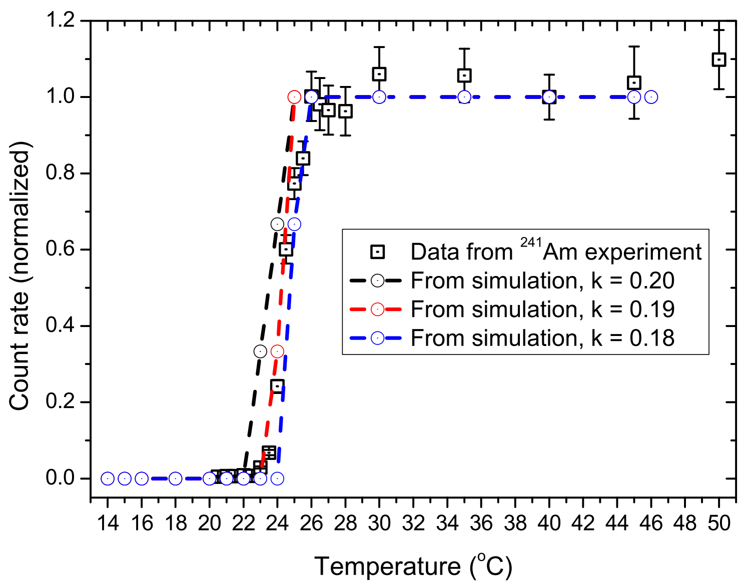

Figure 6.6: Result obtained from simulation of ^{241}Am spiked detector for nucleation parameters (k), namely, 0.20, 0.19 and 0.18.

To find the value of the nucleation parameter k, the experimentally obtained normalized count rates ($N_{\text{expt},i}$) are compared with those obtained from simulation ($N_{\text{sim},i}$) at different temperatures in the temperature region (21 °- 45 °) C. The deviation between the experimental and simulation results is calculated for the mentioned temperature range by the equation,

$$\chi^2 = \sum_i \left[\frac{1}{\sigma_i^2} \left(N_{\mathrm{expt},i} - N_{\mathrm{sim},i}(k) \right)^2 \right], \tag{6.3}$$

where σ_i represents uncertainty in $N_{\mathrm{expt},i}$ and i represents temperature. The count rates obtained form the simulation as a function of temperature for three values of the nucleation parameters (k), namely, 0.20, 0.19 and 0.18, are shown in Figure 6.6. The simulation results that give best fit to the experimental data correspond to the value of $k = 0.19$, which we take to be the approximate value of the nucleation parameter for α-particles of energy 5.64 MeV in C_4F_{10} liquid.

6.3.2 For ^{226}RaCl-spiked detector

From simulation of Ra-spiked detector, 16 hit points are obtained. But every hit does not result in a nucleation event. In the plateau region of the α response curve, nucleation condition is satisfied by all 16 hits, but this includes 8 cases of double hits to a same droplet. So, actual count is found to be equal to (16 - 8) = 8. Consequently, at the plateau the actual count rate is 76.58 $h^{-1}gm^{-1}$, where active mass is 208.9 mg. Figure 6.7 shows the normalized count rates obtained from the simulation along with the experimental data points. The simulation points are joined by a red dotted line. The simulation results for ^{226}Ra match reasonably well with the experimental results from ^{241}Am experiment for the value of $k \sim 0.19$ found for the case of α-particles from ^{241}Am decay discussed in Subsection 6.3.1. Thus, it can be concluded that the alpha response curve for PICASSO detector does not depend on the energy of α-particles.

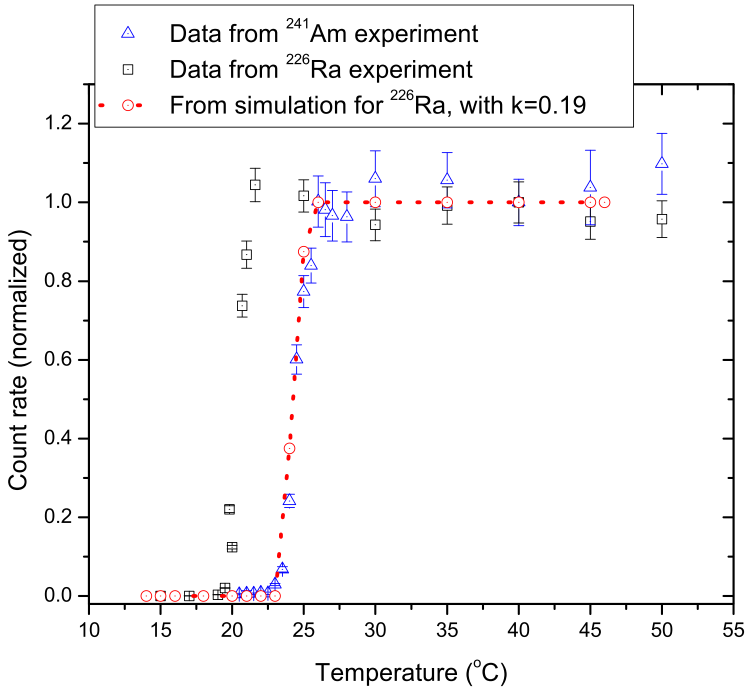

Figure 6.7: Result obtained from simulation of ^{226}Ra spiked detector.

6.3.3 LET of Pb in C_4F_{10}

In the simulation described in the previous subsection, we did not consider the effect of nuclear recoils in C_4F_{10} due to ^{210}Pb coming from the decay chain of ^{226}Ra. In this subsection, we consider this effect and show that the observed shift of the threshold temperature to a lower value in the case of α-particle from ^{226}Ra can be explained due to recoils caused by ^{210}Pb from ^{226}Ra decay chain. We have calculated the LET, $(\frac{dE}{dx})$, using SRIM 2008 code [50]. Actually, instead of ^{210}Pb, another isotope, ^{208}Pb, is taken, as only this is available in SRIM 2008. This calculation is done for two different temperatures by changing the density of C_4F_{10}. The density of C_4F_{10} is taken as 1.478 gm/cc and 1.5195 gm/cc for temperatures 30 °C and 19 °C, respectively. The dE/dx of 146 keV ^{208}Pb in C_4F_{10} for these two cases are 238.53 eV/Å (2385.3 keV/μm) and 245.3 eV/Å (2453 keV/μm), respectively, and the range of ^{208}Pb in that same liquid is 853 Å and 830 Å, respectively. Experimentally, it is observed (Figure 6.1) that for ^{226}Ra nucleation starts at 19 °C. From our calculation, $\frac{W}{r_c}$ at 19 °C is 61.94 keV/μm. So, nucleation parameter for ^{208}Pb in C_4F_{10} is (61.94/2453) = 0.025 which is less than that for α-particles ($\sim$ 0.19). Thus, nucleation due to ^{210}Pb (or actually ^{208}Pb) from ^{226}Ra decay chain is more probable than that due to α-particles from ^{226}Ra, which explains the shift of the experimental threshold temperature in the case of ^{226}Ra to a lower temperature as compared to the results from simulation which does not consider the effect of ^{210}Pb (from ^{226}Ra) but rather considers only the α-particles (from ^{226}Ra).

6.4 Conclusions

We have studied the response of the PICASSO detector to alpha particles from two sources, namely, ^{241}Am and ^{226}Ra to understand the reason behind a lower threshold temperature obtained for ^{226}Ra than that for ^{241}Am, by simulating the energy losses (LET) of alpha particles during their passage through the detector. The nucleation parameter, k, for alpha particle within C_4F_{10} liquid has been determined by comparing the simulation result with that from experiment performed with detector having ^{241}Am spiked polymer matrix. Because of its small range ^{237}Np stays in polymer and does not give contribution in experimentally obtained count rate. In the case of ^{226}Ra spiked detector alpha particles of energies 5.49 MeV, 6.0 MeV and 7.69 MeV are simulated both inside and outside the droplets because in actual experiment radon diffuses throughout the whole detector. The response of detector to alpha particle obtained from simulation for ^{226}Ra spiked detector is similar to that obtained for ^{241}Am spiked detector and in both cases, the simulation results are reasonably well matched to the experimentally obtained response of ^{241}Am spiked detector, for a value of the nucleation parameter $k \sim$

0.19. This result implies that the energy range of alpha particles considered here, is not responsible for the shift of the threshold temperature to lower temperature. Unlike ^{241}Am spiked detector, in case of ^{226}Ra spiked detector various recoiling nuclei from the decay chain of ^{226}Ra are present inside the droplet and the calculation of LET shows that ^{208}Pb of energy 146 keV in particular has a higher value of LET compared to that of α-particles, which could trigger nucleation events at a lower threshold temperature in case of ^{226}Ra spiked detector.

Chapter 7

Study of the role of droplet size distribution in alpha-neutron discrimination in SDDs

7.1 Introduction

As discussed in Chapter 6, the main component of the particle-induced intrinsic background for the PICASSO experiment is the one due to α-particles, which can be present in the polymer matrix or in the sensitive liquid. Though the shapes of WIMP and alpha particle response curves differ from each other, it is rather difficult to discriminate between alpha and WIMP induced events on an event by event basis. On the other hand neutrons and WIMPs both produce nuclear recoils during passing through detector, and in both cases it is the recoiling nucleus that triggers the bubble nucleation event. Hence neutrons and WIMPs have similar response curves (see Figure 5.5 [32]). The neutron background can be removed only by appropriate shielding and then separately measuring the residual neutron background in the region around the detector. Therefore important information about discrimination between alpha and WIMP induced events can be obtained from studies of alpha-neutron discrimination.

In the present phase of PICASSO experiment, the detector contains C_4F_{10} liquid droplets with size distribution peaking at radius of about 100 μm. In its earlier phase, the PICASSO detectors were fabricated with droplets with size distribution peaking at a radius of 5 μm. In PICASSO experiment, piezoelectric transducers are used to acquire the high frequency components of the acoustic pulse generated during bubble nucleation. Using the present phase of PICASSO detector, it is observed that the acoustic signals generated by alpha particle induced bubble nucleations have amplitude that are roughly a factor four more higher than those due to neutron or WIMP induced nucleation events [57]. The COUPP experiment [18], which uses bubble chamber of CF_3I liquid instead of SDD also confirms this observation. It is to be noted that this effect was not observed when the peak of droplet radius distribution of the PICASSO detector was 5 μm or lower. At present, the PICASSO experiment has achieved 99.34 % alpha particle rejection at 80 % WIMP acceptance [78]. On the other hand, the SIMPLE collaboration [58] which uses the active liquid C_2ClF_5 (b.p. -39.1 °C) droplets of radius $\sim$ 30 μm (as compared to PICASSO's droplet radius $\sim$ 100 μm) has recently reported WIMP acceptance of greater than 97 %, significantly better than that obtained by PICASSO. The SIMPLE experiment also finds α-induced events are of larger amplitudes than the neutron-induced events. However the SIMPLE experiment uses electret microphone to record information from the low frequency components of the pulse associated with the nucleation events as opposed to only high frequency components (> 18 kHz) recorded by PICASSO experiment.

In order to investigate the result obtained by the SIMPLE experiment with an aim towards achieving better WIMP acceptance for the PICASSO experiment, in the present work we study the effect of using droplets of smaller sizes than those used in usual PICASSO detectors (radius $\sim 100\ \mu$m) and also the effect of recoding the low frequency components of the pulses on discrimination between alpha and neutron induced events. We have performed separate experiments with droplets of two different radius distributions. For our experiments, we have fabricated SDDs with R-12 (CCl_2F_2; b. p. -29.8 °C) as the sensitive liquid which we expect to yield similar results as those with liquid C_2ClF_5 used in the SIMPLE experiment. We have condenser microphone to record the acoustic pulses arising from bubble nucleation events. The condenser microphone records the information from the low frequency components of the pulse associated with a nucleation event. Pulses are recorded in presence of ^{241}Am-Be and ^{252}Cf neutron sources and ^{241}Am α-source. The analysis of acoustic signals has been carried out to find the variables which are capable of discriminating between the neutron and α-particle induced events.

7.2 Present work

7.2.1 Experimental setup

We have performed four different experiments with SDDs made of superheated droplets of R-12, dispersed in soft aquasonic gel matrix. The pulses from the detector due to neutrons and α-particles from neutron sources ^{241}Am-Be (3 Ci) and ^{252}Cf (3.2 μCi) and α-source ^{241}Am (30 particles s^{-1}) are recorded at the temperature of 33.5±0.5 °C.

Experimental set up with α-source ^{241}Am is shown in Figure 7.1a. The same type of setup was used with the neutron source, ^{241}Am-Be, the difference is that in this case the source was kept at 1.4 meter away from detector. In this setup (Figure 7.1a) the superheated droplets of R-12 immersed in the soft aquasonic gel matrix were kept in a perspex box. The temperature of the detector was varied

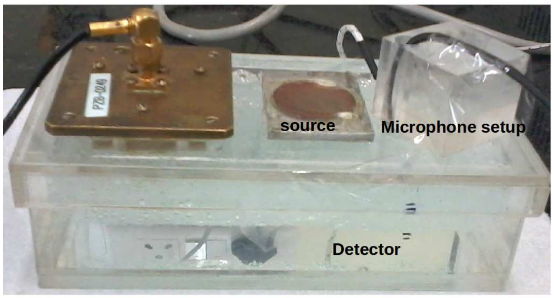

(a)

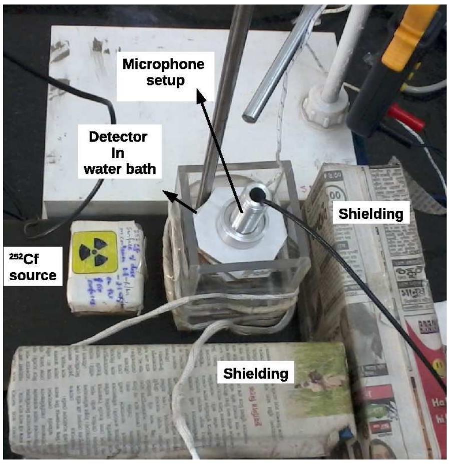

(b)

Figure 7.1: Experimental setup to measure the acoustic response of (a) α-particle induced events in presence of ^{241}Am α-source, (b) neutron induced events in presence of ^{252}Cf source.

by wrapping the perspex box with a heating coil and was controlled by using a temperature controller (Metravi) of precision $\pm 1\,^{\circ}$C. In the case of neutron source ^{252}Cf (Figure 7.1b), the superheated droplets of R-12 were kept in a glass vial which was placed in a similar temperature controlled water bath as mentioned above. Here the temperature of the detector was measured using the temperature sensor (225A Metrix) of precision $\pm 1\,^{\circ}$C. The condenser microphone used to detect the pulses was placed in such a way that its active surface touched the upper surface of the gel matrix (shown in Figure 7.1). The traces of the electrical signal output from microphone were recorded using LabVIEW for α-particle induced events and in presence of ^{252}Cf neutron source. In the case of ^{241}Am-Be neutron source, the experiment was performed in a different laboratory where due to inconvenience of acquiring data by LabVIEW, digital storage oscilloscope was used for data storage

.

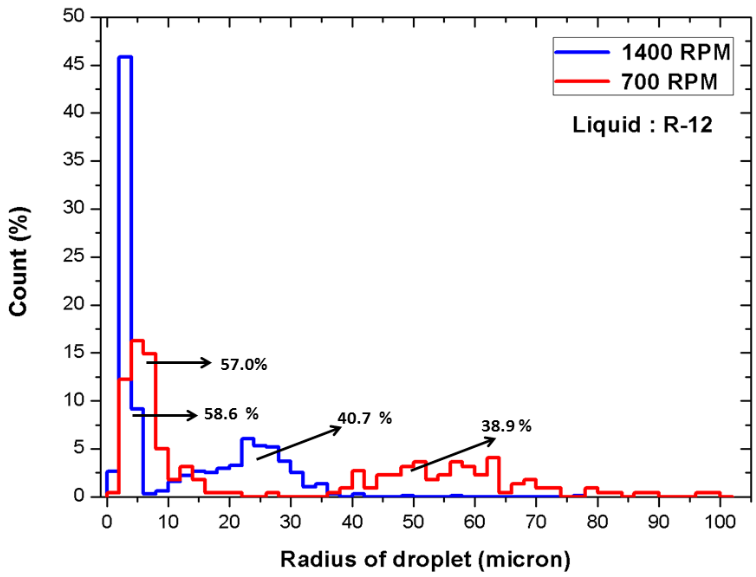

Figure 7.2: Distribution of radius of droplets created with 700 RPM (red line) and 1400 RPM (blue line). For 1400-RPM droplets, the droplets with radii less than 10.0 μm and those with radii in the range 10.0 - 38.0 μm constitute about 58.6 % and 40.7 % of the total distribution, respectively. For 700-RPM droplets, the droplets with radii less than 22.0 μm and those with radii in the range 36.0 - 74.0 μm constitute about 57.0 % and 38.9 % of the total distribution, respectively.

7.2.2 Droplet radius distribution

As discussed in Chapter 4, the droplets are produced by adding the R-12 liquid on the top of degassed soft supporting gel medium in a stainless steel high pressure chamber and by stirring the liquid. Droplets of different size distributions can be produced by rotating the stirrer with different rotation frequencies. For our experiment, we have used two different stirrer rotation frequencies, namely, 1400 RPM and 700 RPM. The resulting droplets for the two cases will be referred to as "1400-RPM droplets" and "700-RPM droplets", respectively. It is to be noted that during experiments with α-source (^{241}Am) both types of droplet distributions were used while ^{241}Am-Be was used only in the case of detector with 1400-RPM droplets and ^{252}Cf neutron source was used in the case of 700-RPM droplet detector. The radii of droplets are calculated from direct measurements of the volume of the vapour bubble (resulting from the nucleation of the droplet) observed under a microscope using Pharma Pro 4.2 software. The resulting radius distribution of the droplets is shown in Figure 7.2. From this Figure, it is observed that the droplet radius distribution for both the RPMs is bimodal and broadly divided into two regions, and the overall distribution shifts to lower droplet radii for higher rotation frequency.

For the case of 1400 RPM, the first sharp peak of the radius distribution is at 2.0 - 4.0 μm bin and the second broad peak spans the radius range of about 10.0 - 38.0 μm (about 40.7 % of the total distribution). The droplets with radius less than 10.0 μm constitute about 58.6 % of the total distribution for the case of 1400 RPM.

For the droplets created with 700 RPM, the first peak is at 4.0 - 6.0 μm bin and the second broad peak spans the radius range of about 36.0 - 74.0 μm (about 38.9 % of the total distribution). The droplets with radius less than 22.0 μm constitute about 57.0 % of the total distribution for 700 RPM.

7.2.3 Calculation of stopping power and range of charged particles

The range and stopping power or LET (Linear Energy Transfer) has been calculated using SRIM 2008 code [50] for α-particle and neutron induced recoil nuclei for both the sources, ^{241}Am-Be and ^{252}Cf, and are shown in Tables 7.1 and 7.2, respectively.

^{241}Am decays to ^{237}Np by emitting an α-particle : $^{241}\mathrm{Am} \rightarrow {}^{237}\mathrm{Np} + \alpha + 5.64$ MeV. From conservation of momentum, it can be calculated that recoil energy of ^{237}Np is about 93.60 keV. The energies of α-particle for ^{241}Am decay are 5.48 MeV (85.2 %) and 5.44 MeV (12.8 %). During the experiment, α-particles from the source traversed through 1.5 cm of air path before reaching the emulsion. The energy loss of 5.48 MeV α-particles through air path is estimated to be about 1.34 MeV, using the stopping power obtained from SRIM 2008 [50] for air of density 1.2484×10^{-3} gm/cc. As a result, α-particles entered the emulsion with energy about (5.48 - 1.34) MeV = 4.14 MeV. The Bragg peak of α-particle in R-12 liquid occurs at an energy of 650 keV. The stopping power and the range of α-particle at Bragg peak in R-12 are tabulated in Table 7.1.

Table 7.1: Range and stopping power (dE/dx) of α-particle using SRIM 2008 [50].

Medium with density (gm/cc)	Energy of α particle (MeV)	Range	dE/dx (MeV/mm) or (keV/μm)
Air (1.2484×10^{-3})	5.48	40.16 mm	8.939×10^{-2}
R-12 (1.29)	4.14	32.58 μm	92.74
	0.650	4.93 μm	182.12
Glycerine (1.24)	4.14	22.55 μm	127.70

For the calculation of stopping power and range for neutron induced recoils, the neutron of energy 4.0 MeV for ^{241}Am-Be and of 700 keV for ^{252}Cf [63], corresponding to the peaks of the respective energy spectra, are considered. The energy loss through air and the perspex box or the glass vial is not considered in the above calculations. Due to elastic collision with the neutron, three recoil nuclei, $^{12}C_6$, $^{19}F_9$ and $^{35}Cl_{17}$, can be produced in R-12. The maximum energies ($E^i_{\mathrm{R,max}}$) of the three recoil nuclei ($^{12}C_6$, $^{19}F_9$ and $^{35}Cl_{17}$) produced by the neutron passing through R-12 liquid are obtained by considering elastic head on collision of the neutron with the nucleus. This gives $E^i_{\mathrm{R,max}} = 4AE_{\mathrm{n}}/(A+1)^2$, where E_{n} is the energy of neutron and A is the mass number of the nucleus. The range and dE/dx of these recoil nuclei in R-12 are shown in Table 7.2. Tables 7.1 and 7.2 show that the energy deposition is more localized in case of recoil nuclei than α-particles.

Table 7.2: Range and stopping power (dE/dx) of recoil nuclei in R-12 (1.29 gm/cc) using SRIM 2008 [50].

Source	Recoil nuclei	Max. energy from elastic collision	Range (μm)	dE/dx (MeV/mm) or (keV/μm)
^{241}Am-Be	$^{12}C_6$	1.14 MeV	4.45	488.43
	$^{19}F_9$	0.760 MeV	3.10	343.78
	$^{35}Cl_{17}$	0.432 MeV	1.16	320.0
^{252}Cf	$^{12}C_6$	198.8 keV	1.38	155.22
	$^{19}F_9$	133.0 keV	0.72	142.52
	$^{35}Cl_{17}$	75.6 keV	0.18	351.10

A comparative study of the energy losses for the α-particles and neutron induced carbon, fluorine and chlorine nuclei in R-12 liquid are shown in Figure 7.3. It is seen that the stopping power for α-particles at Bragg peak is almost equal to the stopping power for chlorine at about 1 keV and of fluorine and carbon at about 300 keV.

As mentioned in Chapter 2, radiation-induced bubble nucleation occurs when the deposited kinetic energy ($E_{\rm dep}$) of a traversing particle exceeds a certain critical minimum energy, $E_{\rm c}(T)$. The effective path length can be expressed using the relation, $L_{\rm eff} = \frac{E_{\rm c}(T)}{dE/dx}$ and also in terms of the critical radius, $r_{\rm c}(T)$ as $L_{\rm eff} = ar_{\rm c}$, a is the nucleation parameter, discussed in more details in Chapter 2. $L_{\rm eff}$ is also known as critical length. The value of critical radius ($r_{\rm c}$) and critical minimum energy ($E_{\rm c}$) used in the calculation of $L_{\rm eff}$ and a, are obtained by fitting the data from Ref. [10] ($E_{\rm c}$ is denoted as W_o in the Ref. [10]) using exponential functions.

The calculated values of the effective path length ($L_{\rm eff}$) for nucleation and the related nucleation parameter (a) at the operating temperature 33.5 °C are shown in Table 7.3. It is seen that in the present case, the effective path length ($L_{\rm eff}$) is always smaller than the ranges of α-particles and the recoil nuclei. This implies that

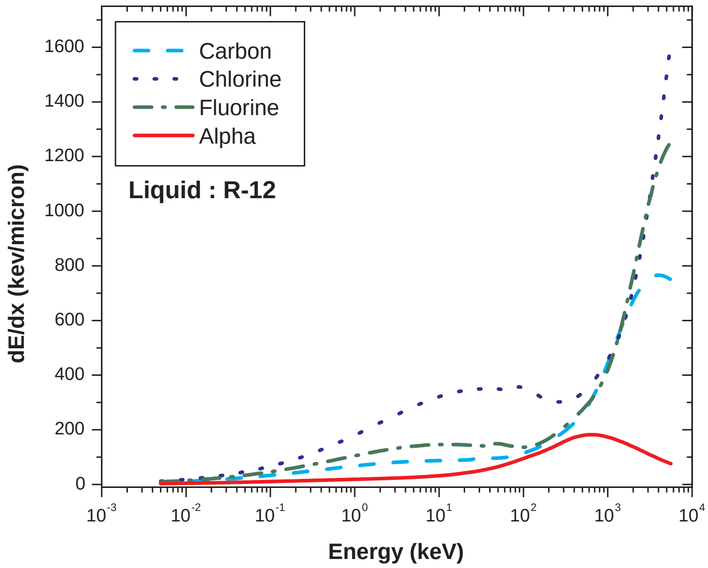

Figure 7.3: Stopping power in keV μm^{-1} for carbon (dashed), fluorine (dash-dotted), chlorine (dotted) nuclei and α-particles (continuous) in R-12 (density 1.29 gm/cc) calculated using SRIM 2008 [50].

for both the cases (i.e. α-particle as well as recoiling nuclei) many nucleation sites are produced along the tracks of the particles within a droplet. In the last column of Table 7.3, the possible numbers of protobubbles or nucleation sites ($N_{\rm protobubble}$) along the track of a particle are calculated using the values of effective path length ($L_{\rm eff}$) and the ranges of the particles (obtained from Tables 7.1 and 7.2). The amplitude of the acoustic signals associated with nucleation events is expected to be dependent on $N_{\rm protobubble}$.

Table 7.3: Calculation of nucleation parameter (a) and number of protobubble created along the track of the particle.

T= 33.5 °C, E_c= 3.153 keV, r_c= 0.021 μm, $\frac{E_c}{r_c}$ = 150.14 keV/μm

Source	Particle or recoil nuclei	dE/dx (keV/μm)	$L_{eff} = \frac{E_c}{\frac{dE}{dx}}$ (μm)	$a = \frac{L_{eff}}{r_c}$	$N_{protobubble} = \frac{Range}{L_{eff}}$
^{241}Am	α	92.74 (min)	0.034	1.62	$\sim$ 958
		182.12 (max)	0.017	0.810	$\sim$ 290
^{241}Am-Be	$^{12}C_6$	488.43	0.006	0.29	$\sim$ 742
	$^{19}F_9$	343.78	0.009	0.43	$\sim$ 344
	$^{35}Cl_{17}$	320.0	0.010	0.48	$\sim$ 116
^{252}Cf	$^{12}C_6$	155.22	0.020	0.95	$\sim$ 69
	$^{19}F_9$	142.52	0.022	1.05	$\sim$ 63
	$^{35}Cl_{17}$	351.10	0.009	0.43	$\sim$ 153

7.3 Results and discussion

7.3.1 Typical raw signal and signal processing

In this work, the trace of the signal and the power spectrum of the signal are analyzed using ROOT software [85]. The raw signals from oscilloscope and LabVIEW have different sampling rate and time span. All signals are normalized to a same sampling rate (50 k samples/sec) and same time span of 20 ms. Those modified signals are then passed through a 150 Hz high-pass filter using a LabVIEW program. The pulses due to noise are rejected by eye selection. The traces of a few rejected events attributed to noise arising during experiment, in the presence of α-source are shown in Figure 7.4. Some of these noise pulses are also observed in a separate experiment which is performed with freon-less detector (gel matrix without active liquid) at the temperature of 33.5±0.5 °C. Figure 7.5 shows the typical raw signal obtained from LabVIEW. The right panel shows the same signal by zooming on 20 ms time duration of the signal. The amplitude of the signals is in unit of Volt.

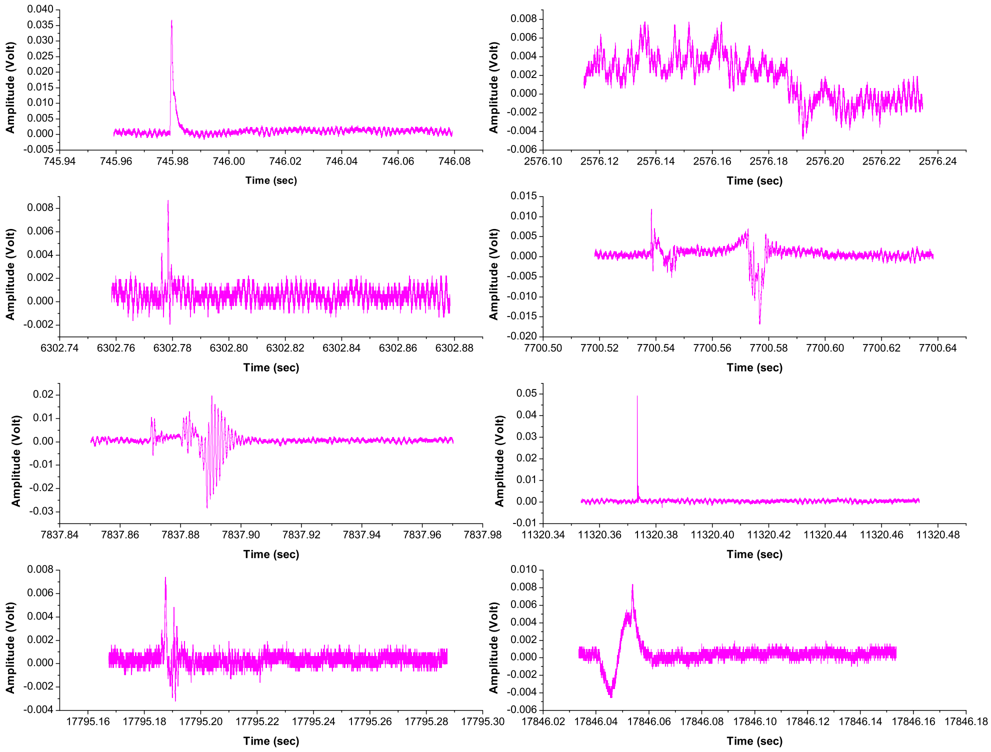

Figure 7.4: A sample of the traces of some rejected noise events.

Figure 7.6 (left) shows the typical event measured by the microphone after passing the signal through the previously mentioned high-pass filter, and Figure 7.6 (right) shows the power spectrum of the same filtered signal obtained by taking the Fast Fourier Transform (FFT) computed using LabVIEW.

7.3.2 Filtered signal

In order to study the filtered signals (shown in Figure 7.6 (left)), we define a variable $\mathrm{S_A} = \sum_{i=0}^{1000}(\mathrm{A}_i^2)$, where A_i is the amplitude (in unit of Volt) of the signal at the i^{th} time bin and the summation extends over the time duration of the signal, taken to be 20 ms for both the neutron and α-particle induced events. Clearly,

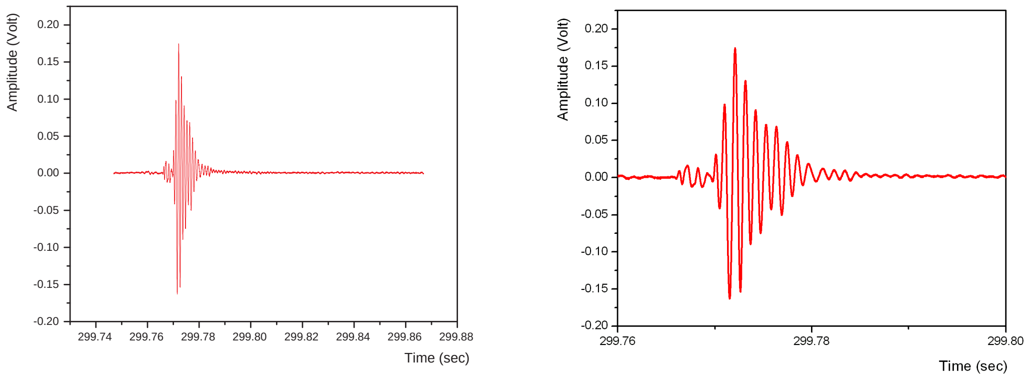

Figure 7.5: Typical raw signal from microphone (left) and zoomed raw signal (right).

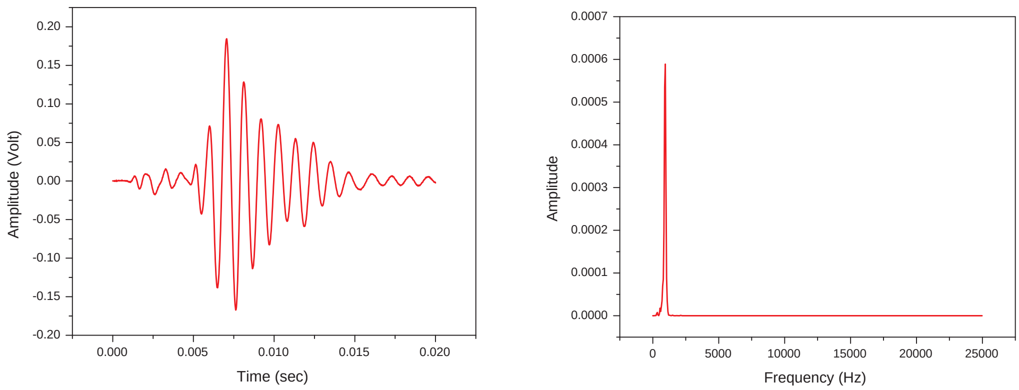

Figure 7.6: Filtered signal after processing (left) and power spectrum of the filtered signal (right).

the variable S_A is a measure of the energy associated with the bubble nucleation process.

Figure 7.7 shows the distribution of the variable S_A for neutron and α-particle induced events for 700-RPM droplets (top panel) and 1400-RPM droplets (bottom panel). It is observed that, for 700-RPM droplets, the α- and neutron induced

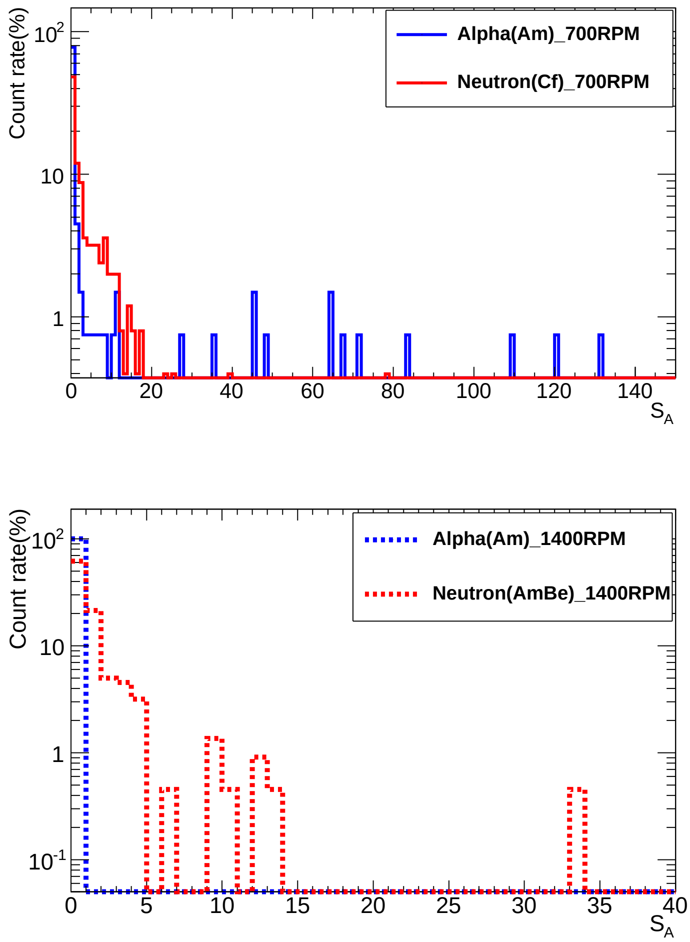

Figure 7.7: Distribution of the variable S_A for 700-RPM droplets (top) and 1400 RPM droplets (bottom) of R-12 liquid.

events overlap in the low S_A region, while the higher S_A region above $S_A = 40$ is populated mainly by the large pulses due to α-particle induced nucleations with a very small contribution from neutron induced events found there. On the other hand for 1400-RPM droplets, while the relevant overall range of S_A populated by the two types of events is comparatively smaller (spans up to $S_A \sim 40$), relatively higher S_A ($S_A \geq 1.0$) is now populated mainly by neutrons with essentially no alpha - induced events there. Note, however, that in both cases (i.e. for 700-RPM as well as 1400-RPM), there may be very little neutron induced events above $S_A \simeq 40$.

Now to focus on the low S_A region, in Figure 7.8, we plot the distribution of the events in the variable $P = \log_{10} S_A$ instead of S_A. It is observed that α-particle induced pulses having P< -1 constitute about 58.2 % and 92.3 % of the total pulses for the 700-RPM droplets and 1400-RPM droplets (see Figure 7.8), respectively. The P-distribution of alpha particle for 700-RPM droplets (top panel of Figure 7.8) can be divided into three regions :

(a) a low P ($P < -1$) region where the distribution strongly overlaps with the distribution of gamma rays and neutron induced events (In Chapter 4, it is shown that the gamma induced events are of smaller P than that of neutron.),

(b) an intermediate region of P ($-1 \leq P \leq 2$) where the α-induced events overlap with neutron induced events,

(c) high P ($P > 2$) region where only α-particle induced events are present.

For the 1400-RPM droplets (bottom panel of Figure 7.8), the α-particle induced events overlap with the gamma induced events but are well separated from the neutron induced events. So, in the case of 1400-RPM droplets, the α-particle induced events can be rejected along with the noise and gamma ray induced events by applying a cut on P at around P = -1.

Figure 7.8 also shows that the spontaneous nucleation events (green histogram) overlap with the α-induced events both for the 1400-RPM and 700-RPM droplets. Thus, the low amplitude pulses during neutron run (with ^{252}Cf neutron source) for droplets of 700 RPM may come from the α-contamination in gel and active liquid.

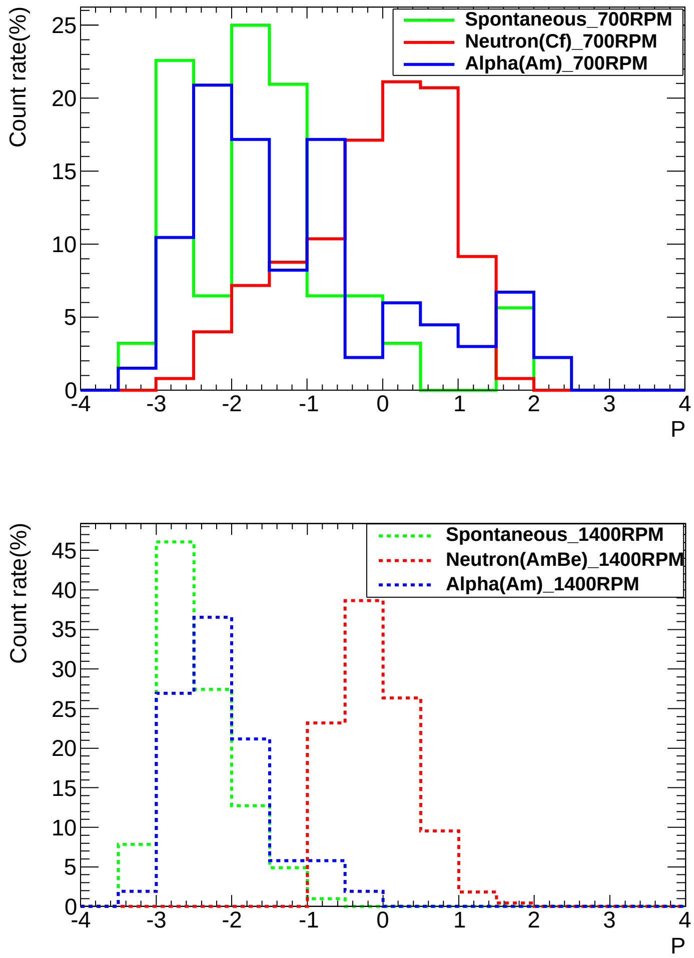

Figure 7.8: Distribution of P variable for neutron and α-particle induced events for 700-RPM (top) and 1400-RPM (bottom) droplets of R-12 liquid. For comparison, the spontaneous nucleation events, occurring at low P region, are also shown.

Amplitude of the pulses carries the information related to the total energy released during the nucleation process [57]. Besides that, the several nucleation sites along the track of a particle in a droplet contribute to the total signal [57].

The ranges of neutron induced recoils (shown in Table 7.2), which in almost all cases are smaller than the diameters of the droplet, are from micron to sub micron order while the effective path length (L_{eff}) is of sub micron order, so there is a probability to create more than one nucleation site in a droplet (shown in

Table 7.3). Table 7.1 and 7.2 show that for neutron induced recoils, energy deposition is more localized than that of alpha particle. The highly localized dE/dx also plays a more important role in the case of neutron induced or recoil nuclei induced bubble nucleation. As a result, the neutron induced pulses are of comparatively higher amplitude as well as of higher value of variable $\mathrm{S_A}$ (or P).

However, if α-source is within the droplet, generally at least two nucleations occurs: (i) one from recoiling nucleus and (ii) the second one or more on the α-particle track. But in the present experiments, α-source was kept outside the detector, so the contribution from recoil nuclei (^{237}Np) is not present, due to its short range. In the present case, the probability of number of protobubbles along the track of 4.14 MeV alpha particle depends on the diameter of the droplet because range of alpha particle in most cases is larger than the diameter of the droplets. From Table 7.3 we see that L_{eff} corresponding to the alpha particle of energy 4.14 MeV is 0.034 μm. So, the value of $N_{\mathrm{protobubble}}$ will be about 176 and 294, respectively, for the α-track length of 6.0 and 10.0 μm corresponding to the peaks of the droplet radius distribution for 1400-RPM and 700-RPM droplets, respectively. Unlike neutron induced events, in the case of α-induced events pulses are present in all the regions of $\mathrm{S_A}$ (or P) depending on the radius of the droplets. The α-particle induced events at lower values of $\mathrm{S_A}$ (or P) in Figures 7.7 and 7.8 may carry the imprint of the events with less number of nucleation sites along the track than that for neutrons. It can be expected that in a large droplet with diameter greater than or equal to roughly about the range of α-particle (32.58 μm), there is a probability to create several nucleation sites along the α-track, which generates a large pulse. But, in the present case, the number of smaller droplets being more than that of larger droplets, the α-particles preferentially induced relatively large number of pulses with relatively smaller acoustic energy. However when the droplet size is small, an α-particle may also hit more than one droplet along its track and create large amplitude pulses due to combine contributions from more than one nucleation events.

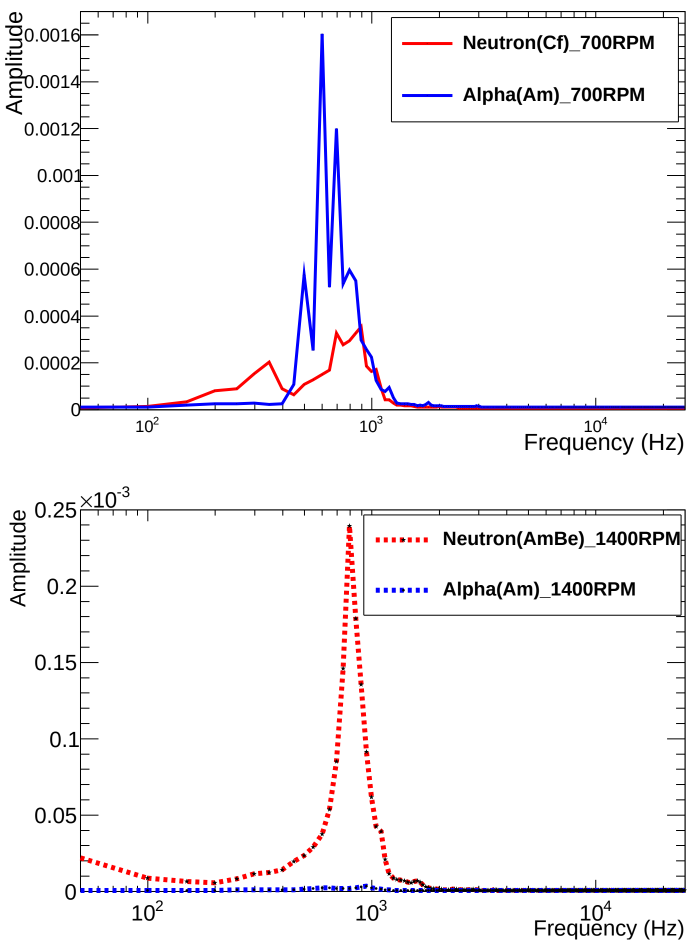

Figure 7.9: Mean of power spectrum for α- and neutron induced events in R-12 liquid for 700 RPM (top) and 1400 RPM (bottom).

7.3.3 Power spectrum of the filtered signal

The power spectrum of the filtered signals (shown in Figure 7.6) can be analyzed to study the frequency spectrum of each pulse measured by condenser microphone. A mean power spectrum over all pulses has been constructed separately for neutron and α-particle induced events. The mean of amplitudes for all events in a given

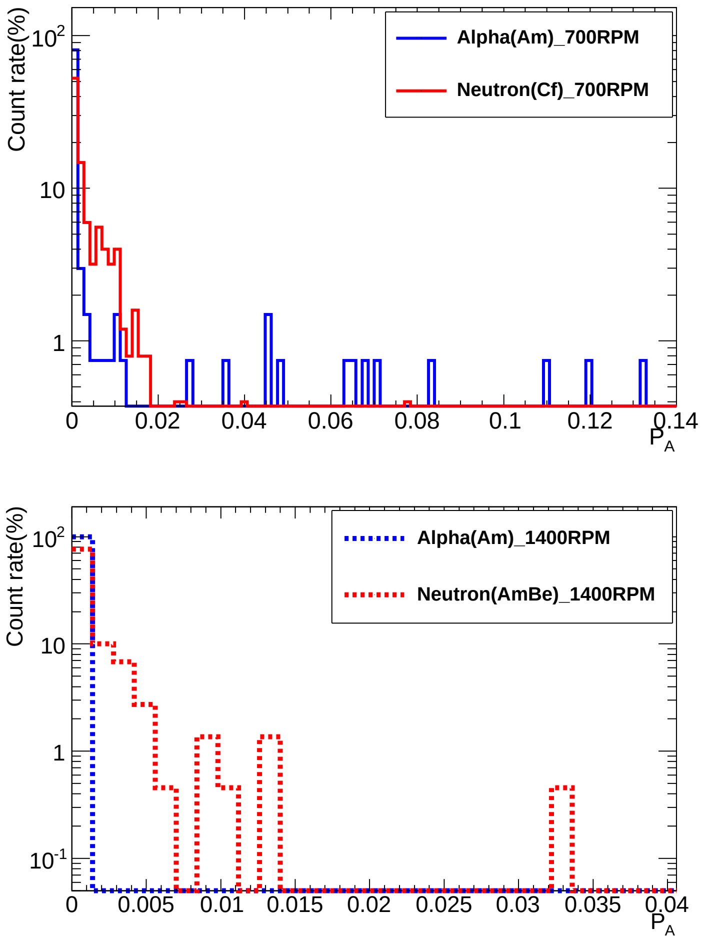

Figure 7.10: Distribution of P_A for 700-RPM (top) and 1400-RPM (bottom) droplets of R-12 liquid.

frequency bin is calculated as $\bar{A}_i = \frac{\sum_j(A_{ij})}{N_{\text{total}}}$, where A_{ij} is the amplitude corresponding to i^{th} frequency bin of the j^{th} event and N_{total} is the total number of events. Figure 7.9 shows plots of $\bar{A}_i$ as a function of frequency for 700-RPM droplets (top panel) and 1400-RPM droplets (bottom panel).

In Figure 7.9, the blue curve corresponds to the mean of 134 α-particle induced events from ^{241}Am α-source, and the red curve is for 251 events due to neutrons from ^{252}Cf neutron source. In the bottom panel of Figure 7.9 the red curve is for 220 events due to neutrons from ^{241}Am-Be neutron source and the blue curve is for 52 events due to α-particles from ^{241}Am α-source. From Figure 7.9 (top), it is seen that for 700-RPM droplets, the mean power spectra for both the neutron- and α-particle induced events have multiple peaks. On the other hand, for 1400-RPM droplets (Figure 7.9 (bottom)), the neutron induced events have a sharp peak while the α-induced events have a flat mean power spectrum with negligible mean amplitude compared to the peak mean amplitude for neutron induced events. The reason behind the multiple peaks of the mean power spectrum for α-particles induced events in the 700-RPM droplet case may be that the different α-particle induced events have different values of primary harmonic within the range of 0.10 - 2.4 kHz of frequency spectrum and also have higher harmonics in the frequency spectrum. During the experiment with 700-RPM droplet, since α-induced events are always present as intrinsic background during neutron run (i.e. with ^{252}Cf neutron source), the mean power spectrum in the case of ^{252}Cf neutron source also shows multiple peaks (see Figure 7.9 (top)) because of the contributions due to α-contaminations. In contrast, in the 1400-RPM droplet case, because of the relatively smaller droplet sizes, the contribution due to α-contaminations is expected to be small.

To further study the power spectrum of pulses, we define the variable, $\mathrm{P_A} = \sum_{i=0}^{25\,\mathrm{kHz}} (\mathrm{A}_i)$. where A_i is the amplitude of power spectrum at the i^{th} frequency bin. The range of frequency is from 0 to 25 kHz. The variable $\mathrm{P_A}$ represents the area under power spectrum. Figure 7.10 shows the distribution of $\mathrm{P_A}$, while in Figure 7.11 the distribution of $\log_{10} \mathrm{P_A}$, is shown in order to focus on the low $\mathrm{P_A}$ region. Figure 7.10 is similar to Figure 7.7, whereas Figure 7.11 is similar to Figure 7.8. Figure 7.10 shows that for 700-RPM droplets, only α-induced events are present in $\mathrm{P_A} > 0.04$ whereas both α and neutron induced events present in the lower $\mathrm{P_A}$ region. It is also seen from Figure 7.11 that for 1400-RPM droplets, the α induced events are well separated from neutron induced events and these are

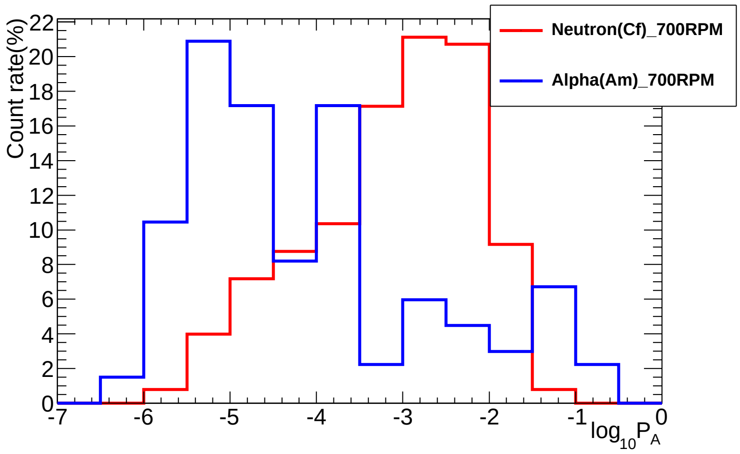

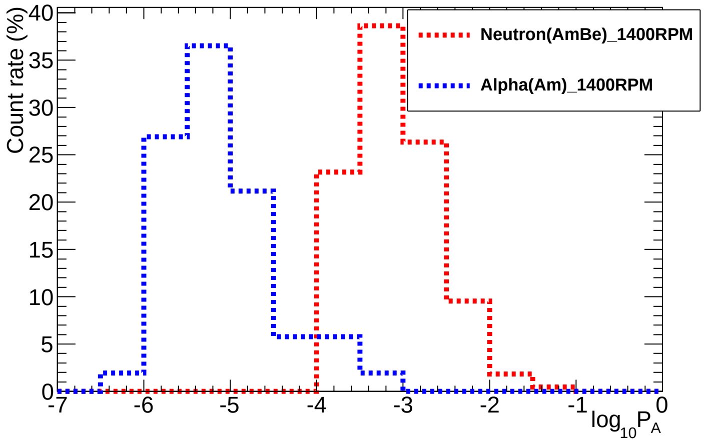

Figure 7.11: Distribution of $\log_{10} \mathrm{P_A}$ for 700-RPM (top) and 1400-RPM (bottom) droplets of R-12 liquid.

in the lower value region of the variable $\mathrm{P_A}$.

7.3.4 Comparison with the results of the SIMPLE experiment

The SIMPLE collaboration has recently presented their results on neutron-alpha discrimination [58]. The sensitive liquid is C_2ClF_5 of total active mass of 0.208 kg, with droplets of radius about 30 μm. The SDDs are immersed in a water pool maintained at a bath temperature of 9.0$\pm$0.1 °C at 2 bar. For liquid C_2ClF_5

(R-115), the critical radius of bubble nucleation at 10 °C is 0.027 μm and critical minimum energy required for bubble nucleation is 4.294 keV [10].

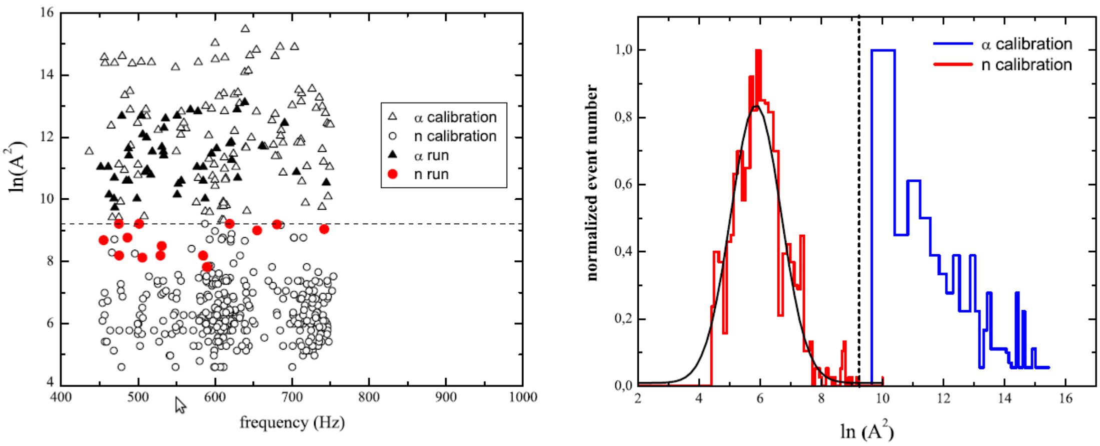

Figure 7.12: Plot from SIMPLE experiment [58].

The particle induced signals are selected as follows : after rejecting the pulses with amplitudes below 2 mV and noise, the remaining each single event is individually inspected. The signals of a characteristic frequency response, with a time span of few milliseconds, a decay time constant of 5 - 40 ms and a primary harmonic between 0.45 - 0.75 kHz, are selected as particle induced nucleation events. The noise events are mainly due to trapped N_2 gas, gas escape, gel fractures and water bubbles.

The scatter plot of the squared maximum amplitude and frequency of the primary harmonics of the particle induced nucleation events obtained by the SIMPLE experiment is shown in Figure 7.12 (left) for both α and neutron runs as well as for the calibration events. A typical histogram of the distribution of the squared maximum amplitudes for neutron and α calibration runs is shown in Figure 7.12 (right).

These two Figures show that the neutron induced events are in general of lower amplitude than α-induced events and are well separated with an acceptance of $>$

97 % for a discrimination cut of $\leq$ 100 mV. In Figure 7.12 (right), it is observed that there is a gap in amplitude between the distribution for alpha particles and neutrons. The droplet size provides a natural lower cutoff to the energy deposited by an alpha particle. The SIMPLE collaboration attribute the observed amplitude gap mentioned above and the observed asymmetry in the distribution of alpha particles to the size of the typical droplets and the typical values of dE/dx relevant in their experiment [58].

Our results using the filtered signals are shown in Figure 7.13 and 7.14 for two sets of droplet size distribution discussed in Subsection 7.2.2, namely, 700-RPM droplets and 1400-RPM droplets, respectively. The left panels of these Figures show the scatter plot of logarithm of the squared maximum amplitude and the frequency of the primary harmonics of the events, and the right panels show the distribution of the logarithm of the squared maximum amplitudes. From Figures 7.13 and 7.14 it is observed that for the 700-RPM droplets the α-particle induced events span a wide range of amplitudes, while for the 1400-RPM droplets the α-induced events are present only in the relatively low - amplitude region. It is also observed that for 1400-RPM droplets about 88.5 % of the total α pulses are well separated from neutron induced events if a discrimination cut is placed for $\ln(\mathrm{A}^2) = 7.6$ (A is in mV). This cut corresponds to about 44.7 mV of maximum amplitude of pulse. For 700-RPM droplets (Figure 7.13 (right)), using the same discrimination cut, it is observed that the small amplitude α-induced signals are about 59.0 % of total number of signals. For neutron induced events, the maximum $N_{\mathrm{protobubble}}(\approx 742)$ is obtained for neutron induced carbon recoil with maximum recoil energy 1.14 MeV. Therefore to obtain the α-induced pulse with larger amplitude than neutron induced events, the droplet diameter is expected to be larger than $(N_{\mathrm{protobubble}})_{\mathrm{carbon}} \times (L_{\mathrm{eff}})_{\mathrm{alpha}} = (742 \times 0.034)\ \mu\mathrm{m} \approx 25.23\ \mu\mathrm{m}$. Thus, it is expected that the most of the small amplitude signals of the α-induced events

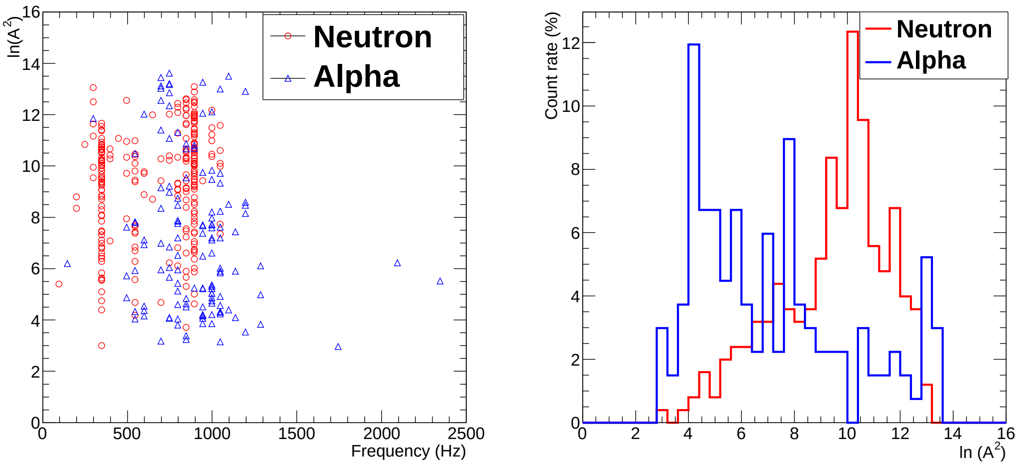

Figure 7.13: The two plots are for experiments with 700-RPM droplets of R-12 liquid. $\ln(\mathrm{A}^2)$ of the filtered signal vs primary harmonic of power spectrum plot (left). The distribution of $\ln(\mathrm{A}^2)$ of α-particle and neutron induced events (right).

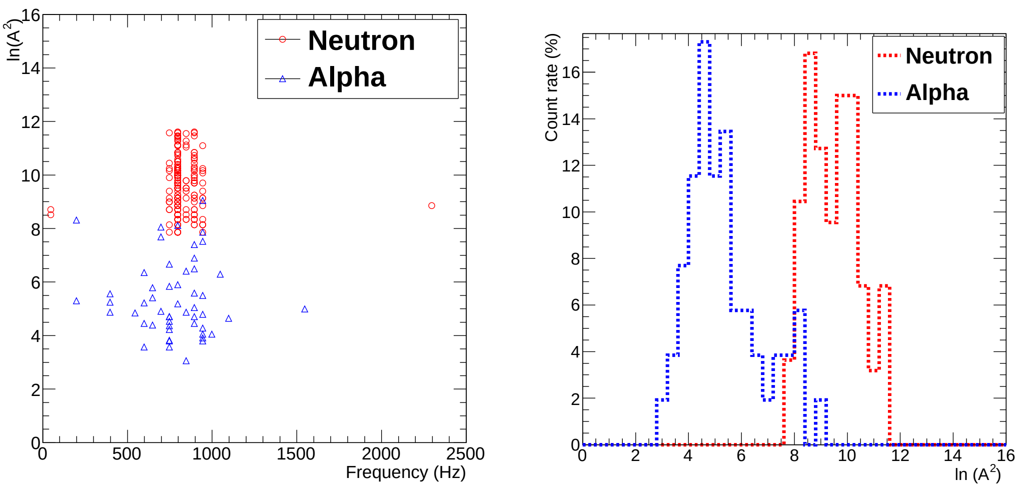

Figure 7.14: The two plots are for experiments with 1400-RPM droplets of R-12 liquid. $\ln(\mathrm{A}^2)$ of the filtered signal vs primary harmonic of power spectrum plot (left). The distribution of $\ln(\mathrm{A}^2)$ of α-particle and neutron induced events (right).

with maximum amplitudes less than 44.70 mV would come from the droplets with radii less than 12.61 μm. From Figure 7.2, it is seen that the droplets with radius less than 12.61 μm are roughly 52.0 % of total number of 700-RPM droplets and 61.2 % of 1400 RPM droplets, thus explaining the broad nature of the curves in Figures 7.13 and 7.14.

It is observed that for SIMPLE the α-induced pulses are of larger amplitudes than neutron induced pulses, which is opposite to our results. The reason behind the relatively larger amplitudes of the α-induced events in the SIMPLE experiment may be that in most cases the α-particles may utilize the whole droplet diameter of 60 μm for creation of protobubbles. But, one expect that there would be also a probability of obtaining small amplitude pulses because some of the α-particles may pass through only a small portion of the whole droplet, which does not seem to be observed in the results of SIMPLE experiment [58]. In contrast to this situation, in our experiment the broad distribution of the radius of droplets provides both small and large amplitude α-induced events. Due to presence of smaller droplets in 1400-RPM droplets than that of 700-RPM droplets, maximum amplitude of acoustic pulses due to alpha particle induced nucleation has comparatively lower value in case of 1400-RPM droplets. It is expected that use of purified detector would give better discrimination in our case.

Our results obtained with condenser microphones sensitive to the low frequency components of the acoustic signal for the case of relatively small droplets of active liquid clearly show for that the alpha-particle induced bubble nucleation events can produce acoustic pulses of smaller amplitudes as well as larger ones than those of neutron induced events in contrast to results from previous studies with PICASSO detector.

Before closing we should mention that our experimental set up and signal processing procedure somewhat differ from those of SIMPLE experiment :

(a) For the SIMPLE experiment reduced superheat (s)[1] was 0.3 while for our experiment it is about 0.45.

(b) Unlike the SIMPLE experiment, our detector was unpurified and fabricated at surface laboratory.

(c) The distribution of droplet radius used by SIMPLE is assumed to be sharply peaked at $\sim$ 30 μm. In our experiments a broad distribution of small size droplets are used, described in Subsection 7.2.2.

(d) The noises appeared in SIMPLE experiment mentioned previously are also not present in our case.

(e) Our signal processing procedure is different from SIMPLE experiment as described before. While we have only used a 150 Hz high-pass filter, in SIMPLE experiment the 'pulse validation routine' is used and the time span, decay constant and primary harmonic of the signals are inspected for selection of particle induced events.

7.4 Conclusions

In this chapter, we have studied the nature of pulses using microphone for α and neutron induced events to study the low frequency components of the acoustic signal. We have used smaller droplets of liquid R-12 than usual PICASSO detector. The analysis work is carried out using the filtered signals and their frequency spectrum with ROOT software. In our experiment with 1400-RPM droplets, the

[1]The 'reduced superheat' (s) [10] represents the normalized operating point of superheated liquid within the temperature range corresponding to the metastable superheated state and is defined as $s = \frac{T-T_b}{T_c-T_b}$ where, T_b is the boiling point, T_c is the critical temperature and T is the ambient temperature of the liquid.

variable, 'P', gives better neutron - alpha discrimination than that with the variable squared maximum amplitude ('$\ln(A^2)$') used by the SIMPLE experiment. In contrast to the SIMPLE result, both smaller and larger amplitude pulses for alpha induced events were observed due to the droplet size distribution. The present study shows that the α-n discrimination works better for smaller droplets (1400 RPM). Among the variables used in this work, the variables 'P' (for filtered signal) and '$\log_{10} P_A$' (for power spectrum of filtered signal) appear to be good variables for discrimination between α and neutron induced events.

Chapter 8

Towards improving the alpha-neutron discrimination

8.1 Introduction

As discussed in Section 5.4, getting rid of the α-background is a major challenge for the PICASSO experiment. In addition to the efforts towards fabrication of more purified detectors with as little α-contamination as possible, another avenue of possible improvements in this regard is the development of double speed electronics to increase the sampling rate of the acquired signal. After development of this electronics, at present we have data with sampling rate 800 kHz, known as the "double speed" run as against the "single speed" run at the sampling rate 400 kHz used earlier.

In the present Chapter, we focus on a new analysis technique to significantly reject the α-background by increasing the resolution of discrimination between α- and recoil nuclei induced events, by taking advantage of the double speed run.

One issue that poses a major problem for the data analysis procedure is that the signal amplitude of the events in any detector decreases with time. This is because, as the number of vapour bubbles (due to nucleated events) increases with time, the resulting mixture of liquid and vapour damps the subsequent acoustic signals due to newly nucleated events, resulting in a decrease in their signal amplitude with time. This shows up as a systematic decrease of the variable “PVAR” described in Section 5.4 with time. This leads to a broadening of the PVAR distribution of the events which, in turn, results in reduced accuracy discrimination between α and recoil nuclei induced nucleation events using the variable PVAR. Below we present two methods of applying corrections to take into account the effect of signal amplitude decrement with time in the full data analysis procedure.

8.2 Time-gain correction

To illustrate the procedure analysis is performed with the PICASSO data for three single speed neutron calibration runs of sampling rate 400kHz, namely the run numbers 0.2779.4, 0.2780.4, 0.2781.4 at 40 °C. The detector 93 of TPCS 1 has been used due to presence of good statistics of events and two good detectors 71, 72 of the same TPCS are also used. To study the effect of the analysis procedure on the present double speed calibration run, ten double speed long duration calibration runs of sampling rate 800 kHz are chosen because large number of events are required for analysis. Three detectors 141, 145 and 147 of TPCS 1 are chosen. The double speed calibration runs are runs 0.5771.4 and 0.5772.4 at temperature 40 °C, runs 0.5773.4, 0.5774.4, 0.6018.4 and 0.6019.4 at temperature 35 °C and runs 0.6020.4, 6021.4, 0.6028.4 and 0.6029.4 at temperature 30 °C. The time duration of all these calibration runs are shown in Table 8.1. The ‘qpicasso’ analysis tool, which is a ROOT software [85] based code, is used for this analysis. This code is used and modified by PICASSO experiment as required.

In Figure 8.1, the distributions of PVAR, FVAR and RVAR variables are shown

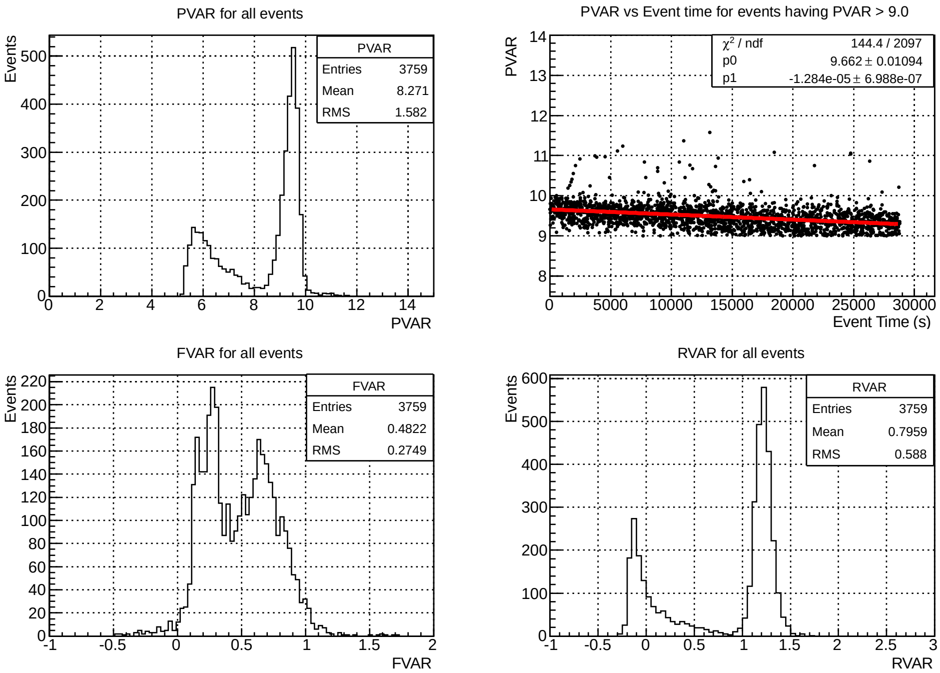

(a) Single speed run 0.2780.4 and detector 93.

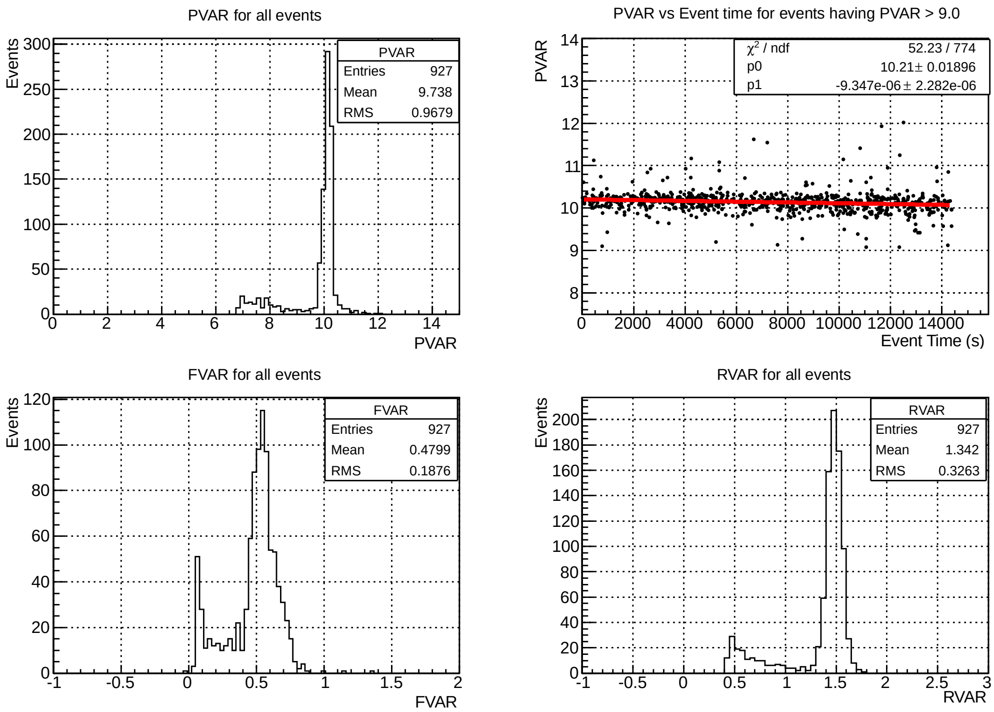

(b) Double speed run 0.6019.4 and detector 145.

Figure 8.1: PVAR, FVAR and RVAR distributions for all events and PVAR as a function of event time for events having PVAR > 9.0 for detector 93, run 0.2780.4 and detector 145, run 0.6019.4 are shown.

Table 8.1: Time duration of calibration runs

Temperature °C	Run	Time duration (hours)
40	0.2779.4	8.0
	0.2780.4	8.0
	0.2781.4	7.1
40	0.5771.4	2.5
	0.5772.4	2.5
35	0.5773.4	3.0
	0.5774.4	3.0
	0.6018.4	4.0
	0.6019.4	4.0
30	0.6020.4	4.0
	0.6021.4	4.0
	0.6028.4	4.0
	0.6029.4	4.0

for a single speed run (run 0.2780.4 of detector 93) and a double speed run (run number: 0.6019.4 of detector 145) at 40 °C. It is observed that for each of the three variables, PVAR, FVAR and RVAR, the distribution has two peaks, first peak at the comparatively low value of the variables is related to the non-particle induced background while the second peak is due to particle induced bubble nucleation, called the "bubble peak".

For all of the cases, it is observed that the variable PVAR (calculated as averaged over nine active piezo transducers) decreases with time for particle induced nucleations having the value of PVAR > 9.0. The cutoff value of PVAR variable (called PCUT) is chosen as 9.0 by eye selection. The variable PVAR as a function of event time for the events having the value of PVAR > 9.0 is shown in Figure 8.1 for two cases —detector 93 used for single speed calibration run 0.2780.4 and detector 145 used for double speed calibration run 0.6019.4. The fitted thick red straight lines with negative slopes indicate the decrement of PVAR with event time. This decrement causes broadening of the PVAR distribution of particle induced nucleation events as mentioned before. It is expected that applying suitable corrections to make the slope of PVAR (as a function of time) zero will improve the resolution of alpha-recoil discrimination by producing narrower PVAR distribution. This type of correction is called as "**time correction**". In the present work, two correction procedures hereafter referred to as Method I and Method II have been developed and the results are compared.

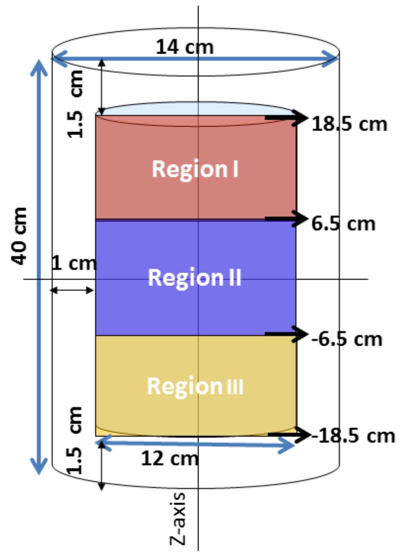

Figure 8.2: Schematic diagram of PICASSO detector with three regions used in analysis.

In the analysis, the fiducial volume is chosen to be about 67.96 % of the actual volume of the detector to reject the events generated at the interfaces of different media. The dimension of each PICASSO detector module is of height 40.0 cm and diameter 14.0 cm. The active part of each detector is topped by a layer of mineral oil of thickness about 1.5 cm . Thus, from the top of the detector a region of thickness 1.5 cm is rejected. To keep the symmetry, same length of region is rejected from the bottom of the detector. A further region of thickness 1 cm on the both sides are rejected in order to avoid events near the detector walls. The remaining fiducial volume is divided into three cylindrical regions, each of diameter 12.0 cm as schematically shown in Figure 8.2. The top and bottom regions (region I and region III) are of height 12.0 cm, and the middle region (region II) is of height 13.0 cm with having z in the following ranges : (i) region I : 18.5 cm $\leq$ z $<$ 6.5 cm, (ii) region II : 6.5 cm $\leq$ z $\leq$ -6.5 cm, and (iii) region III : -18.5 cm $\leq$ z $<$ -6.5 cm.

The co-ordinates of events are obtained from the 'PosMontrealWeight' variable of qpicasso analysis tool. The uncorrected PVAR, FVAR and RVAR variables are denoted as PVAR_raw, FVAR_raw and RVAR_raw in the analysis. The events are first divided into three parts according to the mentioned three regions of the detector. For each of the calibration run, the variables PVAR_raw, FVAR_raw and RVAR_raw are constructed and the distributions are plotted for the events of each region. The second peak of each of the three distributions is fitted by gaussian function and cutoff values, namely PCUT_raw, FCUT_raw and RCUT_raw for the variables PVAR, FVAR, RVAR, respectively, are calculated using the gaussian function in such a way that about 97.5 % of the recoil induced bubble nucleation events having PVAR_raw, FVAR_raw and RVAR_raw greater than the value of PCUT_raw, RCUT_raw, FCUT_raw, respectively, are accepted. Then, for the accepted recoil induced events, the PVAR_raw variable is plotted as a function of event time. This plot for each of the three region is fitted by a straight line individually. For each of the events of a region, a correction factor depending on the slope of the previously mentioned fitted straight line is added to PVAR_raw to make the slope of the PVAR_raw vs event time plot zero. The corrected value of PVAR_raw denoted as PVAR_tc is calculated using the formula PVAR_tc = (PVAR_raw - event time $\times$ slope) for three regions. After time-correction the selection of recoil induced events of a particular region is done using PVAR_tc, FVAR_raw, RVAR_raw with respective cutoff values of PCUT_raw, FCUT_raw and RCUT_raw. The PVAR_tc distribution for all events of three regions after correction are plotted. Finally the PVAR distribution is plotted by adding the selected recoil induced events of three regions and fitted by gaussian function to compare resolution (R). The resolution of the distribution is calculated using the standard deviation (σ) and mean value of PVAR ($\mathrm{PVAR_{mean}}$) from fitted gaussian function of PVAR distribution. The formula used is

$$\text{Resolution (R)} = \frac{\text{FWHM}}{\mathrm{PVAR_{mean}}} \times 100\,(\%) = \frac{2.35482\sigma}{\mathrm{PVAR_{mean}}} \times 100\,(\%) \tag{8.1}$$

The improvement of resolution of the PVAR_raw variable distribution after correction, denoted as improvement factor (I_R), is calculated using the relation

$$\mathrm{I}_R = \frac{\text{R\_raw} - \text{R\_corrected}}{\text{R\_raw}} \times 100\,(\%) \tag{8.2}$$

The flow charts of the steps involved in the correction procedures followed under Method I and Method II are described below for detector 145 and calibration run 0.6019.4 as an example. The basic differences between the two correction procedures are explained below :

(a) In Method I, the variables PVAR_raw, FVAR_raw and RVAR_raw are constructed by taking the average over all the nine active piezoelectric transducers to reduce the solid angle effect, while in Method II the average is taken over the three active transducers of the corresponding region to reduce the effect of damping of amplitude of acoustic signal due to the distance traversed through a medium. For region I, piezoelectric transducers are numbered 0, 1, 2, while for the regions II and III, those are 3, 4, 5 and 6, 7, 8, respectively. The z co-ordinate of the piezoelectric transducers of these three regions are -10.5 cm, 0.0 cm and 10.5 cm, respectively.

(b) It is observed that the positions of bubble peak (second peak: see Figure 8.1) of the distribution of PVAR_raw variable are different for the three regions (see Figure 8.2) of the detector. The possible reason is that PVAR_raw varies with transducers. We shall discuss this later in Section 8.3. As a result, **gain correction** for each of the three regions of the detector becomes also important along with **time correction**. This is done in Method II. The effect of gain correction has been studied separately on the PVAR_raw and the PVAR_tc variables. These gain corrected variables are denoted as PVAR_gc and PVAR_tc_gc, respectively. In gain correction method, a **gain correction factor** is added to the variable to shift the bubble peak of PVAR_raw and PVAR_tc to a constant value, namely, 10.0. The gain correction factor is basically difference between the value 10.0 and the position of bubble peak of each region.

Method I

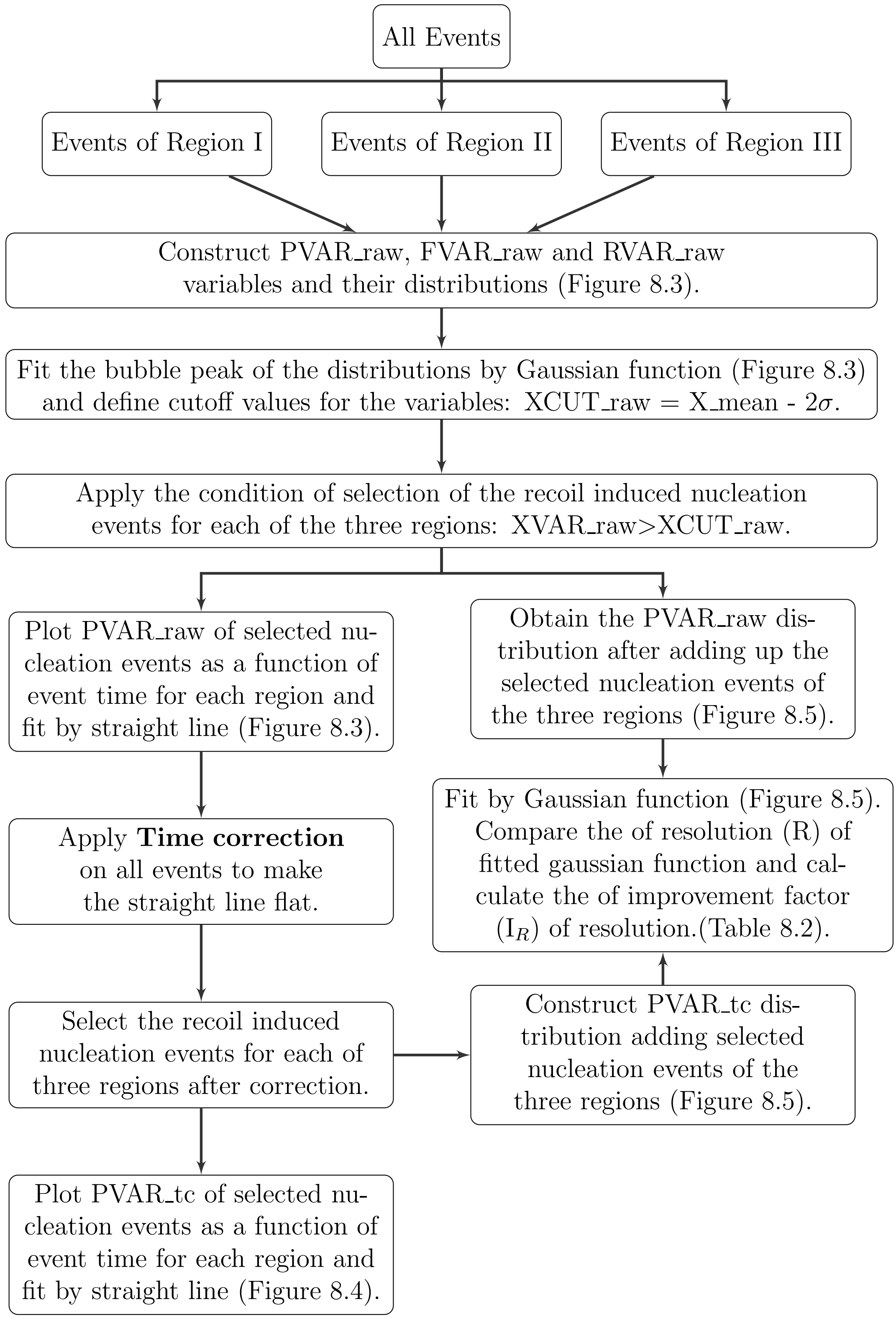
All Events
Events of Region I
Events of Region II
Events of Region III
Construct PVAR_raw, FVAR_raw and RVAR_raw variables and their distributions (Figure 8.3).
Fit the bubble peak of the distributions by Gaussian function (Figure 8.3) and define cutoff values for the variables: XCUT_raw = X_mean - 2σ.
Apply the condition of selection of the recoil induced nucleation events for each of the three regions: XVAR_raw>XCUT_raw.
Plot PVAR_raw of selected nucleation events as a function of event time for each region and fit by straight line (Figure 8.3).
Obtain the PVAR_raw distribution after adding up the selected nucleation events of the three regions (Figure 8.5).
Apply **Time correction** on all events to make the straight line flat.
Fit by Gaussian function (Figure 8.5). Compare the of resolution (R) of fitted gaussian function and calculate the of improvement factor (I_R) of resolution.(Table 8.2).
Select the recoil induced nucleation events for each of three regions after correction.
Construct PVAR_tc distribution adding selected nucleation events of the three regions (Figure 8.5).
Plot PVAR_tc of selected nucleation events as a function of event time for each region and fit by straight line (Figure 8.4).

Method II

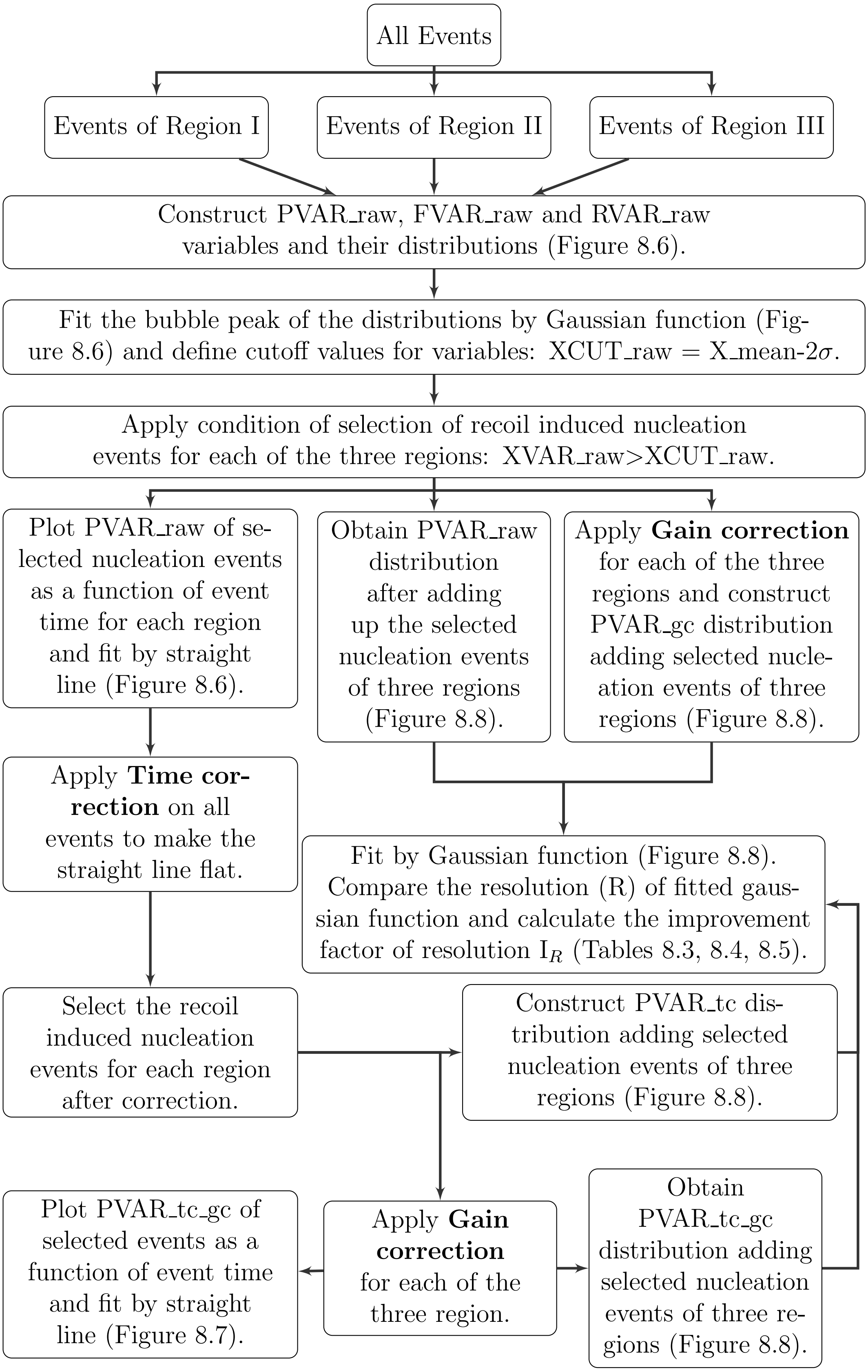
All Events
Events of Region I
Events of Region II
Events of Region III
Construct PVAR_raw, FVAR_raw and RVAR_raw variables and their distributions (Figure 8.6).
Fit the bubble peak of the distributions by Gaussian function (Figure 8.6) and define cutoff values for variables: XCUT_raw = X_mean-2σ.
Apply condition of selection of recoil induced nucleation events for each of the three regions: XVAR_raw>XCUT_raw.
Plot PVAR_raw of selected nucleation events as a function of event time for each region and fit by straight line (Figure 8.6).
Obtain PVAR_raw distribution after adding up the selected nucleation events of three regions (Figure 8.8).
Apply **Gain correction** for each of the three regions and construct PVAR_gc distribution adding selected nucleation events of three regions (Figure 8.8).
Apply **Time correction** on all events to make the straight line flat.
Fit by Gaussian function (Figure 8.8). Compare the resolution (R) of fitted gaussian function and calculate the improvement factor of resolution I_R (Tables 8.3, 8.4, 8.5).
Select the recoil induced nucleation events for each region after correction.
Construct PVAR_tc distribution adding selected nucleation events of three regions (Figure 8.8).
Plot PVAR_tc_gc of selected events as a function of event time and fit by straight line (Figure 8.7).
Apply **Gain correction** for each of the three region.
Obtain PVAR_tc_gc distribution adding selected nucleation events of three regions (Figure 8.8).

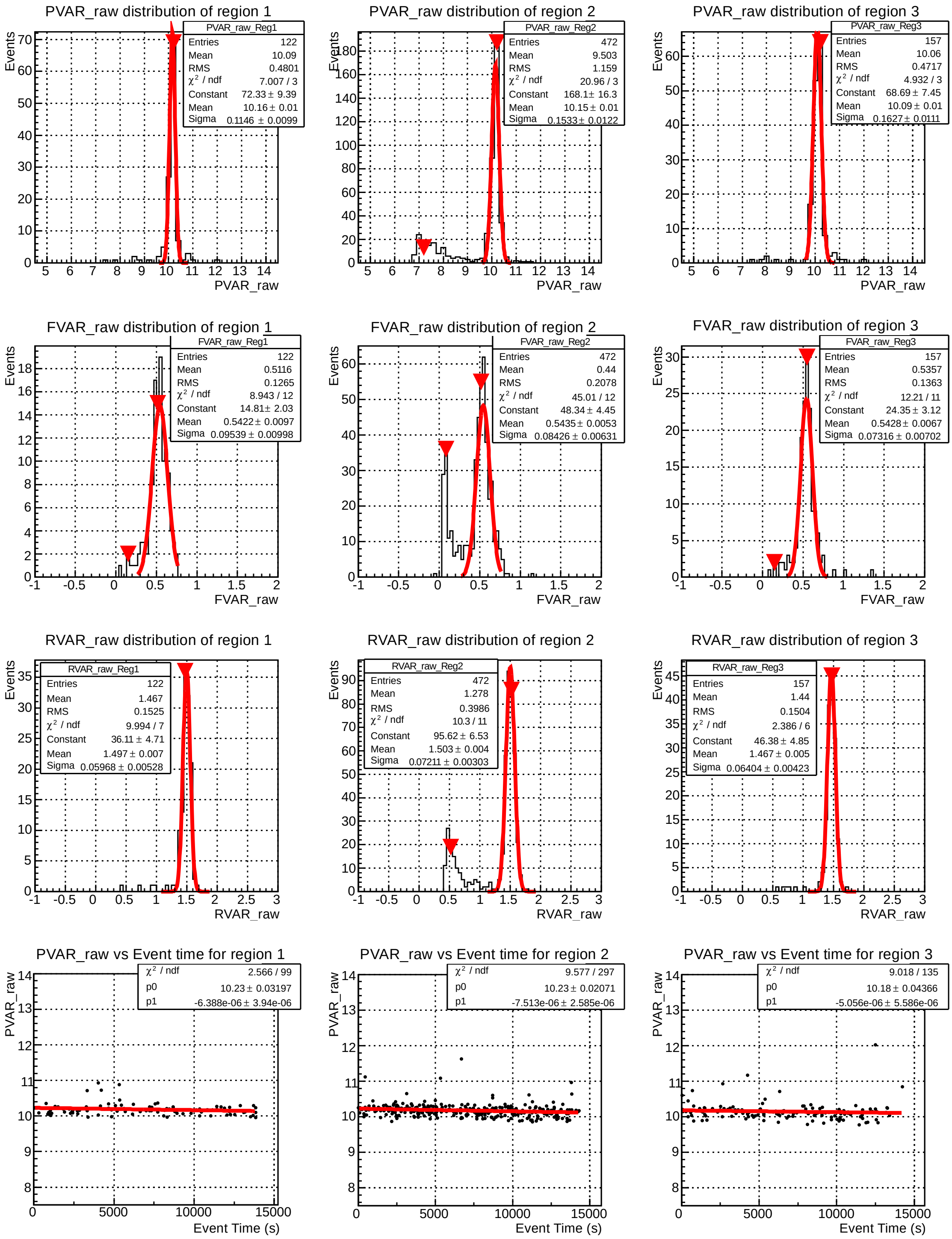

Figure 8.3: PVAR_raw, FVAR_raw and RVAR_raw distributions for three regions in Method I. In the last row, PVAR_raw is plotted as a function of event time for recoil induced bubble nucleation events for run 0.6019.4 and detector 145.

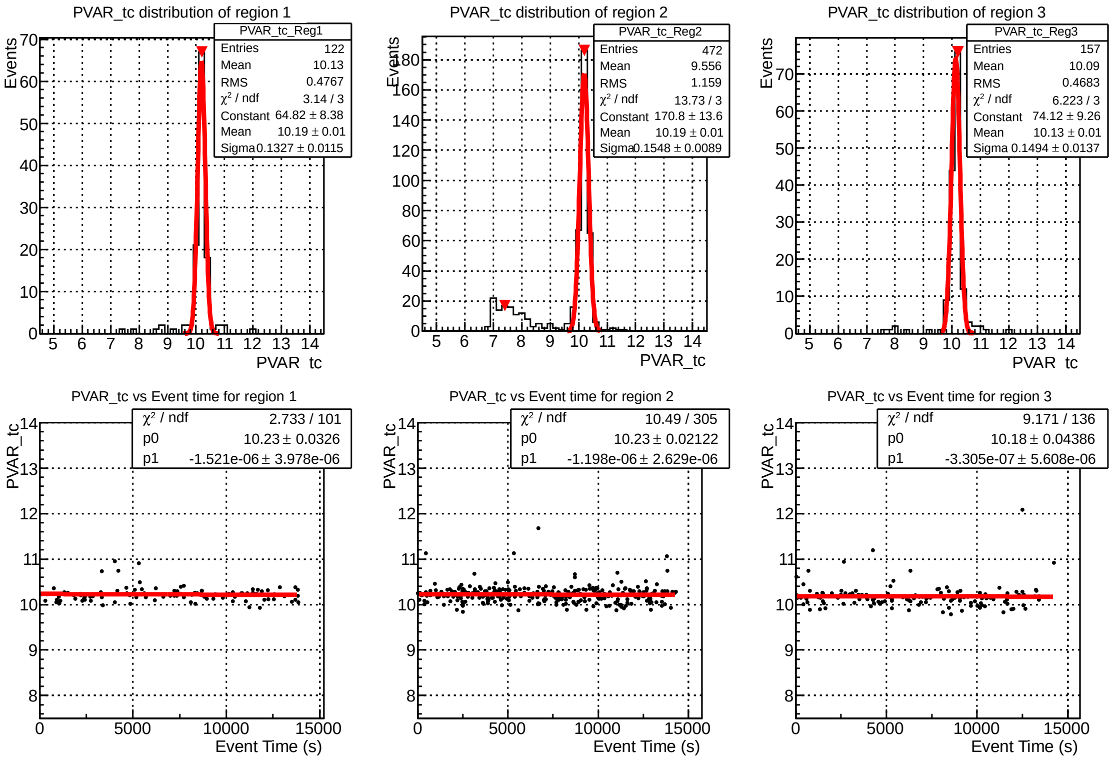

Figure 8.4: PVAR_tc distributions for three regions (above) and PVAR_tc as a function of event time (below) for run 0.6019.4 and detector 145 in Method I.

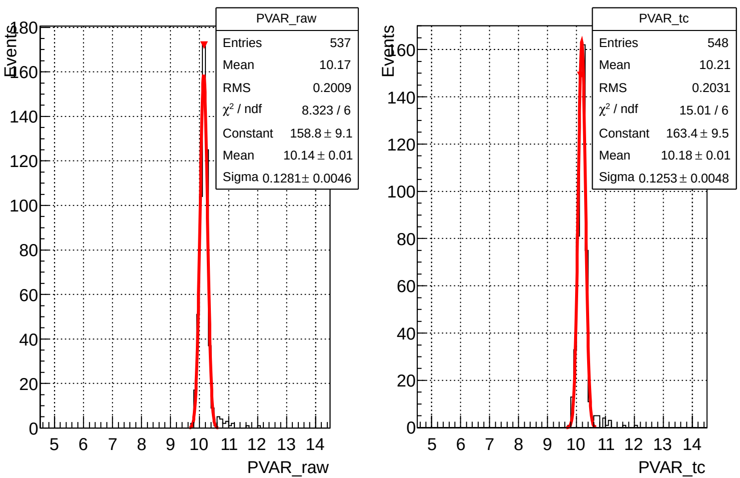

Figure 8.5: PVAR_raw and PVAR_tc distributions (obtained by Method I) of recoil induced nucleation events are shown for run 0.6019.4 and detector 145.

Table 8.2: The resolution (R) of PVAR distribution before and after correction by Method I for detectors 93, 141, 145 and 147.

Detector	Run	PVAR_raw			PVAR_tc			
		σ	Mean	R (%)	σ	Mean	R(%)	I_R (%)
93	0.2779.4	0.2342	9.412	5.860	0.2007	9.593	4.927	15.921
	0.2780.4	0.2211	9.489	5.487	-	-	-	-
	0.2781.4	0.2222	9.680	5.405	0.2050	9.823	4.914	9.084
141	0.5771.4	0.1578	9.853	3.771	0.1484	9.941	3.515	6.789
	0.5772.4	0.1475	9.853	3.525	0.1508	9.911	3.583	-1.639
	0.5773.4	0.1380	9.590	3.389	0.1353	9.636	3.306	2.425
	0.5774,4	0.1462	9.580	3.594	0.1395	9.936	3.409	5.137
	0.6018.4	0.1560	9.575	3.837	0.1443	9.693	3.506	8.626
	0.6019.4	0.1620	9.560	3.990	0.1545	9.627	3.779	5.293
	0.6020.4	0.1474	9.185	3.779	0.1313	9.217	3.355	11.232
	0.6021.4	0.1242	9.146	3.198	0.1298	9.188	3.327	-4.031
	0.6028.4	0.1435	9.154	3.691	0.1359	9.195	3.480	5.718
	0.6029.4	0.1379	9.158	3.546	0.1407	9.915	3.603	-1.620
145	0.5771.4	0.1409	10.47	3.169	0.1435	10.54	3.206	-1.169
	0.5772.4	0.1419	10.46	3.195	0.1536	10.53	3.435	-7.526
	0.5773.4	0.1316	10.16	3.050	0.1316	10.20	3.038	0.392
	0.5774,4	0.1389	10.15	3.223	0.1417	10.20	3.271	-1.516
	0.6018.4	0.1336	10.14	3.103	0.1352	10.24	3.109	-0.209
	0.6019.4	0.1281	10.14	2.975	0.1253	10.18	2.898	2.570
	0.6020.4	0.1305	9.719	3.162	0.1304	9.827	3.125	1.175
	0.6021.4	0.1207	9.709	2.927	0.1509	9.721	3.655	-24.866
	0.6028.4	0.1213	9.728	2.936	0.1184	9.721	2.868	2.320
	0.6029.4	0.1291	9.701	3.134	0.1370	9.748	3.310	-5.608
147	0.5771.4	0.1306	10.17	3.024	0.1277	10.23	2.939	2.794
	0.5772.4	0.1156	10.17	2.677	0.1142	10.18	2.642	1.308
	0.5773.4	0.1007	9.931	2.388	0.09811	9.927	2.327	2.533
	0.5774.4	0.1146	9.910	2.723	0.1106	9.955	2.616	3.927
	0.6018.4	0.1195	9.916	2.838	0.1117	9.968	2.639	7.015
	0.6019.4	0.1128	9.931	2.675	0.1148	9.943	2.719	-1.650
	0.6020.4	0.1109	9.555	2.733	0.1023	9.581	2.514	8.005
	0.6021.4	0.1134	9.533	2.801	0.1123	9.553	2.768	1.177
	0.6028.4	0.09896	9.535	2.444	0.09376	9.550	2.312	5.403
	0.6029.4	0.1114	9.538	2.750	0.1052	9.571	2.588	5.891

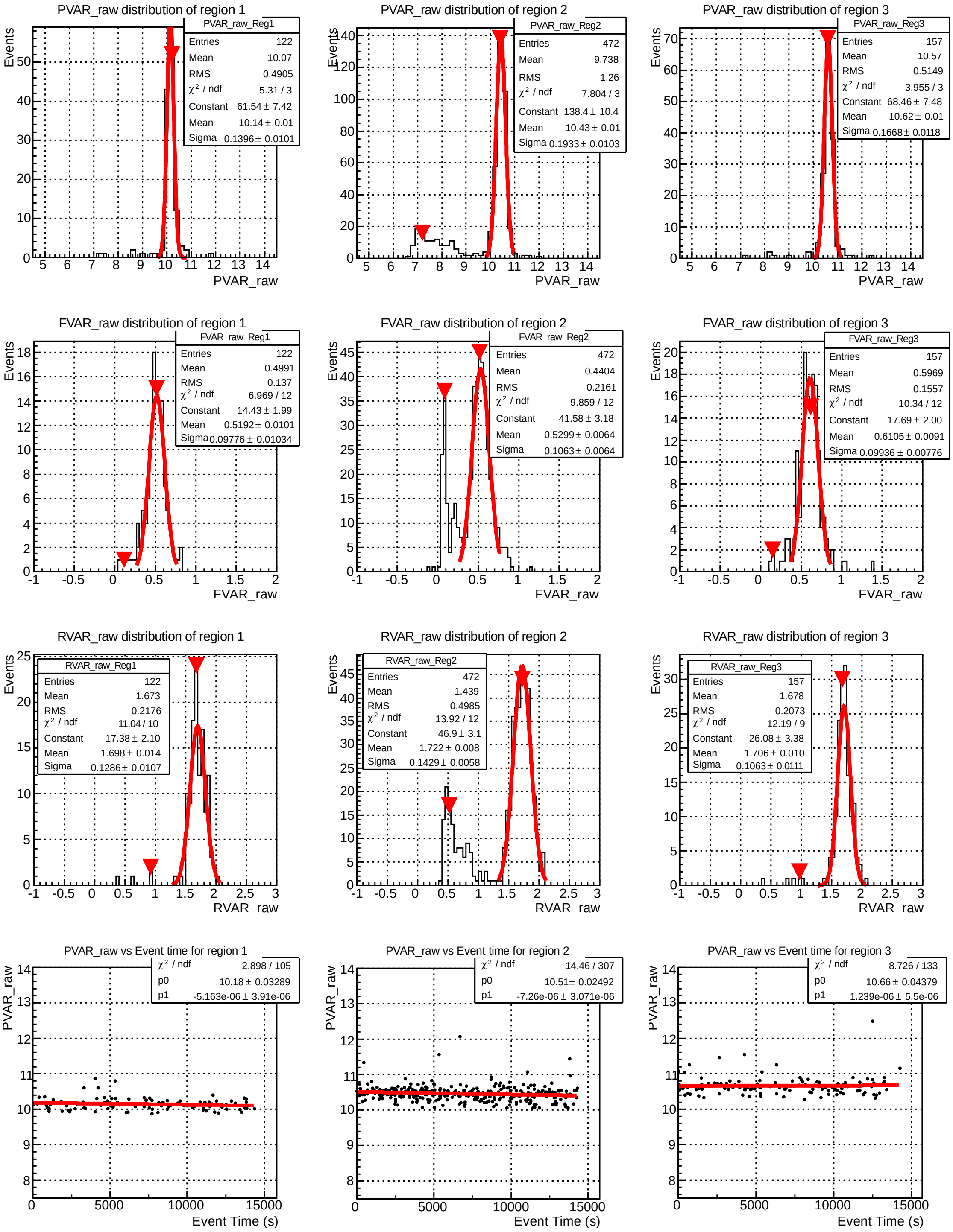

Figure 8.6: PVAR_raw, FVAR_raw and RVAR_raw distributions for three regions in Method II. In last row, PVAR_raw is plotted as a function of event time for recoil induced nucleation events for run 0.6019.4 and detector 145.

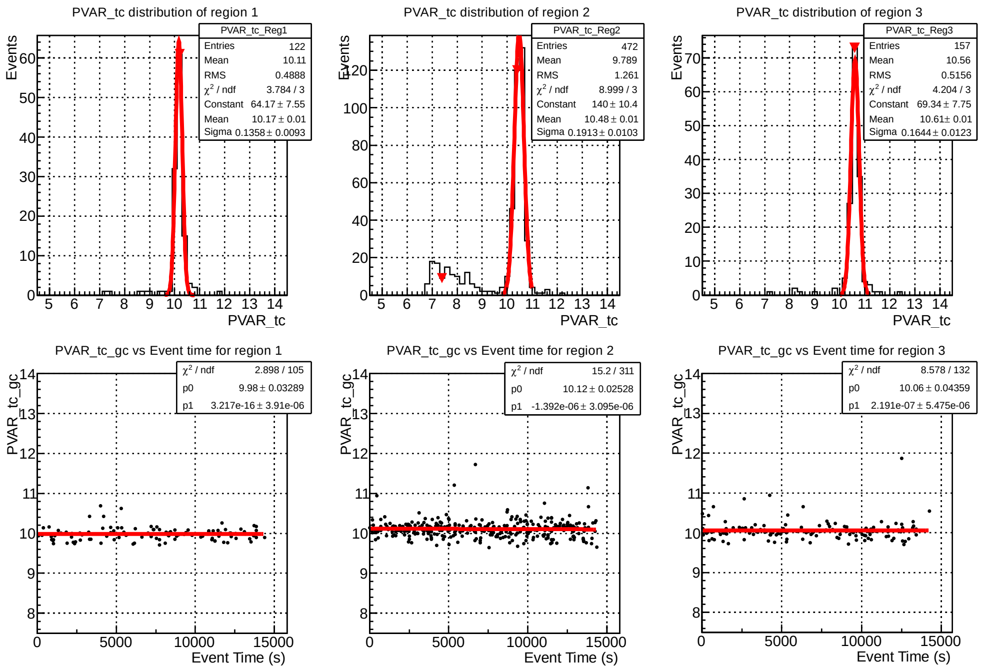

Figure 8.7: PVAR_tc distributions of all events, obtained by Method II for three regions (first row). PVAR_tc_gc of recoil induced events as a function of event time for run 0.6019.4 and detector 145 (second row).

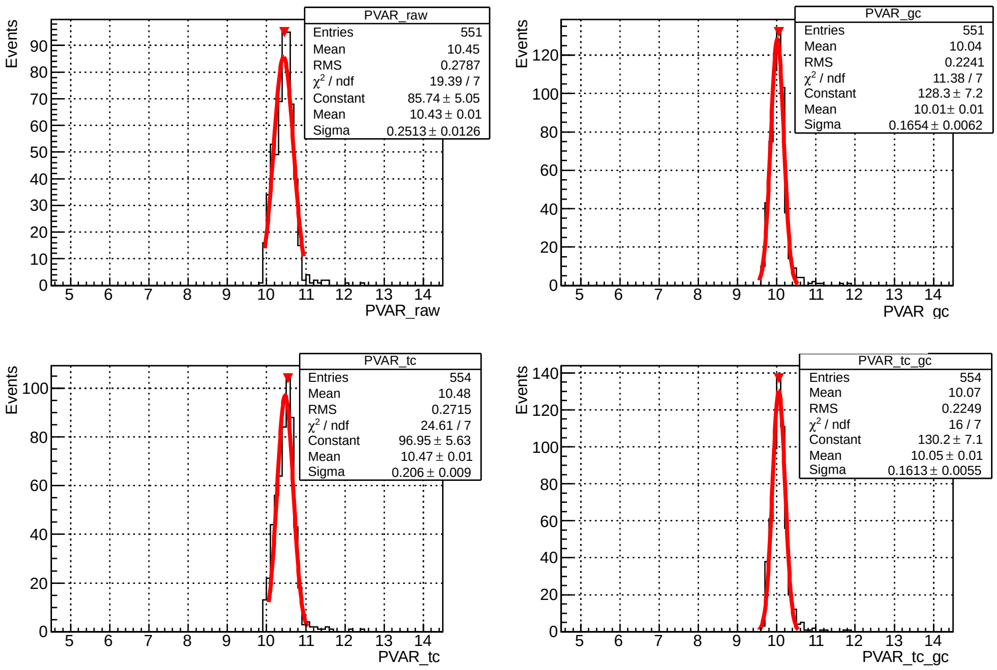

Figure 8.8: PVAR_raw, PVAR_gc, PVAR_tc and PVAR_tc_gc distributions of recoil induced nucleation events, obtained by Method II are shown for run 0.6019.4 and detector 145.

Table 8.3: The resolution (R) of PVAR distribution before and after correction by Method II for detector 141.

Run	PVAR_raw			PVAR_gc				PVAR_tc				PVAR_tc_gc			
	σ	Mean	R (%)	σ	Mean	R(%)	I_R (%)	σ	Mean	R(%)	I_R (%)	σ	Mean	R (%)	I_R (%)
0.5771.4	-	-	-	-	-	-	-	-	-	-	-	-	-	-	-
0.5772.4	0.1684	10.21	3.884	0.1796	10.010	4.225	-8.782	0.1755	10.26	4.028	-3.708	0.1801	10.02	4.233	-8.976
0.5773.4	0.1801	9.96	4.258	0.1708	9.973	4.033	5.287	0.1719	10.0	4.048	4.935	.1634	10.0	3.848	9.636
0.5774.4	0.1701	9.937	4.031	0.1728	9.944	4.092	-1.516	0.181	9.955	4.281	-6.216	0.1813	9.965	4.284	-6.285
0.6018.4	0.1638	9.93	3.884	0.1744	9.940	4.132	-6.364	0.1822	10.04	4.273	-10.015	0.1626	9.977	3.838	1.200
0.6019.4	0.1794	9.953	4.244	0.1763	9.971	4.164	1.905	0.1799	10.01	4.232	0.292	0.1778	10.01	4.183	1.456
0.6020.4	0.1615	9.595	3.964	0.1558	9.990	3.672	7.344	0.1658	9.577	4.077	-2.855	0.1613	9.974	3.808	3.919
0.6021.4	-	-	-	-	-	-	-	-	-	-	-	-	-	-	-
0.6028.4	0.1925	9.518	4.763	0.1761	10.040	4.130	13.276	0.1916	9.537	4.731	0.666	0.1876	9.941	4.444	6.692
0.6029.4	0.1826	9.479	4.536	0.1631	9.998	3.841	15.316	0.1861	9.548	4.590	-1.180	0.1857	9.961	4.390	3.223

Table 8.4: The resolution (R) of PVAR distribution before and after correction by Method II for detector 145.

Run	PVAR_raw			PVAR_gc				PVAR_tc				PVAR_tc_gc			
	σ	Mean	R (%)	σ	Mean	R (%)	I_R (%)	σ	Mean	R (%)	I_R (%)	σ	Mean	R (%)	I_R (%)
0.5771.4	0.2567	10.75	5.623	0.1815	9.963	4.290	23.710	0.2468	10.78	5.391	4.124	0.1656	10.0	3.900	30.651
0.5772.4	0.2186	10.71	4.806	0.1682	10.07	3.933	18.166	0.2378	10.76	5.204	-8.278	-	-	-	-
0.5773.4	0.2172	10.450	4.894	0.1490	10.06	3.488	28.740	0.1821	10.51	4.080	16.639	0.1655	9.959	3.913	20.046
0.5774.4	0.2432	10.490	5.459	0.1959	10.04	4.595	15.839	0.2301	10.50	5.160	5.477	0.1798	10.08	4.200	23.062
0.6018.4	0.2230	10.480	5.011	0.1599	10.07	3.739	25.377	0.2225	10.55	4.966	0.886	0.1680	9.936	3.982	20.536
0.6019.4	0.2513	10.430	5.674	0.1654	10.01	3.891	31.421	0.206	10.47	4.633	18.339	0.1613	10.05	3.779	33.387
0.6020.4	-	-	-	-	-	-	-	-	-	-	-	-	-	-	-
0.6021.4	0.1663	10.100	3.877	0.1532	10.09	3.575	7.786	0.1935	10.05	4.534	-16.935	0.1520	10.08	3.551	8.418
0.6028.4	0.1841	10.110	4.288	0.1639	10.04	3.844	10.352	0.17	10.10	3.964	7.567	0.1653	10.03	3.881	9.496
0.6029.4	0.2065	10.040	4.843	0.1624	10.02	3.817	21.199	0.1787	10.10	4.166	13.977	0.1567	9.939	3.713	23.345

Table 8.5: The resolution (R) of PVAR distribution before and after correction by Method II for detector 147.

Run	PVAR_raw			PVAR_gc				PVAR_tc				PVAR_tc_gc			
	σ	Mean	R(%)	σ	Mean	R (%)	I_R (%)	σ	Mean	R (%)	I_R (%)	σ	Mean	R (%)	I_R (%)
0.5771.4	0.1827	10.48	4.105	0.1626	9.982	3.836	6.562	0.1888	10.52	4.226	-2.946	0.1654	9.962	3.910	4.762
0.5772.4	0.1741	10.47	3.916	0.1571	9.963	3.713	5.173	0.1626	10.47	3.657	6.605	0.1618	10.07	3.784	3.373
0.5773.4	0.1648	10.18	3.812	0.1428	10.01	3.359	11.878	0.1769	10.18	4.092	-7.342	0.1437	10.01	3.380	11.323
0.5774.4	0.1535	10.21	3.540	0.1407	10.03	3.303	6.694	0.1692	10.22	3.899	-10.120	0.1465	10.03	3.439	2.847
0.6018.4	0.1628	10.17	3.770	0.1527	9.994	3.598	4.552	0.1756	10.23	4.042	-7.230	0.1578	10.05	3.697	1.914
0.6019.4	0.1620	10.20	3.740	0.1506	10.03	3.536	5.461	0.1465	10.19	3.385	9.479	0.1374	10.02	3.229	13.662
0.6020.4	0.1782	9.806	4.279	0.1551	10.04	3.638	14.992	0.1748	9.819	4.192	2.038	0.1515	10.05	3.550	17.047
0.6021.4	0.1601	9.788	3.852	0.1474	10.07	3.447	10.511	0.1680	9.801	4.036	-4.795	0.1466	10.08	3.425	11.085
0.6028.4	0.1484	9.793	3.568	0.1382	10.02	3.248	8.983	0.1519	9.802	3.649	-2.265	0.1379	10.02	3.241	9.181
0.6029.4	0.1768	9.807	4.245	0.1586	10.04	3.720	12.376	0.1674	9.811	4.018	5.355	0.1482	10.04	3.476	18.122

8.3 Results and discussion

The PVAR, FVAR and RVAR distributions of Figure 8.1 show that in case of double speed run, number of non-particle induced background events decreases and FVAR distribution has more distinct peak than that in the case of single run single speed run. The probable reason is that in the case of double speed run, comparatively more purified detector has been used. When the events are divided according to three regions, the distribution of all of these three variables indicates that the region II is the most noisy region of the detector. The value of the resolution (R) of PVAR variable before and after correction using Method I are shown in Table 8.2 for the detectors 93, 141, 145 and 147, while the results of Method II for detectors 141, 145 and 147 are shown in Tables 8.3, 8.4 and 8.5.

It is observed that the number of events in the region I of the detector is less than that in the other two regions. In case of Method II, for the double speed run 0.5771.4 and detector 141, this number becomes very small and the fitting of FVAR_raw distribution of region I becomes difficult unlike the fitting of PVAR_raw and RVAR_raw distributions of region I. The selection of correct number of particle induced events and hence the finding of proper slope of PVAR_raw vs event time graph could not be obtained for the above mentioned case.

In some cases, due to selection of wrong bubble peak of FVAR_raw distribution of a region, it becomes extremely difficult to fit the FVAR_raw distribution automatically. This is observed in the case of three sets of detectors and calibration runs, namely, detector 71 and run 0.2780.4, detector 141 and run 0.6021.4, detector 145 and run 0.6020.4 in Method II and for detector 93 and run 0.2780.4 in Method I. As a result, the correct number of recoil induced nucleation events for that particular region, could not be determined.

The values of PVAR_raw, FVAR_raw and RVAR_raw vary with transducers.

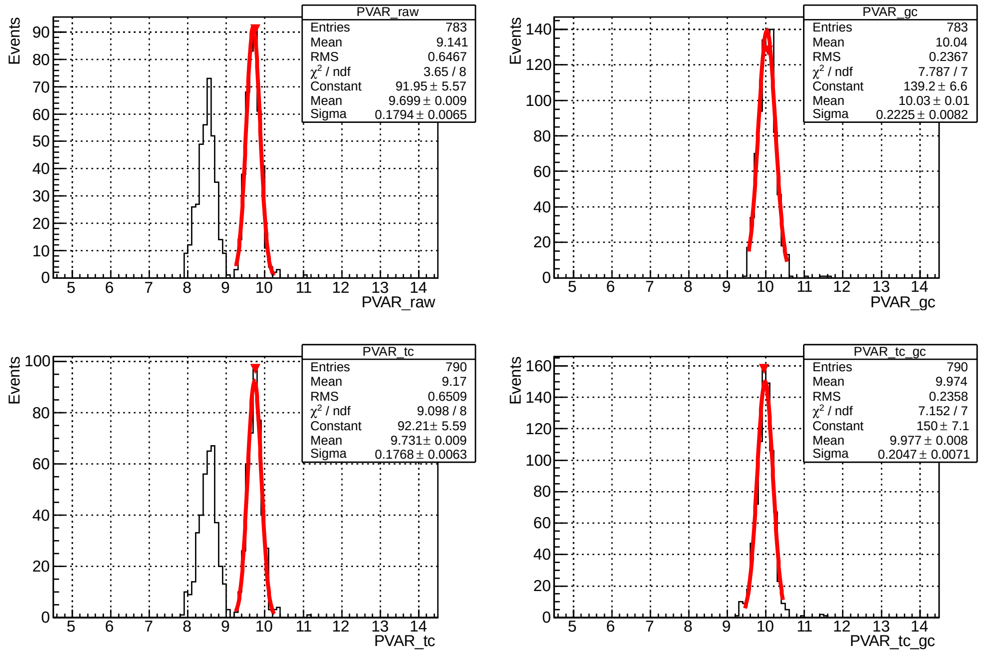

(a) Run 0.2779.4 and detector 71.

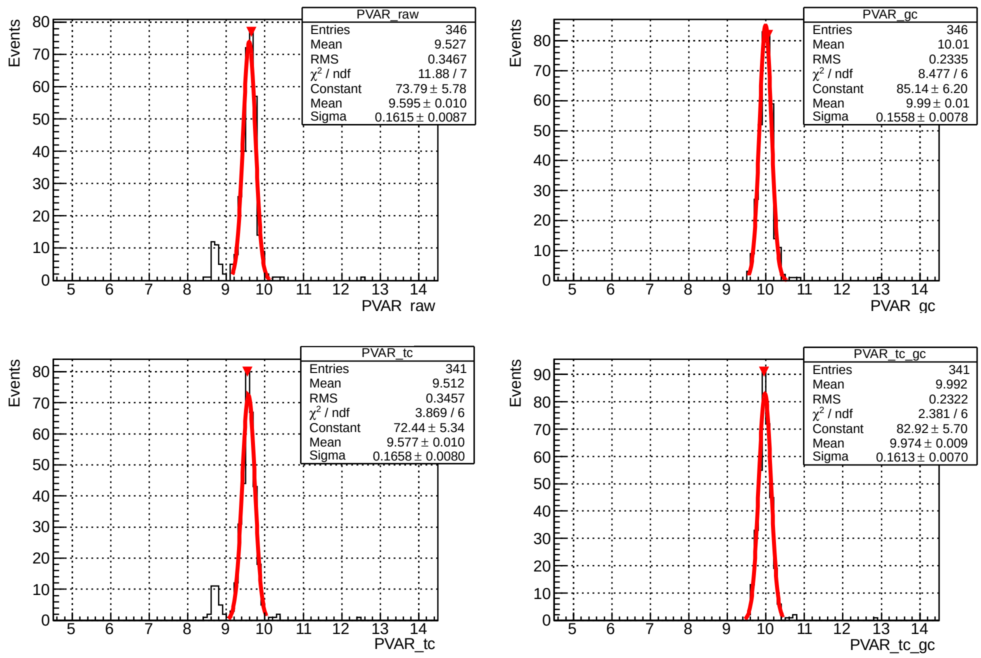

(b) Run 0.6020.4 and detector 141.

Figure 8.9: PVAR_raw, PVAR_gc, PVAR_tc and PVAR_tc_gc distributions of recoil induced nucleation events obtained by Method II. PVAR_raw and PVAR_tc distributions have two distinguished peaks unlike PVAR_gc and PVAR_tc_gc distributions in Method II.

This is reflected in the values of the variables calculated by taking the average over three transducers in Method II, but this effect is reduced in Method I because the variables are obtained by taking average over all of the nine active transducers. In Method II, sometimes the difference between the bubble peaks of the distribution of uncorrected variables are so large that the distribution of PVAR_raw and PVAR_tc of all of the particle induced events has two distinct peaks, which is not expected. Such distributions (shown in Figure 8.9) are observed in three detectors 71, 72 and 141. As a result, in Method II either it is better to handle these three variables distribution separately for three regions or to add **gain correction factor** to the variables before merging them.

For detector 93, the improvement factor (I_R) is obtained up to about 16.0 % in Method I, while in Method II the improvement factor (I_R) of resolution of PVAR_tc_gc distribution becomes about 34.97 %, 22.10 % and 28.34 % for runs 0.2779.4, 0.2780.4 and 0.2781.4, respectively. The improvement factor (I_R) of resolution in Method I for detector 71 and 72 and for the same three single speed calibration runs are about 3.48 %, 5.99 %, 10.94 % and -0.79 %, 1.57 %, -0.58 % respectively. So, Method I is not effective for detector 72 though it is observed that among three detectors 71, 72 and 93, the resolution of PVAR_raw is best for detector 72 in case of Method I.

For the detector 93, time correction by Method II in absence of gain correction is not so effective. The PVAR_raw and PVAR_tc distributions of all of the particle induced events obtained by Method II using single speed calibration runs have two distinct peaks for detectors 71 and 72 which vanish after gain correction. In the case of double speed run, if only time correction is considered, it is observed that for detectors 141 and 147, Method I is better than the Method II unlike in the case of detector 145. In Method II, gain correction is more effective than time correction (shown in Tables 8.3, 8.4 and 8.5) and most effective for detector 145.

The overall resolution of PVAR_raw distribution becomes better in the case of Method I than that of Method II and detector 147 has comparatively narrower PVAR_raw distribution among three of the detectors 141, 145 and 147.

8.4 Conclusions

We have analyzed three single speed calibration runs at temperature 40 °C for detectors 71, 72 and 93 of TPCS1 of the PICASSO experiment and ten double speed calibration runs at temperatures 40 °C, 35 °C and 30 °C for detectors 141, 145 and 147 of the same TPCS. It is observed that the resolution of PVAR distribution for double speed run is better than that of single speed run. We have developed the correction methods to improve the resolution of PVAR distribution by controlling the effect of decrement of PVAR with time, called **time correction**, along with the **gain correction**. The **gain correction** is required due to the variation of the peak of PVAR distribution with transducers. Two correction methods are developed —Method I, in which the variables are calculated as averaged over nine transducers and Method II, in which the variables are calculated as averaged over three transducers. Raw distribution of the PVAR variable without correction has better resolution in Method I than Method II. In Method II, both the time and gain correction are performed while in Method I, only time correction is considered. The gain correction is more effective than time correction in Method II and after correction by Method II, the resolution of PVAR distribution has been improved up to about 33 % (maximum) for the calibration runs.

Chapter 9

Summary and conclusions

In this thesis, we have presented the detailed study of the response of SDDs to various kinds of particles such as neutrons, alpha particles, gamma rays and heavy ions and also discussed application of SDDs in DM search experiment within the context of a specific experiment, namely, PICASSO.

After brief introduction and review on the basic principle of bubble nucleation in Chapter 1 and Charter 2, we have presented in Chapter 3 the results of our simulation studies to understand the physics behind the operating principle of SDD. The response of SDD to high energy heavy ions namely ^{12}C (180 MeV/u), ^{20}Ne (400 MeV/u) and ^{28}Si (350 MeV/u) has been studied with GEANT3.21 simulation toolkit to determine the values of the nucleation parameter, namely, k. Two sets of simulations have been performed. In one set the actual experimental set up has been simulated while in the other set instead of simulating the whole set up, the bubble nucleation probability of a single droplet as a function of the nucleation parameter (k) is determined. From both the simulations the normalized count rates at the threshold temperature of bubble nucleation are calculated and compared with the experimental data. The value of k for which the deviation between experiment and simulations is least is taken as best values of k for a particular ion.

Our results show that the nucleation parameter (k) depends on the mass number of the ions.

In Chapter 4 we have focused on the discrimination between the neutron and gamma - ray induced nucleation events in SDD. We have performed experiments using two different liquids, namely, R-114 and C_4F_{10}. For this purpose, we have used a ^{252}Cf (3.2 μCi) fission neutron source and a ^{137}Cs gamma-ray source (32.5 mCi). We have performed the experiments at the neutron sensitive temperatures of 55 °C for R-114 and 35 °C for C_4F_{10} and also at neutron and gamma-ray sensitive temperatures of 70 °C for R-114 and 55 °C for C_4F_{10} in presence of ^{252}Cf source. We have shown how the pulse height distribution can be used to effectively discriminate between the neutron and gamma-ray induced nucleation events. It was also observed that R-114 as active liquid of SDD gives better neutron-gamma discrimination than C_4F_{10}.

In the second part of the thesis, we have first reviewed in Chapter 5 the basic phenomenology and direct detection method of WIMP candidate of DM. In particular, we have discussed in details the methods used in the PICASSO experiment. In Chapter 6, Chapter 7 and Chapter 8, we presented the results of our studies towards understanding the alpha background of PICASSO detector and developing analysis method to increase the resolution of the discrimination between alpha and neutron induced nucleation events. In Chapter 6, we have performed a simulation to understand the two different threshold temperatures for two alpha sources, namely, ^{241}Am and ^{226}Ra. From the results of the simulation using GEANT3.21 simulation toolkit and calculation of LET using SRIM 2008 software, it is observed that the threshold temperature is lower in the case of ^{226}Ra spiked detector (for which the α contamination is present both in the droplet as well as in the polymer matrix) than in the case of ^{241}Am spiked detector (for which the source of the α contamination is in the polymer matrix only). This is shown to be due to bubble nucleation caused by the ^{210}Pb nuclei generated in the ^{226}Ra decay chain.

The effect of the droplet size on the discrimination between α- and neutron induced events, considering the low frequency components of the signal studied in Chapter 7 by performing experiments with superheated R-12 (CCl_2F_2, b. p. -29.8 °C) droplets dispersed in soft aquasonic gel in presence of two neutron sources, namely, ^{241}Am-Be (3 Ci) and ^{252}Cf (3.2 μCi), and an α-source, ^{241}Am (30 particles s^{-1}) at the temperature of 33.5±0.5 °C. Instead of obtaining larger amplitude of pulses for alpha-particle induced events, as previously observed by COUPP, PICASSO and SIMPLE experiments, both smaller and larger amplitude pulses are observed in our present experiments due to the droplet size distribution used in our experiment.

Finally in Chapter 8 we have presented the results of our new analysis technique to improve the alpha-neutron discrimination using PICASSO experiment data. This has resulted in an improvement of the resolution of the distribution of the variable PVAR (which is a measure of the acoustic energy released during the bubble nucleation process) for neutron calibration data of PICASSO experiment.

Bibliography

[1] R. C. Reid, *Rapid phase transitions from liquid to vapor.*, Adv. Chem. Eng. **12** (1983) 105.

[2] M. Blander and J. L. Katz, *Bubble nucleation in liquids.*, AIChE J. **21** (1975) 833.

[3] M. Das, B. K. Chatterjee, B. Roy and S. C. Roy, *How high can the temperature of a liquid be raised without boiling?*, Phys. Rev. E **62** (2000) 5843.

[4] D. A. Glaser, *Some effects of ionizing radiation on the formation of bubbles in liquids.*, Phys. Rev. **87** (1952) 665.

[5] R. E. Apfel, *Detector and dosimeter for neutrons and other radiation.*, US Patent **4143274** (1979).

[6] H. Ing and H. C. Birnboim, *A bubble-damage polymer detector for neutrons.*, Nucl. Tracks and Radiat. Meas. **8** (1984) 285.

[7] R. E. Apfel and S. C. Roy, *Investigations on the applicability of superheated drop detectors in neutron dosimetry.*, Nucl. Instrum. Methods. **219** (1984) 582.

[8] H. Ing, *The status of the bubble-damage polymer detector.*, Nucl. Tracks **12** (1986) 49.

[9] R. E. Apfel and Y. C. Lo, *Practical neutron dosimetry with superheated drops.*, Health Phys. **56** (1989) 79.

[10] F. d'Errico, *Radiation dosimetry and spectrometry with superheated emulsions.*, Nucl. Instrum. Methods B **184** (2001) 229.

[11] T. Cousins, K. Tremblay and H. Ing, *The application of the bubble detector to the measurement of intense neutron fluences and energy spectra.*, IEEE Trans. Nucl. Sci. **37** (1990) 1769.

[12] F. d'Errico *et al.*, *Active neutron spectrometry with superheated drop (bubble) detectors.*, Radiat. Protect. Dosim. **61** (1995) 159.

[13] M. Das, B. K. Chatterjee, B. Roy and S. C. Roy, *Superheated drop as a neutron spectrometer.*, Nucl. Instrum. Methods A **452** (2000) 273.

[14] R. E. Apfel and F. d'Errico, *A neutron spectrometer based on temperature variations in superheated drop compositions.*, Nucl. Instrum. Methods A **476** (2002) 298.

[15] M. Das and T. Sawamura, *Superheated emulsions in neutron spectrometry by varying ambient pressure.*, Nucl. Instrum. Methods A **536** (2005) 123.

[16] M. Barnabé-Heider *et al.*, *Response of superheated droplet detectors of the PICASSO dark matter search experiment.*, Nucl. Instrum. Methods A **555** (2005) 184.

[17] T. Morlat *et al.*, *A CF_3I-based SDD prototype for spin-independent dark matter searches.*, Astropart. Phys. **30** (2008) 159.

[18] E. Behnke *et al.*, *Improved limits on spin-dependent WIMP-proton interactions from a two liter CF_3I bubble chamber.*, Phys. Rev. Lett. **106** (2011) 021303.

[19] B. Roy, M. Das, S. C. Roy and B. K. Chatterjee, *Photon sensitivity of superheated drop at room temperature.*, Nucl. Instrum. Methods A **455** (2000) 782.

[20] B. Roy, M. Das, S. C. Roy and B. K. Chatterjee, *Threshold temperature for γ-ray detection in superheated drop detector.*, Radiat. Phys. Chem. **61** (2001) 509.

[21] S. L. Guo *et al.*, *Proton tracks in bubble detector.*, Nucl. Instrum. Methods B **198** (2002) 135.

[22] S. L. Guo *et al.*, *High energy heavy ion tracks in bubble detectors.*, Radiat. Meas. **31** (1999) 167.

[23] S. L. Guo *et al.*, *Characteristics of heavy ion tracks in bubble detectors.*, Radiat. Meas. **34** (2001) 269.

[24] S. L. Guo *et al.*, *Status of bubble detectors for high-energy heavy ions.*, Radiat. Meas. **36** (2003) 183.

[25] M. Das, N. Yasuda, A. Homma and T. Sawamura, *Threshold temperatures of heavy ion-induced nucleation in superheated emulsions.*, Nucl. Instrum. Methods A **543** (2005) 570.

[26] G. Hinshaw et al., *Nine-year Wilkinson Microwave Anisotropy Probe (WMAP) observations: cosmological parameter results.*, The Astrophys. J. Suppl. Ser., **208:19** (2013) 25.

[27] G. Jungman, M. Kamionkowski and K. Griest, *Supersymmetric dark matter.*, Phys. Rep. **267** (1996) 195.

[28] G. Bertone, D. Hooper and J. Silk, *Particle dark matter: evidence, candidates and constraints.* Phys. Rep. **405** (2005) 279.

[29] G. Bertone, ed., “Particle dark matter : observations, models and searches” (Cambrige Univ. Press, 2010).

[30] D. Bauer et al., *Dark matter in the coming decade: complementary paths to discovery and beyond.* arXiv:1305.1605.

[31] M. W. Goodman and E. Written, *Detectability of certain dark-matter candidate.*, Phys. Rev. D **31** (1985) 3059.

[32] S. Archambault *et al.*, *Constraints on low-mass WIMP interactions on* ^{19}F *from PICASSO.*, Phys. Lett. B **711** (2012) 153.

[33] F. Seitz, *On the theory of the bubble chamber.*, Phys. Fluids **1** (1958) 2.

[34] J. W. Gibbs, *On the equilibrium of heretogeneous subtances.*, Transl. Conn. Acad. **III** (1875) 108.

[35] R. E. Apfel, S. C. Roy and Y. C. Lo, *Prediction of the minimum neutron energy to nucleate vapor bubbles in superheated liquids.*, Phys. Rev. A **31** (1985) 3194.

[36] M. Das and T. Sawamura, *Estimation of nucleation parameter for neutron-induced nucleation in superheated emulsion.*, Nucl. Instrum. Methods A **531** (2004) 577.

[37] M. Das, B. Roy, B. K. Chatterjee and S. C. Roy, *Use of basic principle of nucleation in determining temperature-threshold neutron energy relationship in superheated emulsions.*, Radiat. Phys. Chem. **66** (2003) 323.

[38] A. G. Tenner, *Nucleation in bubble chambers.*, Nucl. Instrum. Methods **22** (1963) 1.

[39] Ch. Peyrou, *Bubble and Spark Chambers editted by R P Shutt, vol I, (Academic Press, 1967).*

[40] M. J. Harper, *A theoretical model of a superheated liquid droplet neutron detector.*, Ph. D. Dissertation, Univ. Maryland, (1991).

[41] A. Norman and P. Spiegler, *Radiation nucleation of bubbles in water.*, Nucl. Sci. Eng. **16** (1963) 213.

[42] L. Rayleigh, *On the instability of cylindrical fluid surfaces.*, Philos. Mag. **34 (207)** (1892) 177.

[43] M. M. El-Nagdy and M. J. Harris, *Experimental study of radiation induced boiling on superheated liquids.*, J. Brit. Nucl. Eng. Soc. **10** (1971) 131.

[44] L. W. Dietrich and T. J. Connolly, *A study of fission-fragment-induced nucleation of bubbles in superheated water.*, Nucl. Sci. Eng. **50** (1973) 273.

[45] C. R. Bell, N. P. Oberle, W. Rohsenow, N. Todreas and C. Tso, *Radiation-induced boiling in superheated water and organic liquids.*, Nucl. Sci. Eng. **53** (1974) 458.

[46] N. P. Oberle, *Radiation induced nucleation in water and organic liquids.*, MS Thesis, Massachusetts Institute of Technology, Department of Nuclear Engineering, (1972).

[47] C. Tso, *Some aspects of radiation induced nucleation in water.*, MS Thesis, Massachusetts Institute of Technology, Department of Nuclear Engineering, (1970).

[48] M. J. Harper and J. C. Rich, *Radiation-induced nucleation in superheated liquid droplet neutron detectors.*, Nucl. Instrum. Meth. A **336** (1993) 220.

[49] S. Tsuda, T. Sawamura, A. Homma and M. Narita, *Pressure dependence of neutron detection sensitivity in a superheated drop detector.*, Radiat. Protect. Dosim. **87** (2000) 87.

[50] F. Ziegler, M. D. Ziegler and J. P. Biersack, http://www.srim.org/

[51] M. Das, N. Yasuda and T. Sawamura, *Threshold ss of superheated emulsion detector to heavy ions.*, Radiat. Meas. **43** (2008) S62.

[52] W. Lim and C. K. Wang, *Computational studies of neutron response function for a neutron spectrometer which uses Freon-12, -22, and -115 superheated liquids.*, Nucl. Instrum. Meth. A **335** (1993) 243.

[53] GEANT *Detector description and simulation tool CERN Program Library long WRITE-up W5103 CERN Geneva Switzerland.*

[54] SRAND, http://gcc.gnu.org/onlinedocs/gfortran/SRAND.html

[55] S. C. Roy, *Superheated liquid and its place in radiation physics.*, Rad. Phys. Chem. **61** (2001) 271.

[56] S. C. Roy and G. A. Sandison, *Shielding for neutron scattered dose to the fetus in patients treated with 18 MV x-ray beams.*, Med. Phys. **27** (2000) 1800.

[57] F. Aubin *et al.*, *Discrimination of nuclear recoils from alpha particles with superheated liquids.*, New. J. Phys. **10** (2008) 103017.

[58] M. Felizerdo *et al.*, *First Results of the Phase II SIMPLE Dark Matter Search.*, Phy. Rev. Lett. **105** (2010) 211301.

[59] B. Roy, B. K. Chatterjee and S. C. Roy, *An accurate method of measuring lifetime of superheated drops using differential manometer.*, Radiat. Meas. **29** (1998) 173.

[60] M. Das, A. S. Arya, C. Marick, D. Kanjilal and S. Saha, *An active drop counting device using condenser microphone for superheated emulsion detector.*, Rev. Sci. Instrum. **79 (11)** (2008) 113301.

[61] S. Archambault *et al.*, *New insights into particle detection with superheated liquids.*, New. J. Phys. **13** (2011) 043006.

[62] S. Archambault *et al.*, *Dark matter spin-dependent limits for WIMP interactions on ^{19}F by PICASSO.*, Phys. Lett. B **682** (2009) 185.

[63] E. Hjalmar, H. Slätis and S. G. Thompson, *Energy spectrum of neutrons from spontaneous fission of Californium-252.*, Phys. Rev. **100** (1955) 1542.

[64] J. D. Lewin and P. F. Smith, *Review on mathematics, numerical factors, and corrections for dark matter experiments based on elastic nuclear recoil.*, Astropart. Phys. **6** (1996) 87.

[65] S. C. Kim *et al.*, *New limits on interactions between Weakly Interacting Massive Particles and nucleons obtained with CsI(Tl) crystal detectors.*, Phys. Rev. Lett. **108** (2012) 181301.

[66] R. Bernabei *et al.*, *Results from DAMA/LIBRA at Gran Sasso.*, Found. Phys. **40** (2010) 900.

[67] D. N. McKinsey, *The Mini-CLEAN experiment.*, Nucl. Phys. B (Proc. Suppl.) **173** (2007) 152.

[68] W. H. Lippincott *et al.*, *Scintillation yield and time dependence from electronic and nuclear recoils in liquid neon.*, Phy. Rev. C **86** (2012) 015807.

[69] H. Uchida *et al.*, *Search for inelastic WIMP nucleus scattering on ^{129}Xe in data from the XMASS-I experiment.*, Prog. Theor. Exp. Phys. **2012**, 00000 (13 pages), arXiv:1401.4737v3.

[70] E. Aprile *et al.*, *Dark matter results from 225 live days of XENON100 data.*, Phys. Rev. Lett. **109** (2012) 181301.

[71] D. S. Akerib *et al.*, *First results from the LUX dark matter experiment at the Sanford Underground Research Facility.*, Phys. Rev. Lett. **112** (2014) 091303.

[72] T. Alexander *et al.*, *DarkSide search for dark matter.*, JINST **8** (2013) C11021.

[73] D. S. Akerib *et al.*, *First Results from the Cryogenic Dark Matter Search in the Soudan Underground Laboratory.* Phy. Rev. Lett. **93** (2004) 211301.

[74] R. Agnese *et al.*, *Search for low-mass Weakly Interacting Massive Particles using voltage-assisted calorimetric ionization detection in the SuperCDMS experiment.*, Phy. Rev. Lett. **112** (2014) 041302.

[75] G. Angloher *et al.*, *Results from 730 kg days of the CRESST-II Dark Matter search.*, Eur. Phys. J. C **72:1971** (2012).

[76] E. Armengaud *et al.*, *Search for low-mass WIMPs with EDELWEISS-II heat-and-ionization detectors.*, Phy. Rev. D **86** (2012) 051701(R).

[77] H. Kraus *et al.*, *$ZnWO_4$ scintillators for cryogenic dark matter experiments.*, Nucl. Instrum. Methods A **600** (2009) 594.

[78] V. Zacek *et al.*, *Dark matter search with PICASSO*, Journal of Physics, ConferenceSeries **375** (2012) 012023.

[79] Guillaume Giroux, *Details of the analysis procedure in the discrimination of nuclear recoils from alpha particles with superheated liquids.* PICASSO Scientic / Technical Report : PSTR-08-009.

[80] Simon Archambault, *Discrimination d'événements par analyse des signaux enregistrés par le projet PICASSO*, M. Sc. thesis, Université de Montréal, (2010).

[81] Marie-Cécile Piro, *Nouvelles Limites sur la Détection Directe de la Matière Sombre avec l'Expérience PICASSO*, Ph.D. Thesis, Université de Montréal, (2012).

[82] Presentation by Marie-Cécile Piro, PICASSO collaboration internal document.

[83] http://detector-cooling.web.cern.ch/Detector-Cooling/data/C4F10.HTM.

[84] Matheson Company Inc., *Matheson Gas Data Book, 2001*

[85] ROOT, http://root.cern.ch/drupal/